

**THE GEOPHYSICAL VERY LOW FREQUENCY ELECTROMAGNETIC (VLF-EM)
METHOD: EFFECTS OF TOPOGRAPHY AND SURFACE WATER
INVESTIGATED WITH SIMULATIONS AND
FIELD MEASUREMENTS**

A Thesis Submitted to the College of
Graduate Studies and Research
In Partial Fulfillment of the Requirements
For the Degree of Master of Science
In the Department of Geological Sciences
University of Saskatchewan
Saskatoon

By

Zhen Zhang

PERMISSION TO USE

In presenting this thesis in partial fulfillment of the requirements for a Postgraduate degree from the University of Saskatchewan, I agree that the Libraries of this University may make it freely available for inspection. I further agree that permission for copying of this thesis in any manner, in whole or in part, for scholarly purposes may be granted by the professor or professors who supervised my thesis work or, in their absence, by the Head of the Department or the Dean of the College in which my thesis work was done. It is understood that any copying or publication or use of this thesis or parts thereof for financial gain shall not be allowed without my written permission. It is also understood that due recognition shall be given to me and to the University of Saskatchewan in any scholarly use which may be made of any material in my thesis.

Requests for permission to copy or to make other uses of materials in this thesis in whole or part should be addressed to:

Head of the Department of Geological Sciences

University of Saskatchewan

114 Science Place

Saskatoon, Saskatchewan S7N 5E2

Canada

ABSTRACT

The Very Low Frequency Electromagnetic (VLF-EM) method, which enables surveying without contact with the ground, is suitable for ground surveys in a wide area and has been used in mapping geology for decades. The technique makes use of signal radiation from military navigation radio transmitters operating in the frequency range of 15-30 kHz. When the electromagnetic wave impinges on the surface it is both reflected back into the air and refracted into the earth. By measuring the shifted reflected magnetic field relative to the primary field, subsurface structures can be constrained.

Although the VLF method has been widely used to map geology in the last several decades, few modeling studies have been published. Particularly the effect of topography on VLF measurements is poorly characterized. The objective of my research is to study and simulate the VLF topographic responses, and therefore to distinguish between such responses and actual subsurface resistivity anomalies in VLF-EM data.

A few basic models (homogenous half-space, horizontal contact and vertical contact) were first created using the finite-elements modeling software Comsol Multiphysics and verified with theoretical solutions. Subsequently, features such as hills and lakes were incorporated into these basic models and further analyzed. When modeling topographic effects, two relationships between max inphase / max slope and max Quad / max slope versus skin depth / hill width are found, which can be used to predict topographic effects when the slope of a hill and resistivity of the ground are known. Two different sets of field data acquired at Saskatoon's Diefenbaker Hill and at Cameco's Cree Extension are compared with the modeling results.

ACKNOWLEDGEMENTS

I would like to express the deepest appreciation to my supervisor, Professor Samuel Butler, for his constant help, invaluable advice and especially for his insightful comments on the draft of this report. Without his help, I could not have completed this paper.

I would like to thank Professor Jim Merriam, who is always kind and patient, and helped me enrich and broaden my knowledge.

I would also like to thank Tyler Mathieson, who provided me the Cameco Corporation survey data for the research and supported me during the survey in the Slush Lake region.

My thanks also go to C. Mary Liang, who greatly helped me to gather the VLF data in the Slush Lake region field survey.

Last but not least, I would like to express my thanks to my family for valuable encouragement and spiritual support during my studies.

TABLE OF CONTENTS

PERMISSION TO USE	i
ABSTRACT	ii
ACKNOWLEDGEMENTS	iii
LIST OF TABLES	vi
LIST OF FIGURES	vii
LIST OF EQUATIONS	xiv
1 INTRODUCTION	1
1.1 VLF ELECTROMAGNETIC METHOD.....	2
1.2 VLF ELECTROMAGNETIC MEASUREMENT HISTORY	2
1.3 VLF ELECTROMAGNETIC MODELING HISTORY	5
1.4 COMSOL MULTIPHYSICS SOFTWARE	8
1.5 THE FORMAT OF THE THESIS.....	8
2 THEORY	9
2.1 HOMOGENEOUS HALF-SPACE	10
2.2 BOUNDARY CONDITIONS	12
2.3 DIAGNOSTICS.....	14
2.4 COMSOL MODEL SETTING	17
3 BASIC 3D MODELS AND ANALYSIS	19
3.1 HOMOGENEOUS HALF-SPACE	20
3.1.1 ANGLE OF INCIDENCE	30
3.2 TWO LAYER EARTH MODELING	37

3.3 VERTICAL CONTACT MODELING.....	46
3.3.1 VERTICAL CONTACT: H-POLARIZATION	48
3.3.2 VERTICAL CONTACT: E-POLARIZATION.....	57
3.3.3 VERTICAL CONTACT: COMBINATION OF E-POLARIZATION & H-POLARIZATION	69
4 TOPOGRAPHY AND LAKE MODELS AND ANALYSIS.....	70
4.1 TOPOGRAPHY MODELING - HILL.....	71
4.2 LAKE MODELING.....	80
5 SASKATOON DIEFENBAKER HILL MODELS AND ANALYSIS.....	89
6 CAMECO CREE EXTENSION VLF SURVEY & SIMULATION.....	101
7 CONCLUSIONS	123
REFERENCES.....	126

LIST OF TABLES

Table 4.1 Data analysis of hill model at height 10m and width 50m.....	74
Table 4.2 Data analysis of hill model at height 20m and width 50m.....	74
Table 4.3 Data analysis of hill model at height 30m and width 50m.....	74
Table 4.4 Data analysis of hill model at height 40m and width 50m.....	75
Table 4.5 Data analysis of hill model at height 20m and width 40m.....	75
Table 4.6 Data analysis of hill model at height 20m and width 30m.....	75
Table 4.7 Data analysis of hill model at height 20m and width 20m.....	75

LIST OF FIGURES

Figure 1.1 Field components near the surface of the earth	4
Figure 3.1 3D simulation results of homogeneous half-space	21
Figure 3.2 Theoretical and simulated Y component of magnetic field (Hy) comparisons for a homogeneous half-space case.....	22
Figure 3.3 Theoretical and simulated tangential component of electric field (Ex) comparisons for homogeneous half-space case	23
Figure 3.4 Inphase plot of homogeneous half-space simulation.....	24
Figure 3.5 Quad plot of homogeneous half-space simulation	24
Figure 3.6 Phase angle between Ex and Hy for homogeneous half-space simulation when ground conductivity is 0.001 S/m	25
Figure 3.7 Calculated conductivity of homogeneous half-space simulation when ground conductivity is 0.001 S/m	25
Figure 3.8 Phase angle between Ex and Hy for homogeneous half-space simulation when ground conductivity is 0.002 S/m.....	26
Figure 3.9 Calculated conductivity of homogeneous half-space simulation when ground conductivity is 0.002 S/m	26
Figure 3.10 3D simulation results of an extremely high resistivity ground.....	28
Figure 3.11 Phase angle (degree) between Ex and Hy for homogeneous half-space simulation when ground conductivity is 0.00001 S/m.....	28
Figure 3.12 Horizontal magnetic fields (Hy) plot for homogenous half-space case with various angles of incidence.....	31

Figure 3.13 Tangential electric fields (E_x) plots for homogenous half-space case with various angles of incidence	32
Figure 3.14 Inphase plot of homogeneous half-space simulation with various angles of incidence	33
Figure 3.15 Quad plot of homogeneous half-space simulation with various angles of incidence	34
Figure 3.16 Phase angle plot of homogeneous half-space simulation with various angles of incidence.....	35
Figure 3.17 Calculated conductivity plot of homogeneous half-space simulation with various angles of incidence.....	36
Figure 3.18 Theoretical and simulated magnetic field Y component (H_y) comparisons for two layers earth case	38
Figure 3.19 Theoretical and simulated tangential component of electric field (E_x) comparisons for two layers earth case	38
Figure 3.20 Horizontal magnetic field plots with different conductivity values of the top layer at two layers earth model	40
Figure 3.21 Tangential electric field plots with different conductivity values of the top layer at two layers earth model	41
Figure 3.22 Phase angle plots with different conductivity values of the top layer at two layers earth model	42
Figure 3.23 Tangential electric field plots with different upper layer thickness of two layers earth model	43

Figure 3.24 Horizontal magnetic field plots with different upper layer thickness of two layers earth model	44
Figure 3.25 Simulated results of phase angles with different upper layer thickness of two layer earth model.....	45
Figure 3.26 3D view of H- polarization.....	48
Figure 3.27 3D simulation results of H-polarization	49
Figure 3.28 Horizontal magnetic field component plot of H-polarization	50
Figure 3.29 Tangential electric field component (Ex) plot of H-polarization	51
Figure 3.30 Inphase/Quad plots of H-polarization.....	52
Figure 3.31 Vertical magnetic field component plot of H-polarization.....	53
Figure 3.32 Tilt plot of H-polarization.....	53
Figure 3.33 Phase plot of H-polarization	54
Figure 3.34 Calculated conductivity plot of H-polarization	55
Figure 3.35 Phase plot with varying conductivity of medium 2 of H-polarization	56
Figure 3.36 3D view of E-polarization	57
Figure 3.37 3D simulation results of E-polarization.....	58
Figure 3.38 Horizontal magnetic field component plots of E-polarization	59
Figure 3.39 Horizontal magnetic field component plots of E-polarization	60
Figure 3.40 Vertical magnetic field component of E-polarization	61
Figure 3.41 Inphase & Quad plots of E-polarization.....	62
Figure 3.42 Tilt plot of E-polarization.....	63
Figure 3.43 Phase plot of E-polarization	64
Figure 3.44 Calculate conductivity plot of E-polarization.....	65

Figure 3.45 Inphase & Quad plots with varying conductivity of medium 2 of E-polarization.....	66
Figure 3.46 Tilt plots with varying conductivity of medium 2 of E-polarization.....	67
Figure 3.47 Phase plots with varying conductivity of medium 2 of E-polarization	68
Figure 3.48 Calculated Conductivity plots with varying conductivity of medium 2 of E-polarization.....	68
Figure 4.1 3D view of topography modeling results	72
Figure 4.2 Max inphase vs Ground Resistivity of hill model	76
Figure 4.3 Max QUAD vs Ground Resistivity of hill model.....	76
Figure 4.4 Max inphase/Max Slope vs Skin Depth/Hill Width.....	78
Figure 4.5 Max Quad/Max Slope vs Skin Depth/Hill Width.....	79
Figure 4.6 Max inphase vs Max Quad of hill modeling	79
Figure 4.7 3D Results of inphase Response of Lake Model.....	81
Figure 4.8 Horizontal Component of Magnetic Field in Lake Model	82
Figure 4.9 Top view of inphase Response in Lake Model.....	83
Figure 4.10 Inphase Response in Lake Model.....	84
Figure 4.11 Top view of Quad Response in Lake Model	85
Figure 4.12 Quad Response in Lake Model.....	85
Figure 4.13 Top view of inphase Response in Lake Model of Half Sphere Shape	86
Figure 4.14 Top view of Quad Response in Lake Model of Half Sphere Shape.....	87
Figure 5.1 Azimuth plots for different transmitter stations	90
Figure 5.2 VLF Measurement equipment	91
Figure 5.3 Field inphase reading vs. distance and 0.5 times slopes of Diefenbaker hill. .	93

Figure 5.4 Field Quad reading vs. distance and 0.25 times slopes of Diefenbaker hill. ...	94
Figure 5.5 25.2 kHz inphase reading vs. distance and 0.5 * slopes of Diefenbaker hill * cos (46 °).....	95
Figure 5.6 25.2 kHz Quad reading vs. distance and 0.25 * slopes of Diefenbaker hill * cos (46 °).....	95
Figure 5.7 Topographic profiles of Diefenbaker hill and best fitting Gaussian function .	96
Figure 5.8 3D simulation results of Diefenbaker hill at 24.8 kHz	97
Figure 5.9 Field measurement and simulation results comparison of inphase components of 24 kHz.....	97
Figure 5.10 Field measurement and simulation results comparison of quadrature components of 24 kHz	98
Figure 5.11 Field measurement and simulation results comparison of inphase components of 24.8 kHz	99
Figure 5.12 Field measurement and simulation results comparison of quadrature components of 24.8 kHz	99
Figure 5.13 Field measurement and simulation results comparison of inphase components of 25.2 kHz	100
Figure 5.14 Field measurement and simulation results comparison of quadrature components of 25.2 kHz	100
Figure 6.1 Topography of Cameco Cree Extension regions	103
Figure 6.2 Inphase of 24 kHz over UTM position system of 2006 VLF data	104
Figure 6.3 Quad of 24 kHz over UTM position system of 2006 VLF data	104
Figure 6.4 Inphase of 24.8 k z over UTM position system of 2006 VLF data	105

Figure 6.5 Quad of 24.8 kHz over UTM position system of 2006 VLF data	106
Figure 6.6 2006 Cameco NAA fixed Quad data	107
Figure 6.7 2006 Cameco NLK fixed Quad data	107
Figure 6.8 Positions of four different measurement lines of 2012 VLF data	108
Figure 6.9 24 kHz inphase plot of 2012 VLF data.....	109
Figure 6.10 24 kHz Quad plot of 2012 VLF data	109
Figure 6.11 24.8 kHz inphase plot of 2012 VLF data	110
Figure 6.12 24.8 kHz Quad plot of 2012 VLF data	110
Figure 6.13 24.8 kHz inphase and Quad plot of an individual measurement line of 2012 VLF data	111
Figure 6.14 25.2 kHz inphase plot of 2012 VLF data	112
Figure 6.15 25.2 kHz Quad plot of 2012 VLF data	112
Figure 6.16 Cameco topographic radar data in Slush Lake region	114
Figure 6.17 Slush lake inphase simulation plot of 24 kHz with 5000 ohm*m of ground resistivity.....	115
Figure 6.18 Slush lake Quad simulation plot of 24 kHz with 5000 ohm*m of ground resistivity.....	115
Figure 6.19 Slush lake inphase simulation plot of 24.8 kHz with 5000 ohm*m of ground resistivity.....	116
Figure 6.20 Slush lake Quad simulation plot of 24.8 kHz with 5000 ohm*m of ground resistivity.....	116
Figure 6.21 Slush lake inphase simulation plot of 24 kHz with 10000 ohm*m of ground resistivity.....	117

Figure 6.22 Slush lake Quad simulation plot of 24 kHz with 10000 ohm*m of ground resistivity.....	117
Figure 6.23 Slush lake inphase simulation plot of 24.8 kHz with 10000 ohm*m of ground resistivity	118
Figure 6.24 Slush lake Quad simulation plot of 24.8 kHz with 10000 ohm*m of ground resistivity.....	118

LIST OF EQUATIONS

Equation 2.1.....	10
Equation 2.2.....	10
Equation 2.3.....	10
Equation 2.4.....	10
Equation 2.5.....	11
Equation 2.6.....	11
Equation 2.7.....	11
Equation 2.8.....	11
Equation 2.9.....	11
Equation 2.10.....	11
Equation 2.11.....	11
Equation 2.12.....	12
Equation 2.13.....	12
Equation 2.14.....	12
Equation 2.15.....	12
Equation 2.16.....	12
Equation 2.17.....	13
Equation 2.18.....	13
Equation 2.19.....	13
Equation 2.20.....	13
Equation 2.21.....	14
Equation 2.22.....	14

Equation 2.23	14
Equation 2.24	14
Equation 2.25	14
Equation 2.26	15
Equation 2.27	15
Equation 2.28	15
Equation 2.29	15
Equation 2.30	16
Equation 2.31	16
Equation 2.32	16
Equation 2.33	17
Equation 2.34	17
Equation 2.35	17
Equation 2.36	17
Equation 3.1	29
Equation 3.2	47
Equation 3.3	47
Equation 3.4	47
Equation 3.5	47
Equation 3.6	51
Equation 4.1	71
Equation 4.2	73
Equation 4.3	73

CHAPTER 1
INTRODUCTION

1.1 VLF ELECTROMAGNETIC METHOD

The Very Low Frequency Electromagnetic (VLF-EM) method, which enables surveying for electrical conductors without contact with the ground, is suitable for ground surveying in a wide area and has been widely used to aid mapping geology for the past forty years (McNeill & Labson, 1991). The technique makes use of signal radiation from military navigation radio transmitters. There are around 42 global ground military communication transmitters operating at VLF frequencies of 15-30 kHz. The signals from these stations are effectively used for a variety of applications such as ground water detection, soil engineering, nuclear waste detection, and mineral exploration (Sundararajan, Babu, Prasad, & Srinivas, 2006).

1.2 VLF ELECTROMAGNETIC MEASUREMENT HISTORY

Measurements of the conductivity of the earth using the “wave-tilt” method were first done in the 1930’s. However, those early measurements were carried out with a relatively high frequency and, as a result, had a shallow depth of investigation. In 1963, Paal (1965) found that radio waves at frequencies of 3-30 kHz could be used to detect shallow ore bodies. By surveying over known ore bodies in Sweden, Paal found that the horizontal VLF magnetic field reached a maximum value over underground conductors and the modulus of the vertical magnetic field dropped to a minimum at the same location. Since 1964, commercially available ground VLF instruments have been manufactured. However, early instruments used atmospheric magnetic fields as sources. Collett and Becker (1967) introduced a new approach which used VLF transmitters as the signal

source. The new approach used a coherent source and made it possible to measure the phase angle between the horizontal electric and magnetic fields. In 1973, Telsley (1973) suggested using a portable VLF transmitter which could enhance the receiving signal (McNeill & Labson, 1991).

The detection of subsurface formations or anomalies is made feasible by using a portable VLF receiver recording the inphase and quadrature components of the vertical secondary magnetic field relative to the horizontal and primary field. The VLF transmitter can be considered as a vertical electric dipole at the ground surface generating electromagnetic waves which consist of a vertical electric field component and a horizontal magnetic field component. In most cases, when measurements are made at a large distance from the transmitter, the electromagnetic wave can be viewed as a plane wave propagation horizontally. When the primary electromagnetic field impinges on the surface it is both reflected back into the air and refracted into the earth (see figure 1.1). By measuring the shifted reflected magnetic field relative to the primary field, the subsurface structures can be constrained (McNeill & Labson, 1991).

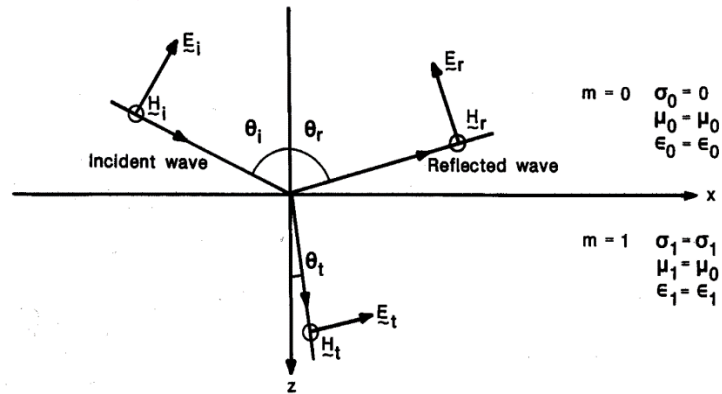


Figure 1.1 Field components near the surface of the earth (McNeill & Labson, 1991)

In the figure, E and H represent the electric field and magnetic field, θ_i is the angle of incidence, σ is the conductivity, μ is the permeability, and ϵ is permittivity. Index m represents different materials.

In VLF-EM prospecting, one of the factors influencing measured data is the effect of topography in the survey areas. Uneven terrain contributes significant anomalies which cause the observed VLF data to depart from the pattern which would be expected on flat ground. It is therefore important to distinguish between such topographic responses and actual subsurface anomalies (Abdul-Malik, Myers, & McFarlane, 1985).

Another factor influencing VLF measured data is the effect of water in the survey areas. Unlike moisture in the ground, surface waters such as lakes and rivers usually have a clear conductivity contrast with surrounding ground materials, therefore VLF anomalies are created when surveying. Like the topography effect, the VLF responses of surface waters need to be distinguished from those due to ground conductors.

1.3 VLF ELECTROMAGNETIC ANALYSIS HISTORY

Although the VLF method has been widely used to map geology over the last several decades, few modeling studies have been published. Most geophysicists have relied on field experience to interpret VLF anomalies (McNeill & Labson, 1991).

There are a few filters that have been used to process the raw measurement data. Fraser and Hjelt filters and subsequent contouring of measurement data are commonly used to enhance qualitative analysis methods. Fraser (1969) suggested passing the inphase data through a band pass filter to reduce noise before generating a VLF contour map. The technique removes the DC noise and Nyquist frequency related noise, reduces long wavelength signals, and phase shifts all frequency by 90 degree (Fraser, 1969; Sundararajan et al., 2006). Another filter proposed by Karous and Hjelt (1977, 1983) allows geophysicists to filter the inphase data and generate an apparent current density pseudosection and therefore image the geological underground structure (M. Karous & Hjelt, 1977, 1983; Sundararajan et al., 2006). Hilbert introduced another filter which shares some similarity with the Fraser filter which shifts the inphase component phase by 90 degrees and turns crossovers into peaks and troughs. The peaks can be interpreted as conductors (Sundararajan, Babu, & Chaturvedi, 2011). In the absence of numerical modeling, these filters provide first-hand information about size, depth and relative position of the conductivity anomalies. However, these filters lose 20% to 30% of the original data which may contain valuable information (Sundararajan et al., 2011).

Several quantitative inversion schemes can be used to interpret VLF or VLF-R (Resistivity) data. Beamish (1994) used a minimum structure inversion method which is referred to as OCCAM, created by deGroot-Hedlin and Constable (1990), to interpret VLF-R data. In further studies, Beamish (2000) improved the quantitative inversion method of two-dimensional VLF data interpretation using the non-linear, conjugate gradient (NLCG) algorithm. He demonstrated that at a high measurement density, single frequency VLF data can be used to interpret subsurface resistivity distributions (Beamish, 2000). However, the approach is only developed for a flat surface. Baranwal (2011) used the damped least -squares inversion method to interpret the VLF and VLF-R data including topographic effects (Baranwal, Franke, Börner, & Spitzer, 2011).

Based on the solutions of Maxwell's equations, numerical modeling methods have been carried out over several decades, but only in the last twenty years have complex two-dimensional (2D) modeling solutions been developed (Baranwal et al., 2011; Zhdanov, Varentsov, Weaver, Golubev, & Krylov, 1997). Tarkhov (1962) carried out some simple calculations of very low frequency EM fields and Gordeyev (1970) used simulations to attempt solving the EM field relationship. Kaikkonen (1979) presented finite element model results of vertical and 45 degrees dipping conductors with different conductivities of overburden (Kaikkonen, 1979). However the other parameters such as host rock resistivity and depth of the underground target were not discussed. Sinha (1990) extended the studies of the sheet-like, 2-D conductors with various inclined angles, various depth, different geometries, and different resistivity values of the host rock (Sinha, 1990a, 1990b).

There are a few studies related to the topographic effect in VLF-EM data interpretation. Whittles (1969) suggested two simple ways for dealing with topographic effects. The first method is a simple graphical treatment of smoothing of the tilt angle data by considering that the sloping is caused by topographic effects. The cross-overs of measurement data with the smoothed background line are used to determine the underground target location. The second method was to calculate the first derivative of the real component values, leaving the effect of a buried conductor expressed as a local low flanked by two small highs. However this method is only effective when earth has a uniform slope (Baker & Myers, 1980). Using the simple EM field calculations of Tarkhove (1962), Karous (1979) solved the undamped and damped approximate analytical calculations to determine the terrain relief effect in the EM methods at distant sources. The case of a two-dimensional E-polarization electromagnetic plane wave was modeled to verify the solutions compared with measured data (M. R. Karous, 1979). Baker and Myers (1980) established VLF-EM tank model experiments and estimated the topographic effects of various angles of dip and depths over a sheet like conductive target (Baker & Myers, 1980). However, the Baker and Myers method is based on ideal situations and Abdul-Malik (1985) developed the method by accounting for directions of hill strikes relative to survey lines and electromagnetic field directions (Abdul-Malik et al., 1985). During the inversion model studies to interpret VLF and VLF-R data, Baranwal (2011) found that the topography effect may become significant. In his models, the total response is decomposed into individual components from the topography and from subsurface conductivity structures. However, the VLF data cannot be distinguished from background noise very well (Baranwal et al., 2011).

1.4 COMSOL MULTIPHYSICS SOFTWARE

Comsol Multiphysics is finite-element modeling software and is a convenient tool for modeling. The software is simply a translation of real-world physical laws into their virtual form and allows users an accurate depiction of what happens in the real world. Comsol Multiphysics allows users to combine different models or add particular parameters into models ("Introduction to Comsol Multiphysics," 2014). As an advantage, for many standard problems, there exist premade application modes and it allows users to edit variables easily using a GUI.

1.5 THE FORMAT OF THE THESIS

In chapter 2, the theory of VLF wave propagation over a homogeneous half-space and layered ground are studied. In chapters 3 and 4, numerical models of a homogenous half-space, layered earth, vertical contact, topography, and lake are analyzed and results are compared with theories. In chapter 5, a new model is created by combining all of the basic models and is compared with real survey data from Diefenbaker Hill, Saskatoon. In chapter 6, a detailed finite-element model is created for the Slush Lake property of Cameco Corporation. The simulation results are compared with 2006 and 2012 VLF survey data.

CHAPTER 2
THEORY

2.1 HOMOGENEOUS HALF-SPACE

In the book “*Electromagnetic Methods in Applied Geophysics*”, McNeill and Labson explained the theory of VLF wave propagation over a homogeneous half-space earth and it is summarized in the following paragraphs.

The air has zero conductivity and permittivity ϵ_0 . The ground has conductivity σ_1 and permittivity $\epsilon_1 = \epsilon_r \epsilon_0$, where ϵ_r is the relative dielectric constant. The permeability, μ , is assumed constant in both the air and the ground.

Maxwell’s equations give the behavior of the electric and magnetic fields in the air and ground.

$$\nabla \times \mathbf{E} = -\frac{\partial \mathbf{B}}{\partial t}. \quad \text{Faraday's Law} \quad \text{Equation 2.1}$$

$$\nabla \times \mathbf{H} = \mathbf{J} + \frac{\partial \mathbf{D}}{\partial t}. \quad \text{Ampere's Law} \quad \text{Equation 2.2}$$

$$\nabla \cdot \mathbf{B} = 0. \quad \text{Equation 2.3}$$

$$\mathbf{B} = \mu \mathbf{H}, \mathbf{D} = \epsilon \mathbf{E}, \mathbf{J} = \sigma \mathbf{E}. \quad \text{Equation 2.4}$$

Where \mathbf{E} is the electric field strength, \mathbf{B} is magnetic induction, \mathbf{D} is electric displacement,

\mathbf{H} is the magnetic field, and \mathbf{J} is the current density.

The time variation is harmonic with frequency ω so we can write the time variation of all quantities as $e^{i\omega t}$, and so $\frac{\partial \mathbf{H}}{\partial t} = i\omega \mathbf{H}$. When substituting these formulas into Faraday's

Law and Ampere's Law, the equations become

$$\nabla \times \mathbf{E} = -i\omega \mu \mathbf{H}, \quad \text{Equation 2.5}$$

and $\nabla \times \mathbf{H} = (\sigma + i\omega \epsilon) \mathbf{E}$. Equation 2.6

Taking the curl of equation 2.6,

$$\nabla(\nabla \cdot \mathbf{H}) - \nabla^2 \mathbf{H} = (\sigma + i\omega \epsilon) \nabla \times \mathbf{E}, \quad \text{Equation 2.7}$$

but $\nabla \cdot \mathbf{H} = 0$, Equation 2.8

therefore, the total magnetic field equation can be expressed as

$$\nabla^2 \mathbf{H} = (\sigma + i\omega \epsilon) i\omega \mu \mathbf{H}. \quad \text{Equation 2.9}$$

The general solutions for the horizontal component of the magnetic field and tangential component of the electric fields are

$$H_{my} = (a_m e^{-u_m z} + b_m e^{u_m z}) e^{-i\lambda x}, \quad \text{Equation 2.10}$$

and $E_{mx} = \frac{-1}{\sigma_m + i\omega \epsilon_m} \frac{\partial H_{my}}{\partial z}$. Equation 2.11

Where $m = 0$ in air, $m = 1$ in the half-space, a_0 is the amplitude of the incoming magnetic field in the air, and b_0 is the amplitude of the reflected magnetic field in the air. For the rest of this section, the wave is propagating along the x axis.

In equation 2.10, u and λ are defined as

$$u_m^2 = \lambda^2 - k_m^2, \quad \text{Equation 2.12}$$

$$\text{and } \lambda = k_0 \sin \theta_i, \quad \text{Equation 2.13}$$

$$\text{where } k_m = (\omega^2 \mu_m \epsilon_m - i\omega \mu_m \sigma_m)^{1/2}, \quad \text{Equation 2.14}$$

and θ_i is the angle of incidence (Referring to figure 1.1).

2.2 BOUNDARY CONDITIONS

The horizontal component of the magnetic field and the tangential component of the electric field are continuous across the air-ground interface. At the air-Earth boundary ($z = 0$), $H_{oy} = H_{1y}$ and $E_{ox} = E_{1x}$.

For an infinite half space with the specified conductivity (Referring to the equations 2.10), the magnetic field can be expressed as

$$H_{oy} = (a_0 e^{-u_0 z} + b_0 e^{u_0 z}) e^{-i\lambda x}, \text{ in air,} \quad \text{Equation 2.15}$$

$$\text{and } H_{1y} = a_1 e^{-u_1 z} e^{-i\lambda x}, \text{ in ground.} \quad \text{Equation 2.16}$$

Only a downward wave exists in this model since the homogenous half-space is assumed to be of infinite depth extent. As a result, the ground equation only contains a refracted component. In the numerical model, the amplitude of the primary magnetic field in air (a_0) is assumed to be 1.

The electric fields in the air and ground can be calculated from

$$E_{ox} = \frac{-1}{\sigma_0 + i\omega\epsilon_0} \frac{\partial H_{0y}}{\partial z}, \quad \text{Equation 2.17}$$

and
$$E_{1x} = \frac{-1}{\sigma_1 + i\omega\epsilon_1} \frac{\partial H_{1y}}{\partial z}. \quad \text{Equation 2.18}$$

Requiring that $H_{0y}=H_{1y}$ and $E_{ox}=E_{1x}$ at the ground surface ($z=0$), coefficients a_1 and b_0 can be derived.

For multi-layer earth cases, the boundary conditions are applied at each interface where the conductivity changes discontinuously. For a two layer Earth, the magnetic fields in each layer are:

$$H_{0y} = (a_0 e^{-u_0 z} + b_0 e^{u_0 z}) e^{-i\lambda x}, \quad \text{in air,} \quad \text{Equation 2.15}$$

$$H_{1y} = a_1 e^{-ik_1 z} + b_1 e^{ik_1 z} \quad \& \quad k_1 = (\omega^2 \mu_0 \epsilon_1 - i\omega \mu_0 \sigma_1)^{1/2}, \quad \text{in the top layer,} \quad \text{Equation 2.19}$$

and
$$H_{2y} = a_2 e^{-ik_2 z} \quad \& \quad k_2 = (\omega^2 \mu_0 \epsilon_2 - i\omega \mu_0 \sigma_2)^{1/2}, \quad \text{in the lower layer.} \quad \text{Equation 2.20}$$

z is negative upward, positive downward and equal to zero at the interface between the air and the ground.

The horizontal magnetic and tangential electric fields are required to be continuous at all of the interfaces. Therefore,

$$H_{0y} = H_{1y} \text{ at } z = 0, \quad \text{Equation 2.21}$$

$$H_{1y} = H_{2y} \text{ at } z = h \text{ (the thickness of top layer),} \quad \text{Equation 2.22}$$

$$E_{0x} = E_{1x} \text{ at } z = 0, \quad \text{Equation 2.23}$$

and $E_{1x} = E_{2x} \text{ at } z = h \text{ (the thickness of top layer).} \quad \text{Equation 2.24}$

The four unknown coefficients b_0 , a_1 , b_1 and a_2 can be determined from the resulting four equations.

2.3 DIAGNOSTICS

Inphase (abbreviation IP) and Quadrature (abbreviation Quad) are the two most important field measurements of the VLF method and can be expressed as the normalized real and quadrature components of the vertical magnetic field.

$$inphase = \frac{real(H_z)}{\sqrt{(H_x^2 + H_y^2)}} . \quad \text{Equation 2.25}$$

$$Quad = \frac{imag(H_z)}{\sqrt{(H_x^2 + H_y^2)}} . \quad \text{Equation 2.26}$$

Another two quantities which are surface impedance and tilt angle yield useful information about the properties of the ground and can easily be calculated.

Tilt angle is defined as the angle of the real part of the vertical magnetic field to the horizontal magnetic field (Reynolds, 1997). Referring to the inphase definition, tilt can also be defined as arctan(inphase). Since inphase tends to be small, the two diagnostics are usually very similar in shape.

$$\text{Tilt angle: } \Delta = \arctan\left(\frac{real(H_z)}{\sqrt{H_x^2 + H_y^2}}\right) . \quad \text{Equation 2.27}$$

The surface impedance is defined as the ratio of the horizontal electric to perpendicular horizontal magnetic fields at the surface. For an infinite half-space, these can be expressed as

$$\frac{E_{0x}}{H_{0y}} = \frac{u_1}{\sigma_1 + i\omega\epsilon_1} = \eta_1 \left(1 - \frac{k_0^2}{k_1^2} \sin^2 \theta_i\right)^{1/2} , \quad \text{Equation 2.28}$$

$$\text{and } \eta_1 = \frac{ik_1}{\sigma_1 + i\omega\epsilon_1} = \left(\frac{i\mu_1\omega}{\sigma_1 + i\omega\epsilon_1}\right)^{1/2} . \quad \text{Equation 2.29}$$

In typical earth materials, $k_1 \gg k_0$, and conduction current flow greatly exceeds displacement current since $\sigma \gg \omega\epsilon$. Applying these assumptions to surface impedance, the equation can be approximated as

$$\frac{E_{0x}}{H_{0y}} \approx \eta_1 = \left(\frac{i\mu_1\omega}{\sigma_1 + i\omega\epsilon_1} \right)^{1/2} \approx \left(\frac{i\mu_1\omega}{\sigma_1} \right)^{1/2}. \quad \text{Equation 2.30}$$

In the upper equation μ_1 , ω and σ_1 are all real numbers and the $i^{1/2}$ term indicates that the phase angle between the tangential electric field and the horizontal magnetic field will be 45 degrees. This phase angle is a commonly plotted quantity. For a homogeneous half-space, the phase shift between the tangential electric and the magnetic fields at the surface is 45 degrees when $\sigma \gg \omega\epsilon$.

The phase angle can also be calculated as

$$\phi = a \tan\left(\frac{\text{imag}(E_x)}{\text{real}(E_x)} \right) - a \tan\left(\frac{\text{imag}(H_y)}{\text{real}(H_y)} \right). \quad \text{Equation 2.31}$$

The conductivity of the ground can be calculated based on equation 2.30. This allows us also to derive the apparent conductivity for conductive ground,

$$\sigma_1 = \frac{\omega\mu_1}{\left[\left(\frac{E_{0x}}{H_{0y}} \right) / \frac{(1+i)}{2^{1/2}} \right]^2}, \quad \text{Equation 2.32}$$

and apparent resistivity $\rho_1 = \frac{1}{\sigma_1}$. Equation 2.33

Skin depth is a measure of how far electromagnetic wave propagation takes place in a conductor, and is a function of frequency.

The skin depth is defined as (Reynolds, 1997)

$$\delta = \left(\frac{2}{\mu\sigma\omega} \right)^{1/2} \approx 500(\rho / f)^{1/2} .$$
Equation 2.34

2.4 COMSOL MODEL SETTING

Comsol Multiphysics versions 4.2 and 4.3 were chosen for modeling. A premade application mode of electric and induction currents from Quasi-Statics electromagnetics in the AC/DC module was used. Boundary condition equations and different parameters are added and edited based on theory.

The premade equations in Comsol governing magnetic fields with no galvanic sources are

$$(i\omega\sigma - \omega^2\varepsilon_0\varepsilon_r)\mathbf{A} + \nabla \times (\mu_0^{-1}\mu_r^{-1}\mathbf{B}) - \sigma\nabla \times \mathbf{B} = \mathbf{J}_e ,$$
Equation 2.35

and $\mathbf{B} = \nabla \times \mathbf{A}$. Equation 2.36

The equations are equivalent to equations 2.1, 2.2, 2.3 & 2.4. \mathbf{A} is the magnetic vector potential, J_e is the external current density which has 0 value in all simulations, and \mathbf{v} is the velocity of the model domain created which also has 0 value in the simulations.

In each numerical model, the boundary conditions are set on the outside of the models, and the tangential components of the magnetic field are specified using equation 2.10.

CHAPTER 3

BASIC 3D MODELS AND ANALYSIS

3.1 HOMOGENEOUS HALF-SPACE

As mentioned earlier, when the electromagnetic wave is generated from a transmitter situated on flat ground with constant conductivity, the near surface VLF waves contain an electric field that is tilted from vertical slightly in the direction of wave propagation and a horizontal magnetic field that is perpendicular to the direction of wave propagation. Also, there are both reflected and refracted waves when the electromagnetic wave impinges on the surface (figure 1.1). The air is where most magnetic measurements are made and the ground is where most electric field measurements are made.

A basic model consisting of a homogeneous half-space is first modeled using the finite-element software Comsol and the behavior of fields inside and above ground is considered in order to test the numerical model. 108895 tetrahedral elements are used in this model, and the mesh of the interface between the air and the ground is refined compared with the rest of the model.

In the homogeneous half-space model, earth is simply divided into two layers which are air and ground with a flat contact between them. The model domain consists of a cube of size $1000\text{m} \times 1000\text{m} \times 1000\text{m}$. The electromagnetic wave propagates along the X axis as shown in figure 3.1 and a frequency of 20 kHz is used. 0 S/m and 0.001 S/m are the values used for the air and ground electrical conductivity. $8.85\text{E-}12$ F/m is used for both permittivity of air and ground. The angle of incidence is $\pi/2 - \pi/40$.

The magnetic field is specified using equations 2.15 and 2.16 on the outer boundaries of the numerical model. When $a_0 = 1$, the coefficients b_0 and a_1 can be calculated to have values of $0.45957-0.3369i$ and $1.45957-0.3369i$.

The following figure shows the 3-D results of the VLF homogeneous half-space model. In the figure, the arrows indicate the current density which is parallel to the X axis for this configuration and decays with depth. The streamlines describe the electric field. The electric field is almost vertical in the air, while it becomes parallel to the X axis direction in the ground. The slices represent the Y component of the magnetic field which range from 1.4979 A/m to -0.172 A/m. The magnetic field is constant in the air and decays with depth in the ground. Since the fields on the outer boundaries are specified to be the analytical solution and they are constant in the X and Y directions in the interior of the model, we can see that the numerical solution is matching the analytical solution for an infinite half-space.

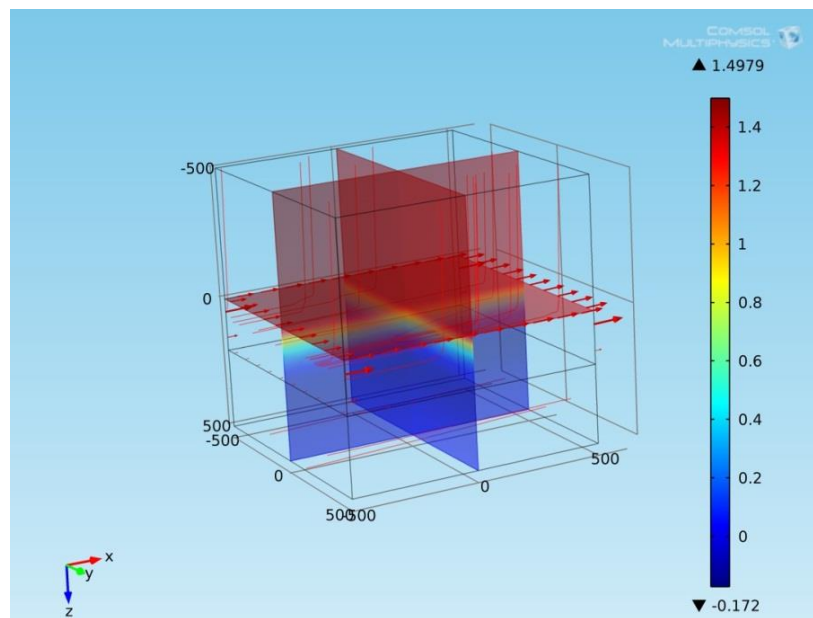


Figure 3.1 3D simulation results of homogeneous half-space

In figures 3.2 and 3.3 the simulation results and theoretical solutions of the primary magnetic field (H_y) and the tangential component of electric field (E_x) are plotted vertically at the horizontal center of the model. Real and quadrature components are indicated in the figures. As shown, E_x and H_y both are constant when in air ($Z < 0$) and decay with depth in ground ($Z > 0$). The real and quadrature components of the simulation results match ones from theoretical solutions which gives us confidence in the numerical model.

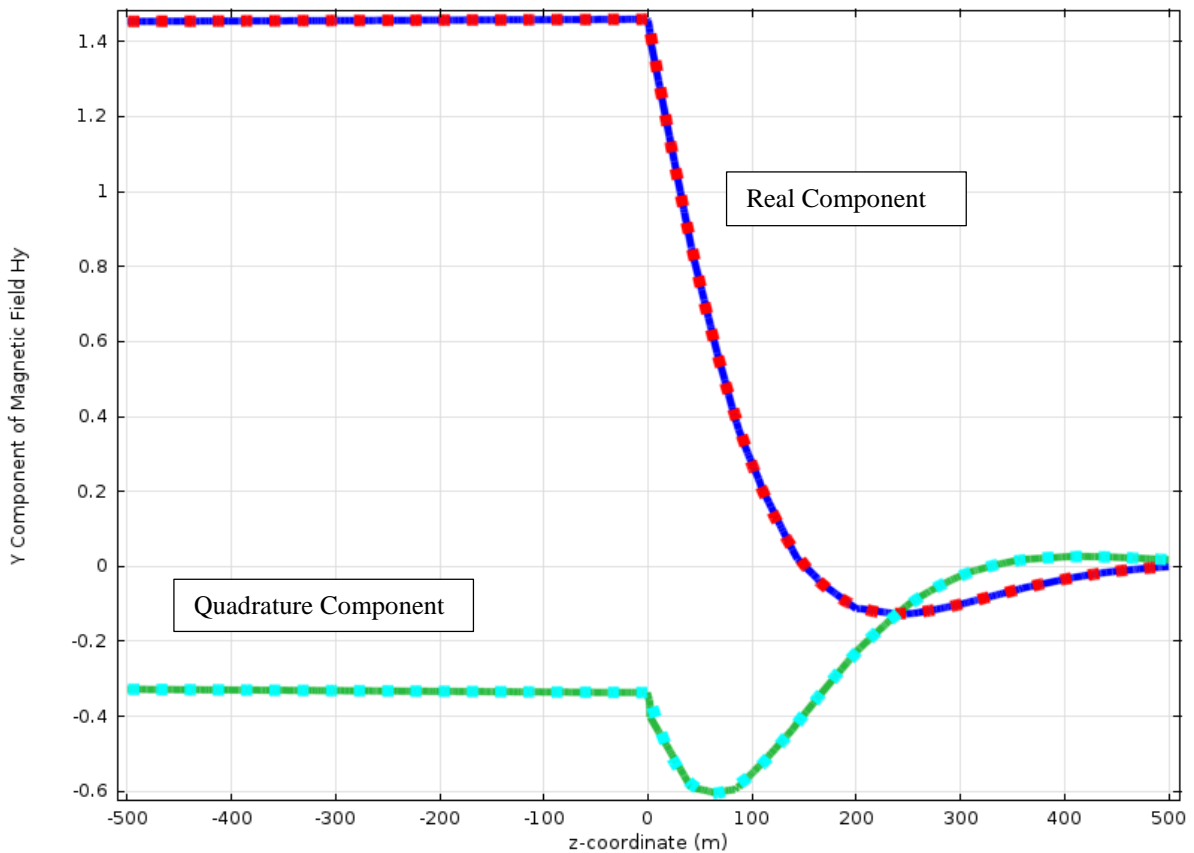


Figure 3.2 Theoretical and simulated Y component of magnetic field (H_y) comparisons for a homogeneous half-space at $X=0$ & $Y=0$ along the Z axis. Red (Dotted) and blue lines indicate the real component for theory and simulations while cyan (Dotted) and green lines represent the quadrature part for theory and simulations.

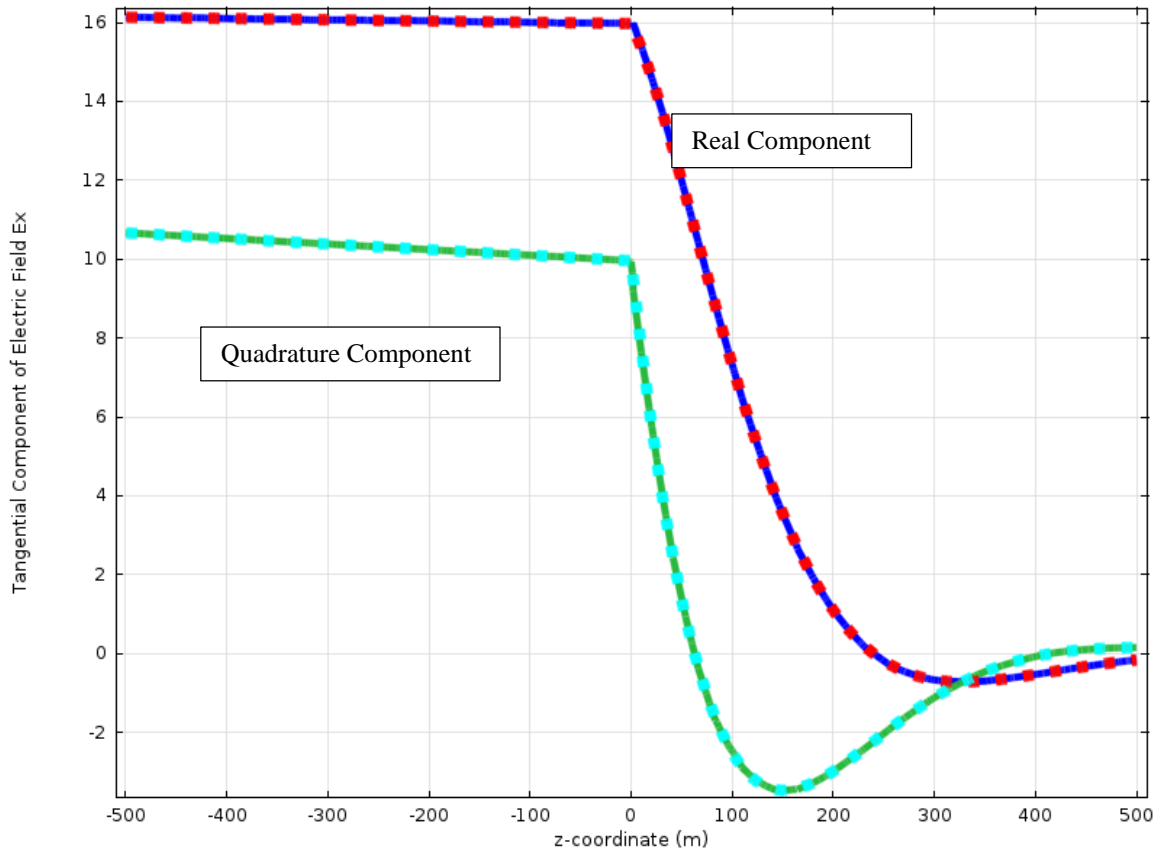


Figure 3.3 Theoretical and simulated tangential component of electric field (E_x) comparisons for homogeneous half-space case at $X=0$ & $Y=0$ along Z axis. Red (Dotted) and blue lines indicate the real component for theory and simulations while cyan (Dotted) and green lines represent the quadrature part for theory and simulations.

Figures 3.4 and 3.5 represent the inphase and Quad plots that are being plotted in a profile at $Z=0$ & $Y=0$ along the X axis for a homogeneous half-space simulation. Since inphase and Quad are both ratios, the Y axes in both figures are in percentage. In a homogeneous half-space with a flat contact between air and ground there is nothing to cause the magnetic field to tilt and there should be no vertical magnetic field components, so the inphase and Quad values should be zero. In figures 3.4 and 3.5, we can see that the

inphase and Quad are both close to zero with values ranging from 0.35% to -0.15% and 0.6% to -0.4%. However, considering the fine scale of the Y axis, these small values can be ignored and considered as numerical errors.

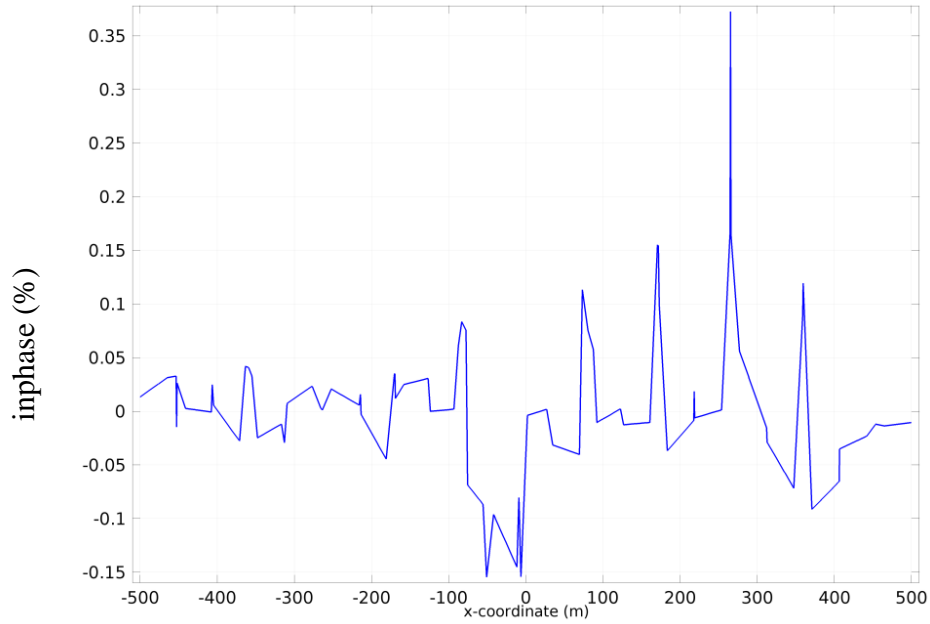


Figure 3.4 Inphase plot of homogeneous half-space simulation at $Z=0$ & $Y=0$ along the X axis.

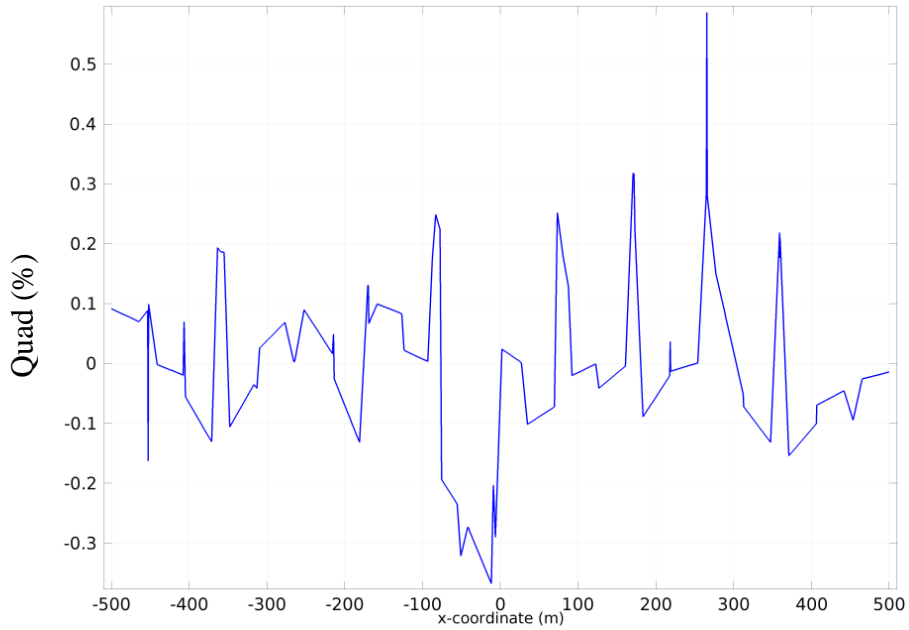


Figure 3.5 Quad plot of homogeneous half-space simulation at $Z=0$ & $Y=0$ along the X axis.

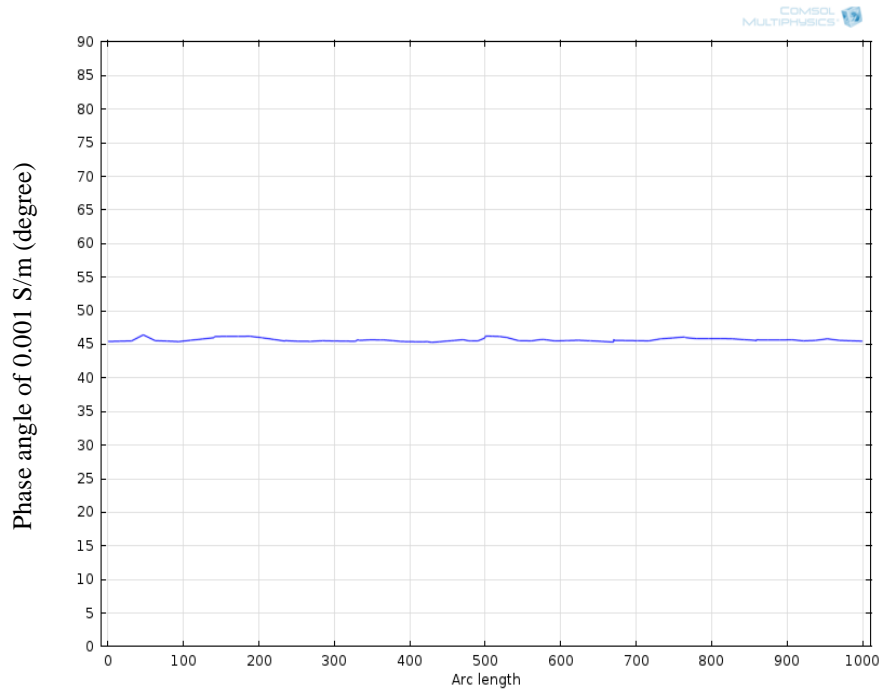


Figure 3.6 Phase angle (degree) between E_x and H_y for homogeneous half-space simulation when ground conductivity is 0.001 S/m at $Z=0$ & $Y=0$ along the X axis.

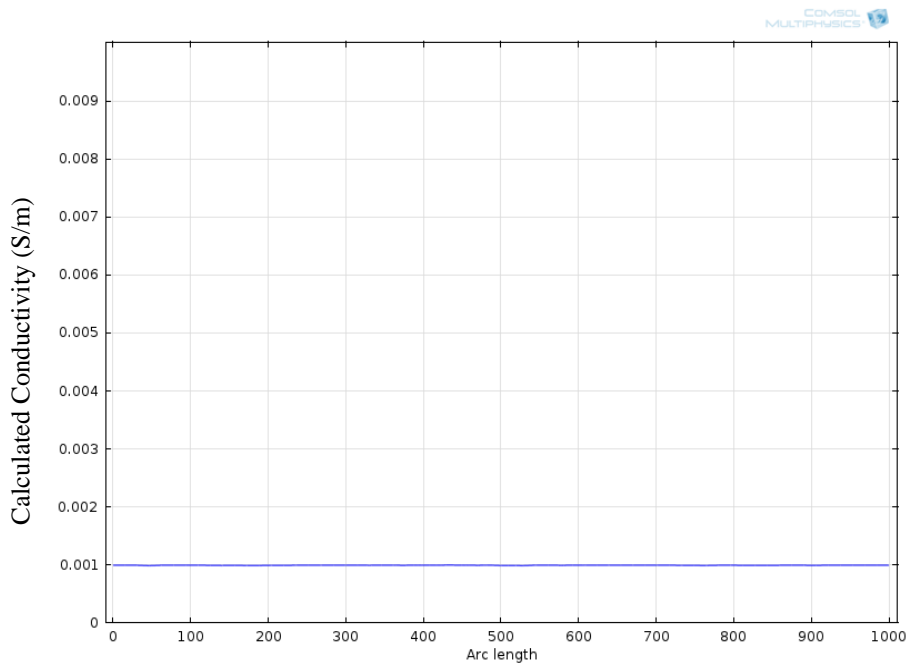


Figure 3.7 Calculated conductivity of homogeneous half-space simulation when ground conductivity is 0.001 S/m at $Z=0$ & $Y=0$ along the X axis.

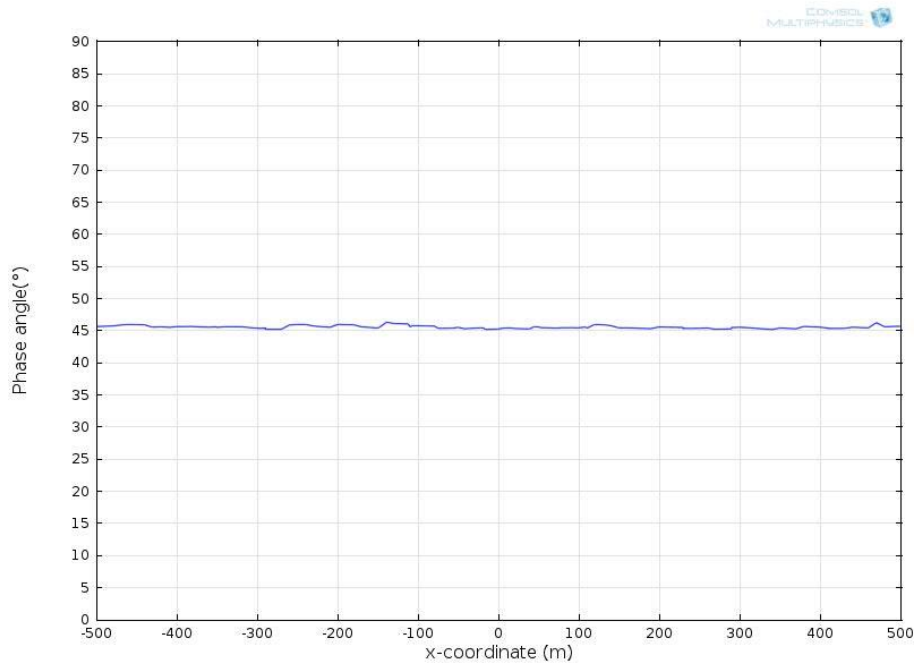


Figure 3.8 Phase angle (degree) between E_x and H_y for homogeneous half-space simulation when ground conductivity is 0.002 S/m at $Z=0$ & $Y=0$ along the X axis.

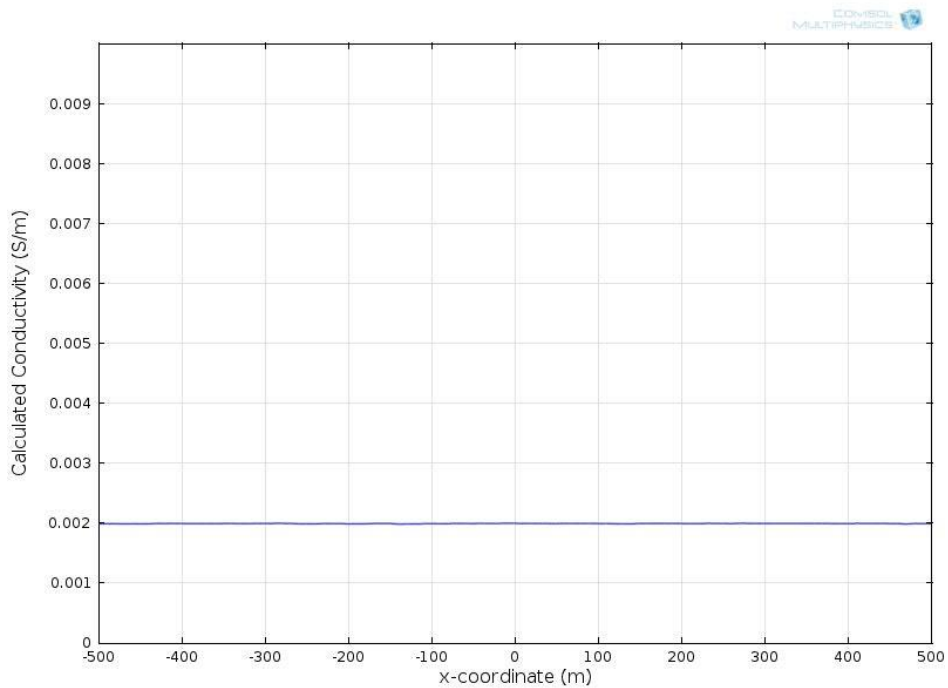


Figure 3.9 Calculated conductivity of homogeneous half-space simulation when ground conductivity is 0.002 S/m at $Z=0$ & $Y=0$ along the X axis.

Figure 3.6 shows the phase of E_x relative to H_y for a simulation of a homogeneous half-space that are plotted horizontally at the vertical center of the model when the ground conductivity is 0.001 S/m. Referring to chapter 2, for the homogenous half-space, the phase shift angle between E_x and H_y should be 45 degrees which also is shown in the figure.

Figure 3.7 shows the calculated conductivity (equation 2.32) for the homogeneous half-space simulation when the ground conductivity is 0.001 S/m. The calculated result is equal to the value inputted in the model.

A different value of ground conductivity of 0.002 S/m is also tested in the model. The phase angle and calculated conductivity are plotted in figures 3.8 and 3.9. In figure 3.8, the values are fluctuating a little. The error could possibly be caused by inadequate model resolution. In the figure 3.9, it can be seen that the conductivity calculated from the model matches the input value.

When the ground is very resistive, the phase angle is not 45 degrees. An extreme case with ground conductivity of $1E-5$ S/m is modeled and 3D simulation results are shown in figure 3.10. In the figure, the arrows indicate current density, the streamlines describe the electric field, and the slices represent the Y component of the magnetic field.

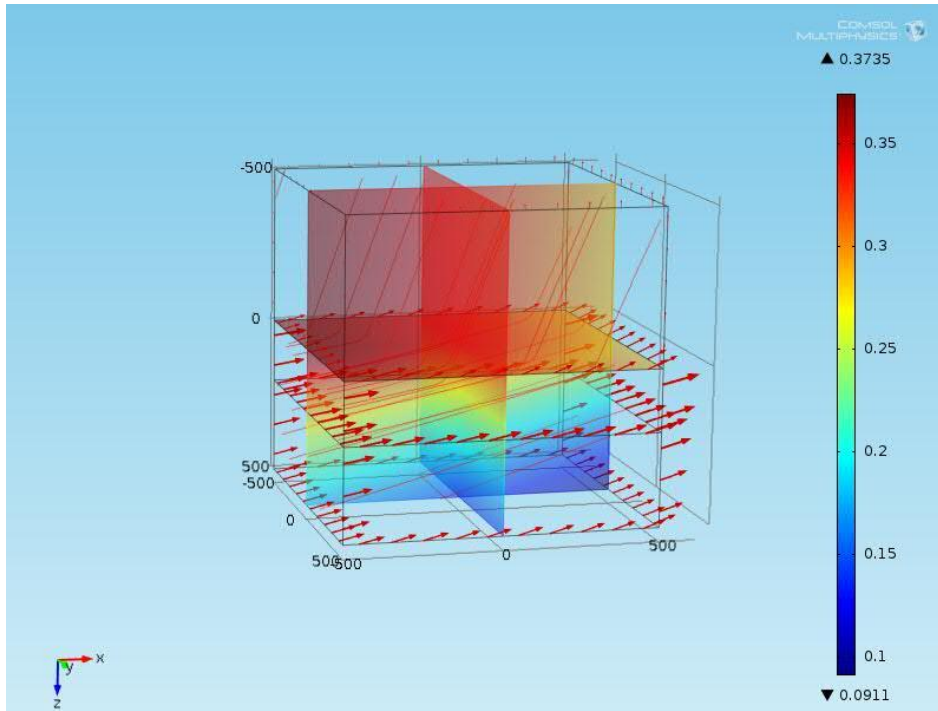


Figure 3.10 3D simulation results of an extremely high resistivity ground

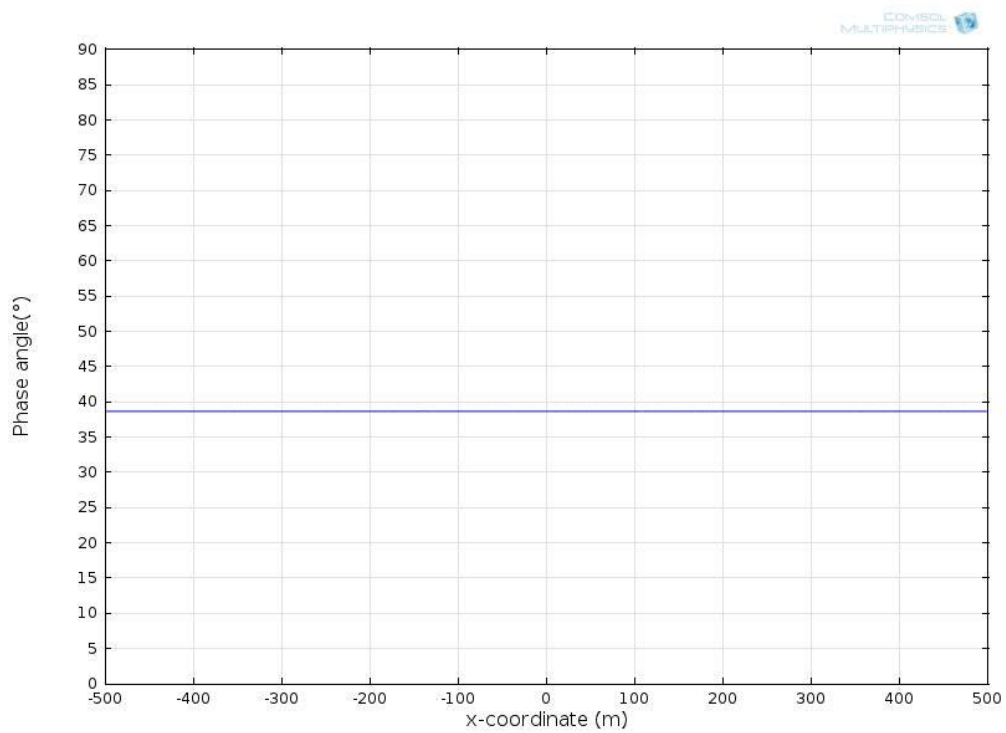


Figure 3.11 Phase angle (degree) between E_x and H_y for homogeneous half-space simulation when ground conductivity is 0.00001 S/m plotted at $Y=0$ & $Z=0$ along the X axis.

Referring to the phase angle section in chapter 2, we indicated that in typical earth materials $k_1 \gg k_0$, and the conduction current flow greatly exceeds the displacement current since $\sigma \gg \omega\epsilon$. However, when ground is very resistive, the conduction current is not much greater than the displacement current. In other words, the assumptions $k_1 \gg k_0$ and $\sigma \gg \omega\epsilon$ are not valid. Referring back to equation 2.28, the

$\left(1 - \frac{k_0^2}{k_1^2} \sin^2 \theta_i\right)^{1/2}$ component cannot be ignored and the phase angle is calculated to

be always less than 45 degree and the result is affirmed in figure 3.11. In this model, the theoretical value of phase angle can be calculated from equation 2.31 to be 38.61 degrees.

Snell's Law states that (with reference to the figure 1.1) the angle θ_t of refracted or transmitted waves are related to the angle of incidence θ_i of the primary wave by (McNeill & Labson, 1991).

$$k_0 \sin \theta_i = k_1 \sin \theta_t. \quad \text{Equation 3.1}$$

When ground is very resistivity (k_1 is not much greater than k_0) for a given angle of incidence, the refracted angle will be significantly greater than 0 and a tilt in the electric field in the ground can be expected. In the figure 3.10, a non-horizontal electric field in the ground can be observed.

3.1.1 ANGLE OF INCIDENCE

In most of the model runs, the angle of incidence θ_i is fixed as $\pi/2 - \pi/40$. The incoming electromagnetic wave is close to parallel to the surface which would have an angle of incidence $\theta_i \cong \pi/2$. However, in reality the angle of incidence varies at each position on Earth's surface for each transmitter.

We carried out a series of calculations to investigate the effects of the angle of incidence. The size of the model is still $1000\text{m} \times 1000\text{m} \times 1000\text{m}$. The frequency and permittivity are the same for the half space modeling. 0 S/m and 0.001 S/m are still the values used for the air and ground electrical conductivity. The angle of incidence is set as $\pi/2 - \pi/20, \pi/2 - \pi/30, \pi/2 - \pi/40, \pi/2 - \pi/50, \pi/2 - \pi/60, \pi/2 - \pi/70$ and $\pi/2 - \pi/80$.

In figure 3.12, the real and quadrature components of the horizontal magnetic fields (H_y) for different angles of incidence are plotted with depth. Based on the prior study of the horizontal magnetic field, it can be expected that the magnetic field will be constant in air and will decay in the ground. This behavior can be observed in every single simulation. However, the amplitude of both the real and quadrature components at the ground surface can be seen to increase with decreasing angle of incidence.

In figure 3.13, the real and quadrature components of the tangential electric fields for different angles of incidence are also plotted. The color legend is the same as the

horizontal magnetic field plot. The decreasing values in air can also be observed. However, when the angle of incidence is smaller, both the real and quadrature component are not constant anymore in air and start to decay. The change in amplitude of all of the measured fields is very similar with angle of incidence and so derived quantities like inphase, Quad, apparent resistivity and phase angle which are ratios, are not strongly affected by the angle of incidence.

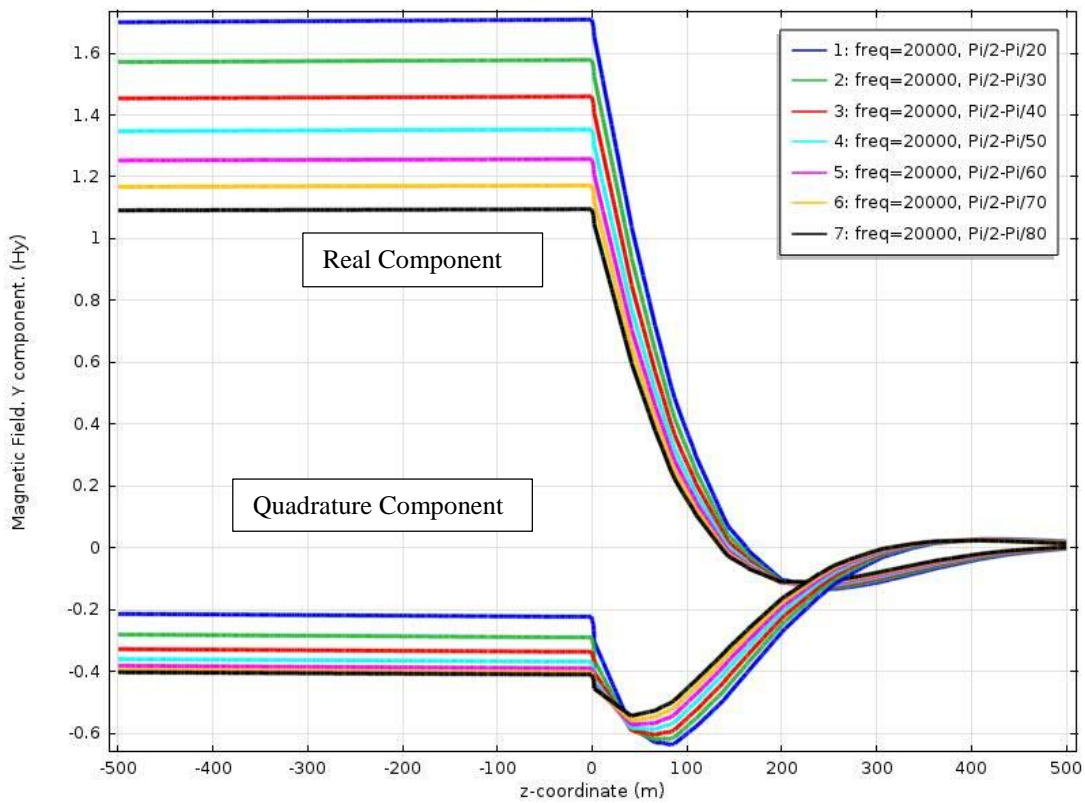


Figure 3.12 Horizontal magnetic fields (H_y) plot for homogenous half-space case with various angles of incidence at $X=0$ & $Y=0$ along the Z axis. The blue, green, red, cyan, magenta, yellow, and black lines represents the results of simulations with incident angles of $\pi/2 - \pi/20$, $\pi/2 - \pi/30$, $\pi/2 - \pi/40$, $\pi/2 - \pi/50$, $\pi/2 - \pi/60$, $\pi/2 - \pi/70$ and $\pi/2 - \pi/80$.

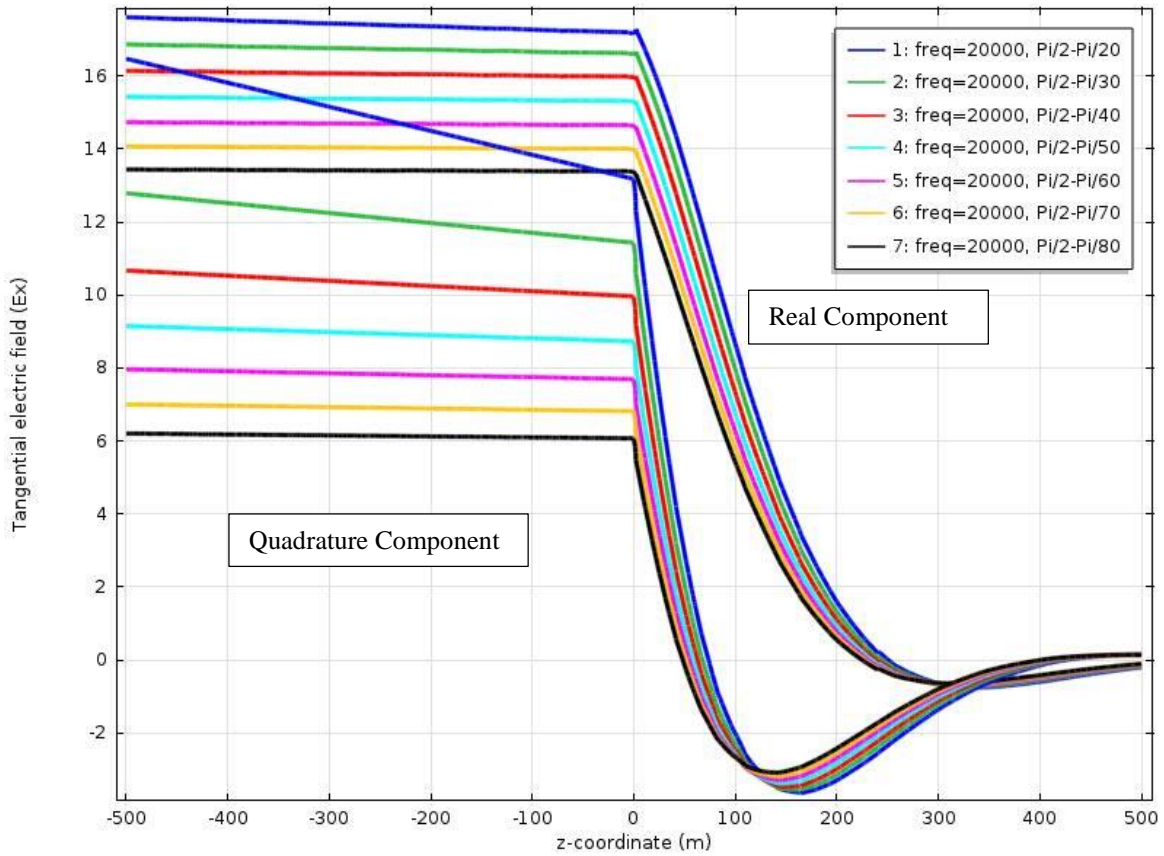


Figure 3.13 Tangential electric fields (E_x) plots for homogenous half-space case with various angles of incidence at $X=0$ & $Y=0$ along the Z axis. The blue, green, red, cyan, magenta, yellow, and black lines represents the results of simulations with incident angles of $\pi/2 - \pi/20$, $\pi/2 - \pi/30$, $\pi/2 - \pi/40$, $\pi/2 - \pi/50$, $\pi/2 - \pi/60$, $\pi/2 - \pi/70$ and $\pi/2 - \pi/80$.

Figures 3.14 and 3.15 show the inphase and Quad plots for the homogenous half-space model with various angles of incidence. As seen, the field measurement elements are not affected by different angles of incidence in the homogeneous half-space model and remain close to 0.

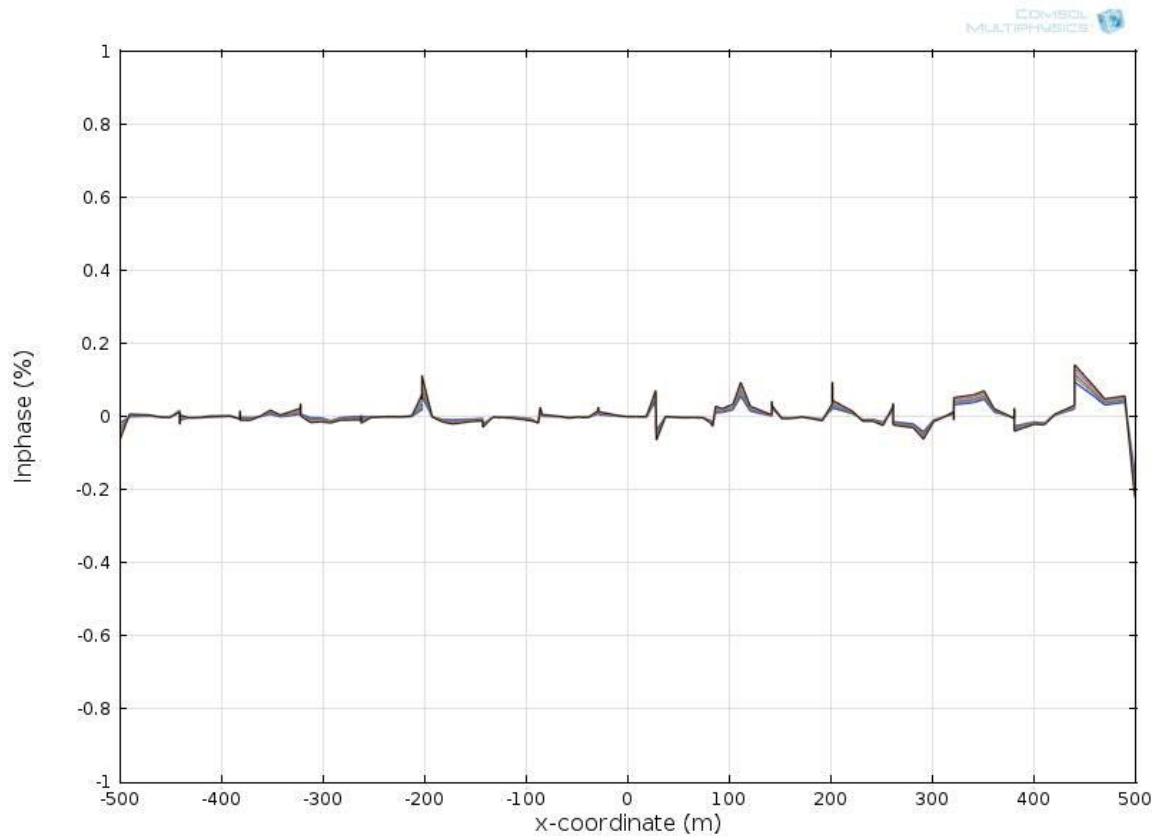


Figure 3.14 Inphase plot of homogeneous half-space simulation with various angles of incidence at $Z=0$ & $Y=0$ along the X axis. The blue, green, red, cyan, magenta, yellow, and black lines represents the results of simulations with incident angles of $\pi/2 - \pi/20$, $\pi/2 - \pi/30$, $\pi/2 - \pi/40$, $\pi/2 - \pi/50$, $\pi/2 - \pi/60$, $\pi/2 - \pi/70$ and $\pi/2 - \pi/80$. In the figure, all the lines lie on top of one another.

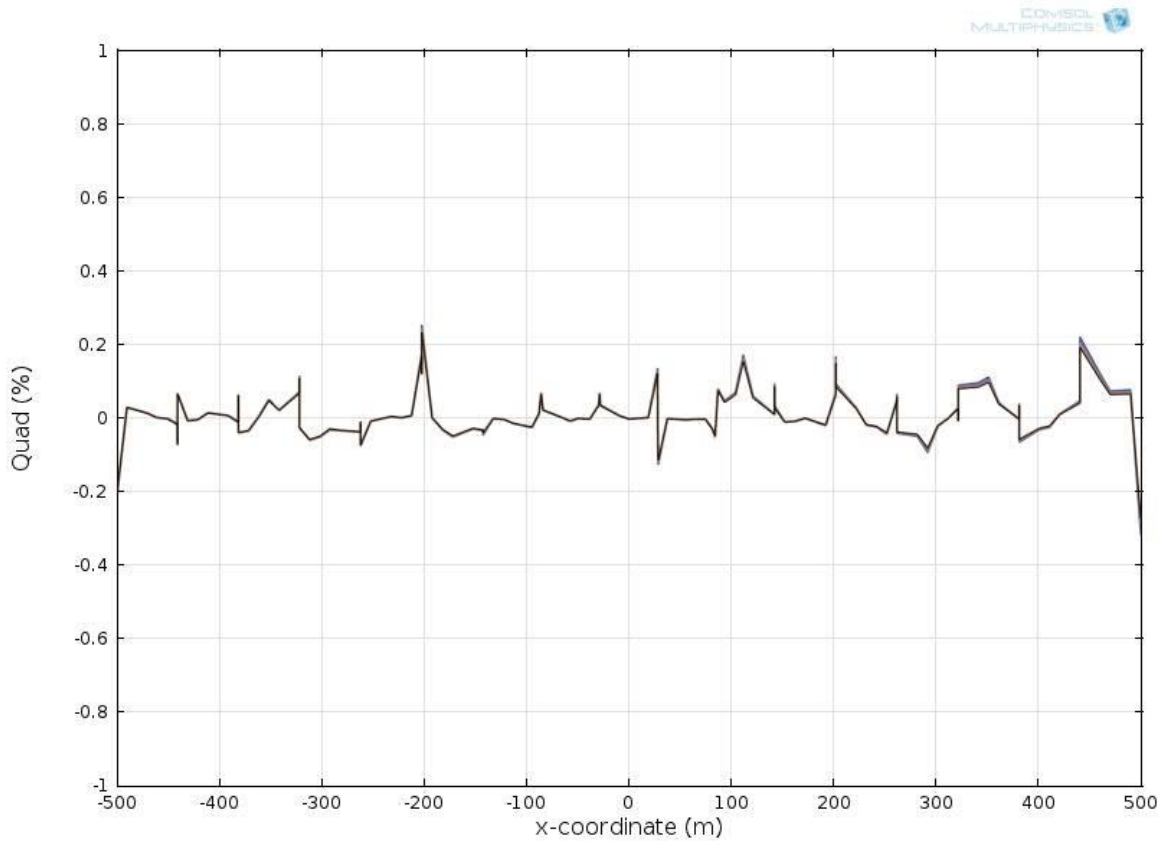


Figure 3.15 Quad plot of homogeneous half-space simulation with various angles of incidence at $Z=0$ & $Y=0$ along the X axis. The blue, green, red, cyan, magenta, yellow, and black lines represents the results of simulations with incident angles of $\pi/2 - \pi/20$, $\pi/2 - \pi/30$, $\pi/2 - \pi/40$, $\pi/2 - \pi/50$, $\pi/2 - \pi/60$, $\pi/2 - \pi/70$ and $\pi/2 - \pi/80$. In the figure, all the lines lie on top of one another.

Figure 3.16 and 3.17 shows the phase angle and calculated conductivity plots for the homogenous half-space model with various angles of incidence. As also can be seen, they are not affected by different angles of incidence in a homogeneous half-space model.

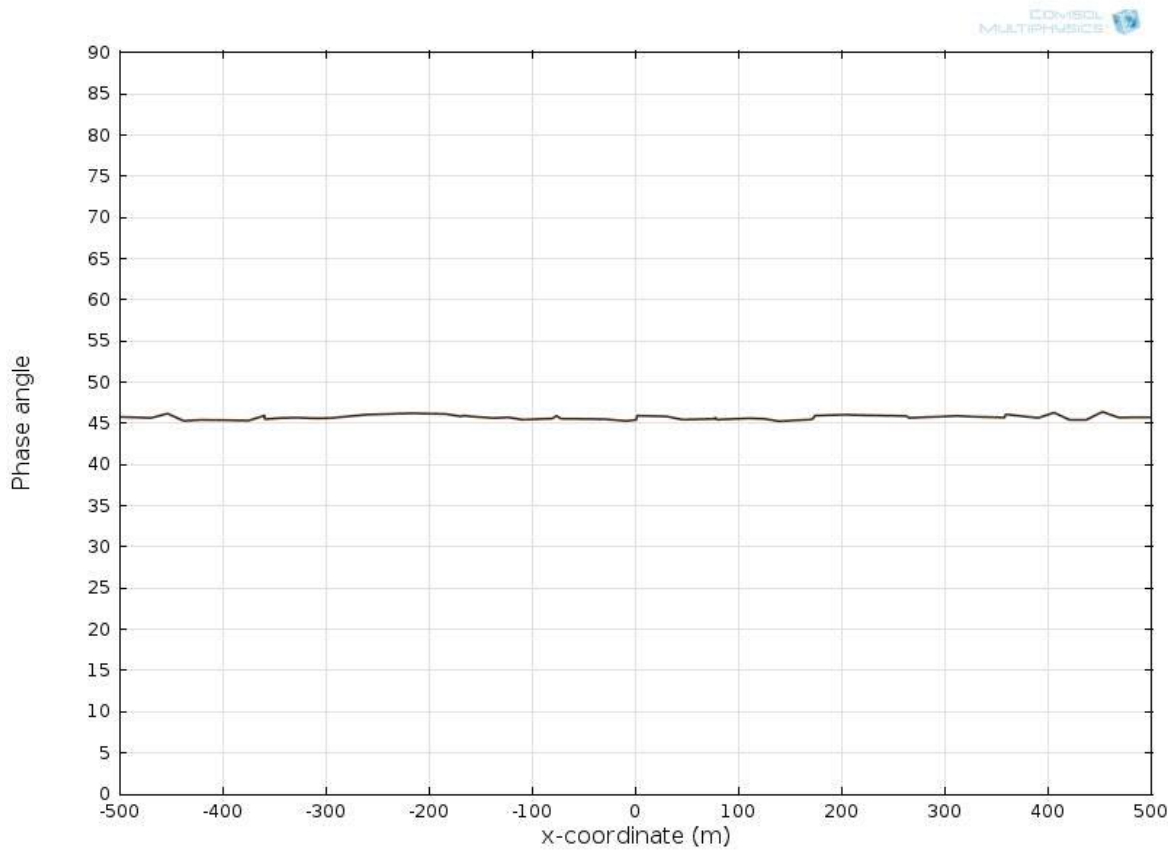


Figure 3.16 Phase angle plot of homogeneous half-space simulation with various angles of incidence at $Z=0$ & $Y=0$ along the X axis. In the figure, all the lines lie on top of one another.

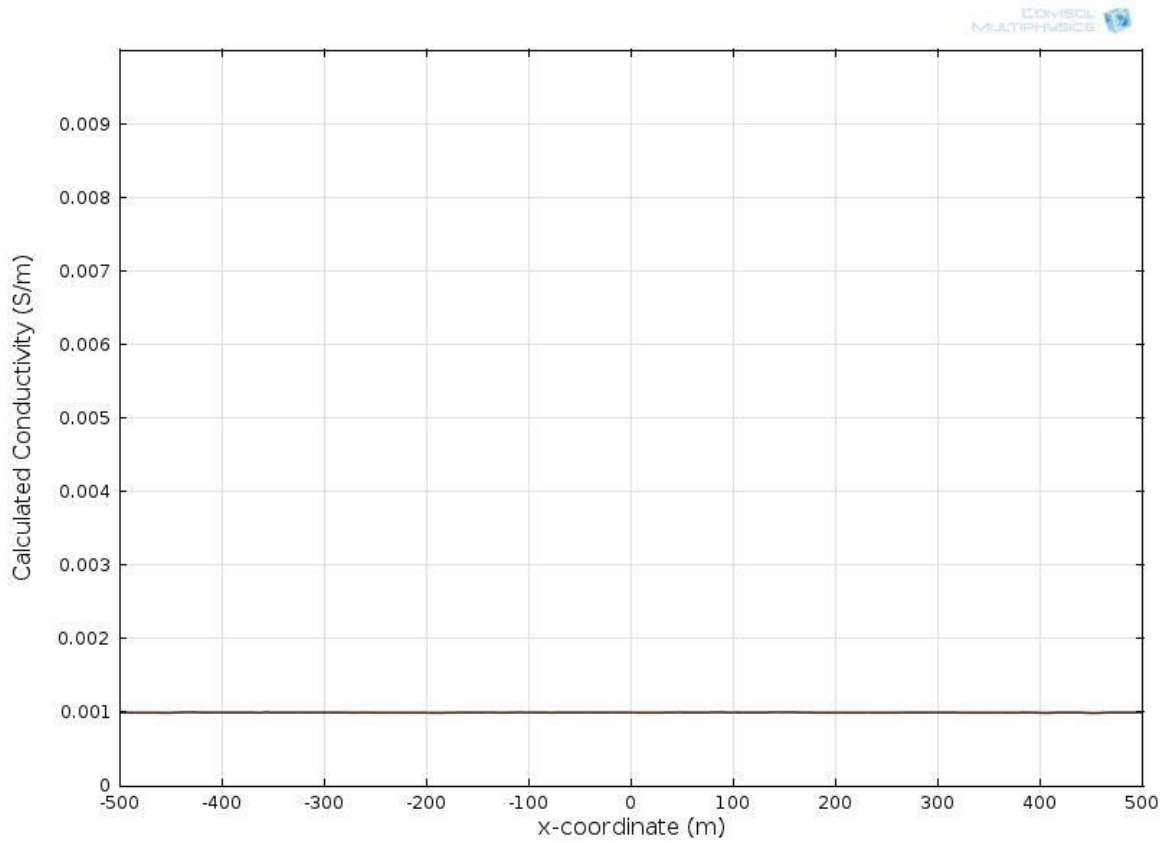


Figure 3.17 Calculated conductivity plot of homogeneous half-space simulation with various angles of incidence at $Z=0$ & $Y=0$ along the X axis. In the figure, all the lines lie on top of one another.

3.2 TWO LAYER EARTH MODELING

A two-layer earth is also modeled using Comsol software that is modified from the homogenous half-space model. The model parameters such as angle of incidence, frequency of the electromagnetic wave and model geometry are the same as in the homogeneous half-space model. The magnetic field on the outer boundaries is specified using equations 2.15, 2.19 and 2.20. In the model, a second layer is added at the depth h of 200m. For the example shown here, the top and lower layers have electrical conductivities 0.001 S/m and 0.01 S/m. In the top medium there are both upgoing and downgoing waves, and in the lower medium there is only a downgoing wave.

The simulation results and theoretical solutions of the horizontal magnetic field Y component (H_y) and the tangential component of the electric field (E_x) are plotted in figures 3.18 and 3.19. Real and quadrature components are indicated in the figures. In both plots, the red and blue colors represent the real components of simulated and theoretical solutions, while the cyan and green colors represent the quadrature components. As seen, the real and quadrature components of the simulation results still match ones from theoretical solutions. In figure 3.18, comparing with prior plots from homogenous half-space models, discontinuous derivative points can be observed at 200m depth where the resistivity changes discontinuously.

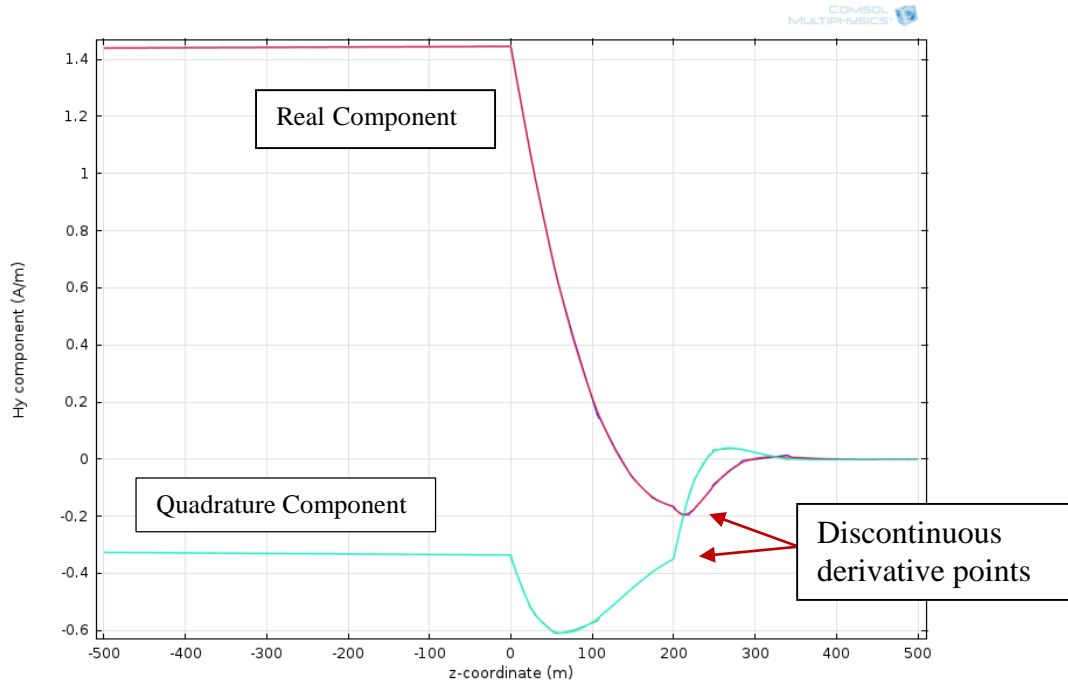


Figure 3.18 Theoretical and simulated magnetic field Y component (H_y) comparisons for two layers earth case at $X=0$ & $Y=0$ along the Z axis.

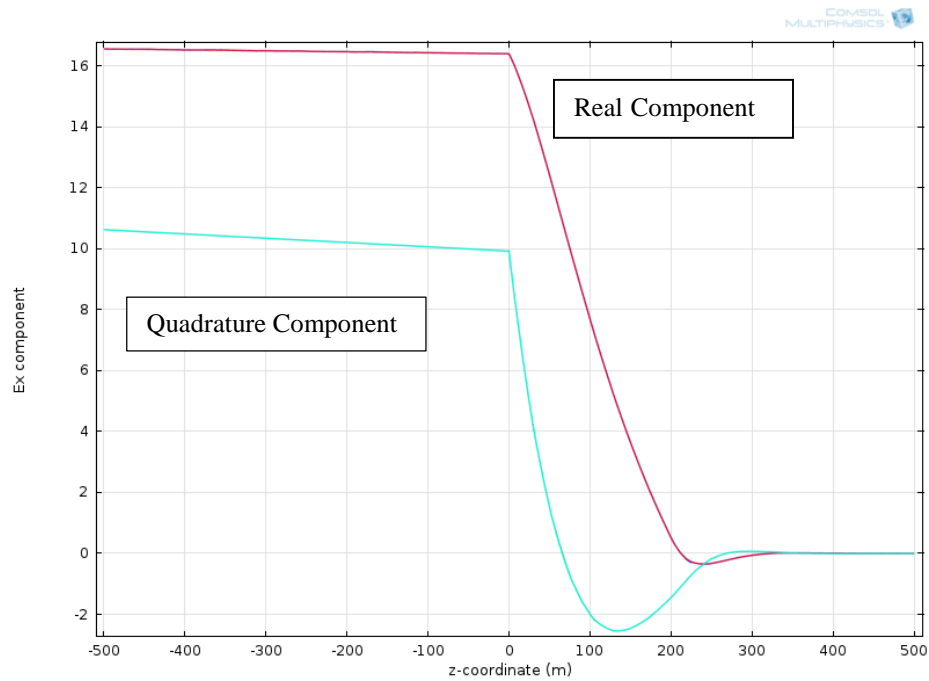


Figure 3.19 Theoretical and simulated tangential component of electric field (E_x) comparisons for two layers earth case at $X=0$ & $Y=0$ along the Z axis.

Referring to chapter 2 equation 2.34, the electrical skin depth is controlled by both the conductivity and frequency and it is an estimate of how deeply the VLF signals penetrate into the ground. Based on the equation, for a perfectly resistive overburden, all of the VLF signal will penetrate the layer and make the top layer “invisible”. In contrast, for perfectly conductive overburden, all of the VLF signal will be blocked by the top layer and the lower layer will be undetected. In both end members, the resistivity value of the top layer greatly affects the measured VLF signal.

In the two layer earth simulation, different conductivity contrasts for the top and lower layers are analyzed. In the Comsol model, model parameters such as angle of incidence, frequency of electromagnetic wave and model geometry are the same as those employed in section 3.1. The domain of the model is decreased to 100m*100m*100m due to the small values of the skin depth, and the horizontal contact is located at 20 m depth. The lower layer conductivity remains 0.01 S/m. The top layer conductivity is given values of 0.2 S/m, 0.01 S/m and 0.0005 S/m.

Figures 3.20 & 3.21 are the theoretical and simulation results of horizontal magnetic field (H_y) and tangential component of electric field (E_x) with different conductivity values of the top layer. In both figures, the red color represents the case when the conductivity ratio is 0.05 (conductivity of the top layer/conductivity of the lower layer), the green represents the case when the conductivity ratio is 1 (which is also the homogeneous half-space case), and the blue represents the case when the conductivity ratio is 20. As seen, the horizontal magnetic field in air ($Z < 0$) becomes greater with a more conductive

top layer, while the tangential electric field in air becomes smaller. In figure 3.20, at 20m depth where the top layer and second layer interface occurs, only the model run with a conductivity of 0.0005 S/m has the discontinuous derivative point. These results can be explained by considering the skin depth. For the three different conductivity input values, the top layer skin depths can be calculated as roughly 7.96m when the top layer conductivity is 0.2 S/m, 35.6m when the top layer conductivity is 0.01 S/m and 159.15m when the top layer conductivity is 0.0005 S/m. When the top layer skin depth is smaller than the layer thickness, the horizontal magnetic field component in the top medium is decaying faster and a discontinuous derivative point cannot be observed at the interface between the different materials.

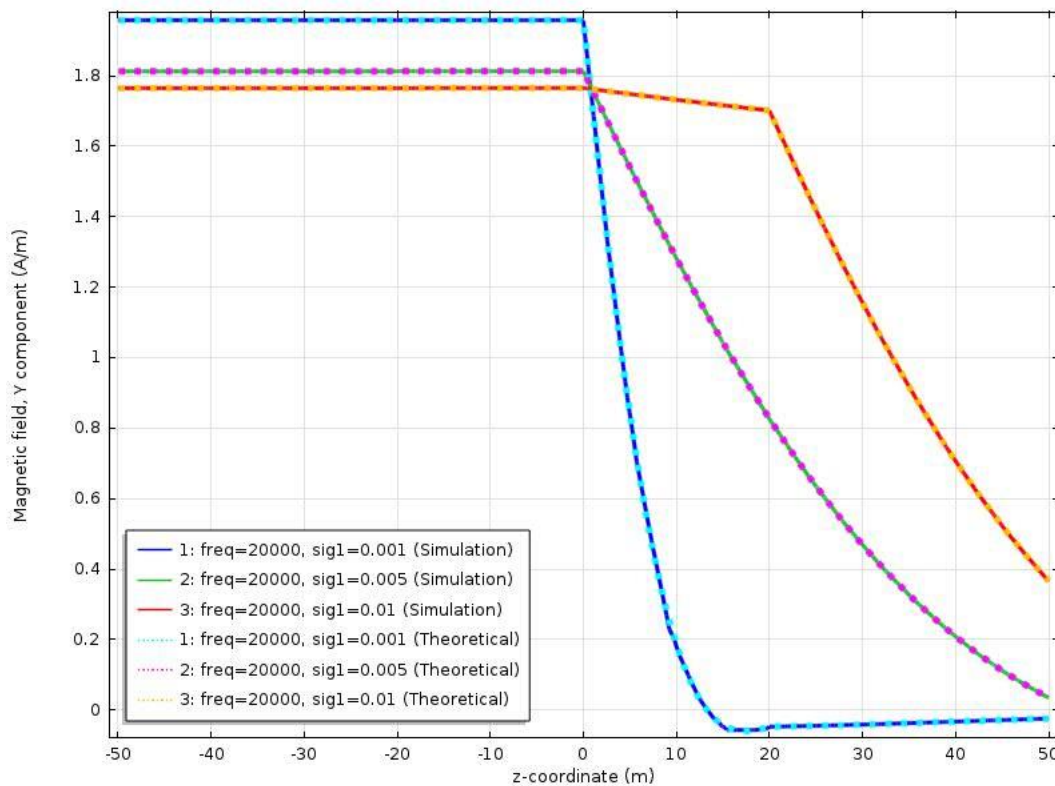


Figure 3.20 Horizontal magnetic field plots with different conductivity values of the top layer in a two layers earth model at X=0 & Y=0 along the Z axis.

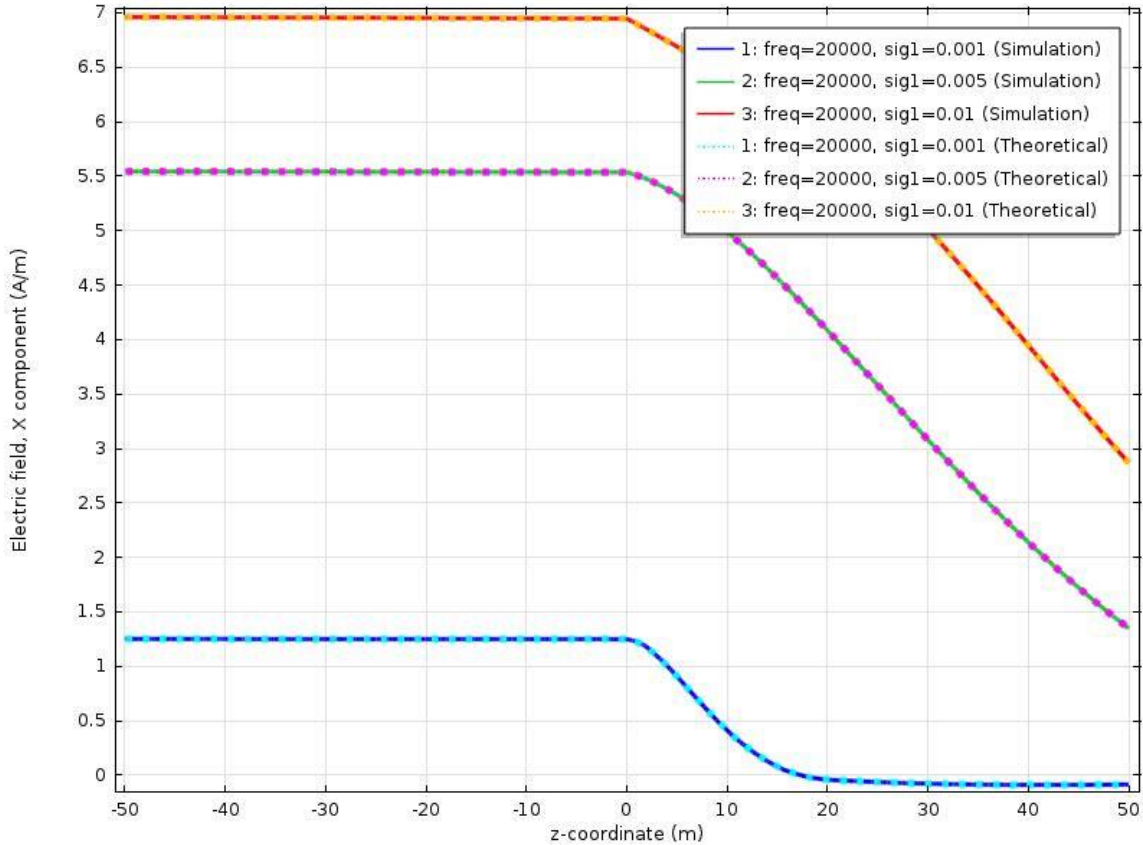


Figure 3.21 Tangential electric field plots with different conductivity values of the top layer in a two layers earth model at X=0 & Y=0 along the Z axis.

A flat surface with horizontal contacts between different layers will not produce any vertical components of the magnetic field and inphase, Quad and Tilt angle will all be zero.

The most useful measurement to determine the layer structure is the phase angle. It can be shown that the phase angle is 45 degrees for a homogeneous half-space case with not very resistive ground. If the earth has two layers, the phase angle measured on the surface departs from 45 degree which gives valuable information about the resistivity of the

layers. The phase angle will usually be bigger than 45 degree if the conductivity increases with depth. While if the conductivity of earth decreases with depth, the phase will be smaller than 45 degree (Reynolds, 1997). Figure 3.22 indicates the different phase angle simulation results at different conductivity values of the top layer for the two layer model. The phase angles calculated from equation 2.31 at the given conductivities of the top layer of 0.2 S/m 0.01 S/m & 0.0005 S/m are 45.45 degrees, 44.995 degrees and 62.915 degrees, which are similar to what is calculated from the numerical model (figure 3.22). In the case when the top layer conductivity is 0.2 S/m, the phase angles from the simulation and the theoretical calculations are both close to 45 degrees instead of having values less than 45 degrees. When the top layer skin depth is smaller than the layer thickness, the electromagnetic wave in the top medium is decaying faster and the interface between the different materials is harder to detect.

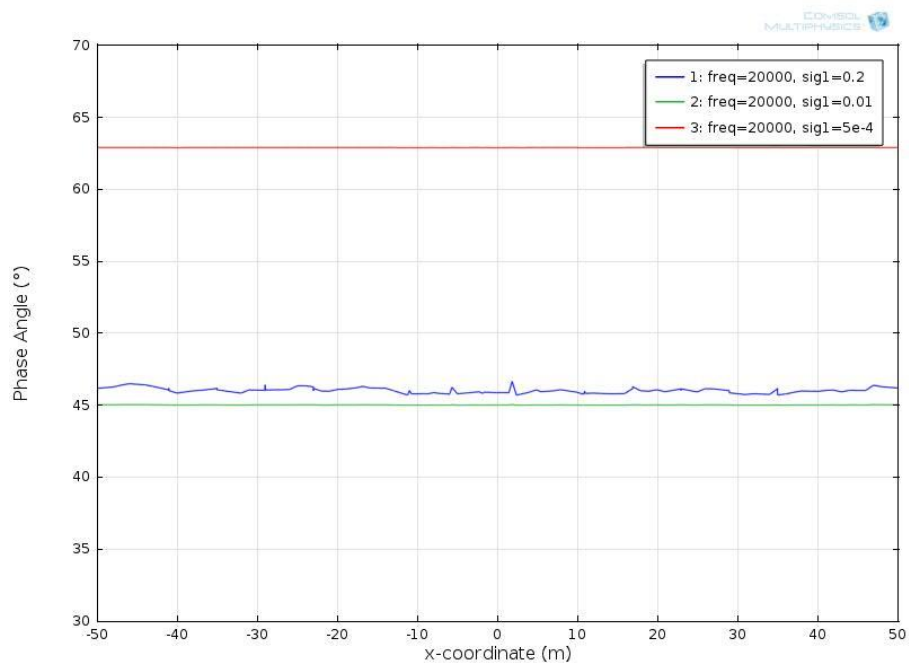


Figure 3.22 Phase angle plots with different conductivity values of the top layer in a two layer earth model at $Z=0$ & $Y=0$ along the X axis.

A two layer Earth was further studied by varying the depth to the interface when the top layer had conductivity 0.0001 and the lower layer 0.01 S/m. The geometry of the model is changed to 1000m*1000m*1000m, and the interface depths used were 100m, 200m, 300m and 400m.

Figures 3.23 & 3.24 display the tangential electric field (E_x) and horizontal magnetic field (H_y) change with different thickness of overburden. In all four simulations, the skin depth value is 356m in the top layer. As shown, when the thickness approaches the skin depth value, the values of E_x and H_y in air are approaching a constant and stable value as both green and purple colors show. In figure 3.24, the discontinuous derivative points of the horizontal magnetic field can still be observed at the interface between two different layers.

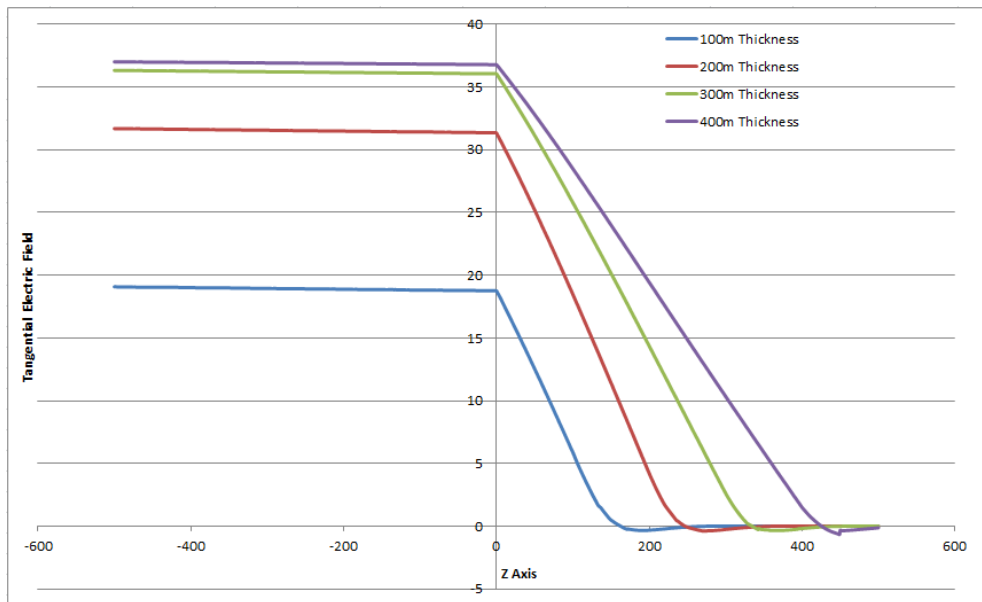


Figure 3.23 Tangential electric field plots with different upper layer thickness of two layers earth model at $X=0$ & $Y=0$ along the Z axis.

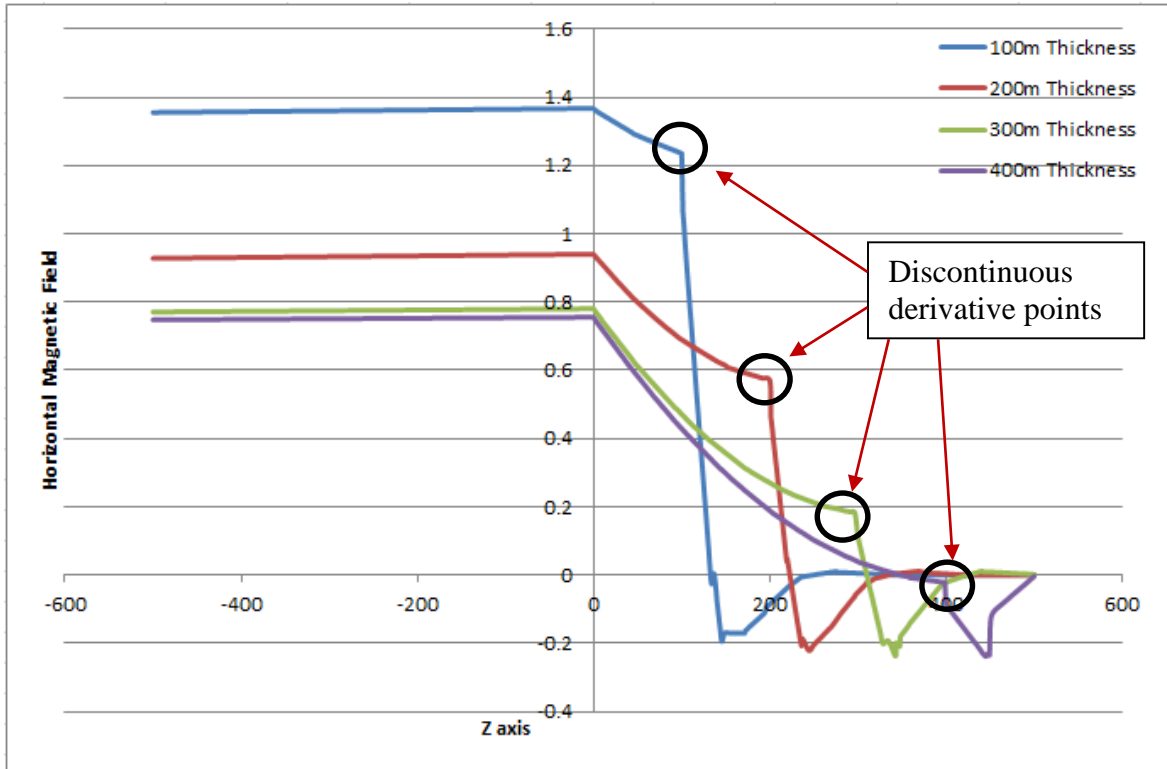


Figure 3.24 Horizontal magnetic field plots with different upper layer thickness of two layers earth model at $X=0$ & $Y=0$ along the Z axis.

As indicated in figure 3.25, if the ground conductivity increases with depth, the phase angle will be larger than 45 degree. In all four simulations, the phase angles are larger than 45 degree, and they decrease with the increasing thickness of overburden. The phase angles calculated from equation 2.31 at the top layer thickness of 100m, 200m, 300m and 400m are 76.88 degrees, 71.69 degrees, 61.492 degrees and 52.08 degrees, which are similar to what is calculated from the numerical model shown in the figure 3.25.

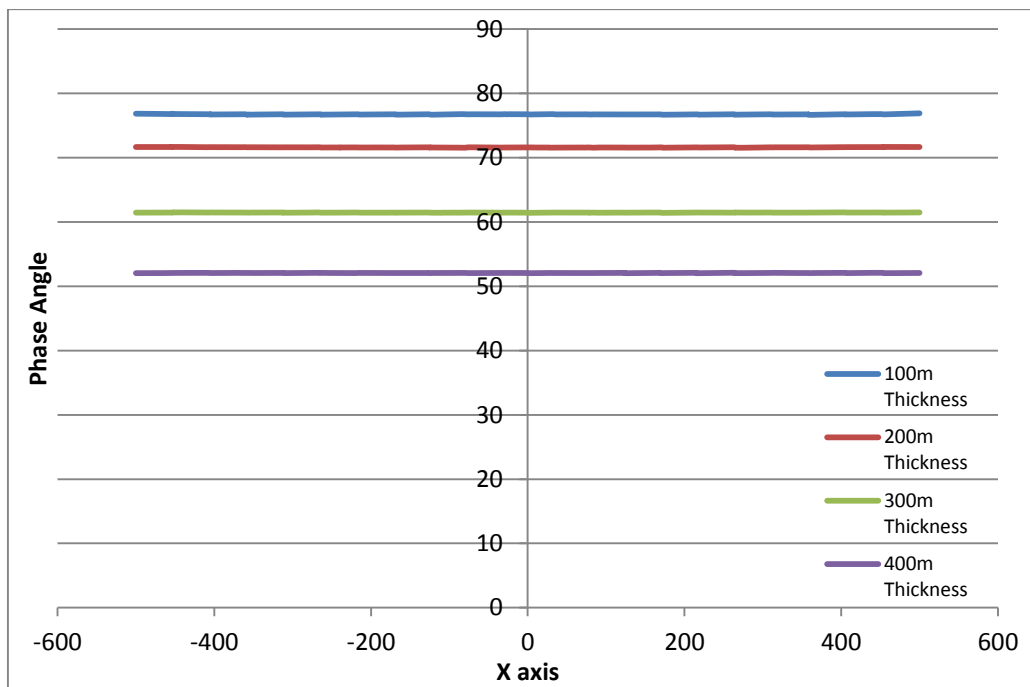


Figure 3.25 Simulated results of phase angles with different upper layer thickness of two layer earth model

3.3 VERTICAL CONTACT MODELING

The prior study indicates the behaviors of a VLF wave propagating over a horizontal contact. The VLF plane wave response of a vertical contact in the ground is discussed in detail here. Unlike a horizontal contact, there is no mathematical solution for a vertical contact although an approximate solution exists (d'Erceville & Kunetz, 1962).

As indicated in section 3.1, a plane electromagnetic (EM) wave is characterized by a direction of propagation and the electric field and the magnetic field are perpendicular to each other and to the direction the plane wave is propagating ("Polarization of Plane Waves,"). Unlike the horizontal contact in the ground, the wave can be propagating at various angles relative to the strike of the contact and the response depends strongly on this angle.

There are two extreme cases, E-polarization and H-polarization. E-polarization, which is also called the TE mode, has the direction of wave propagation parallel to the strike of the vertical contact. The horizontal electric field in the ground is in the same direction as the wave propagation and it is also parallel to the strike of the contact. In contrast, when the plane wave propagation direction is perpendicular to the strike of the vertical contact, it is called H-polarization or TM mode. In this case the magnetic field is parallel to the strike direction. The responses of E-polarization or H-polarization are very different. The response of a plane wave propagating in a random direction relative to the strike of a

vertical contact can be decomposed into E and H polarization components (McNeill & Labson, 1991).

In modeling a vertical contact, the earth is divided into two parts with a vertical contact between each part and the contact between air and ground is still horizontal. We apply boundary conditions appropriate for the homogeneous half-space situation. However, since different ground properties are involved in modeling, different coefficients are needed for the magnetic field applied on either side of the vertical contact for both air and ground. The boundary condition equations used are shown below. In those equations, $a_{0(1)} = a_{0(2)} = 1$, $b_{0(1)}$ and $b_{0(2)}$ refer to the different amplitudes of magnetic field in air on each side of the vertical contact. $a_{1(1)}$ and $a_{1(2)}$ refer to the different amplitudes of down going magnetic field of different ground materials. Note also that these boundary conditions are only approximately correct since they are actually appropriate for an infinite half-space.

$$\text{In air1} \quad H_{oy(1)} = (a_{0(1)}e^{-u_0z} + b_{0(1)}e^{u_0z})e^{-i\lambda x} \quad \text{Equation 3.2}$$

$$\text{In air2} \quad H_{oy(2)} = (a_{0(2)}e^{-u_0z} + b_{0(2)}e^{u_0z})e^{-i\lambda x} \quad \text{Equation 3.3}$$

$$\text{In ground1} \quad H_{1y(1)} = a_{1(1)}e^{-u_1z}e^{-i\lambda x} \quad \text{Equation 3.4}$$

$$\text{In ground2} \quad H_{1y(2)} = a_{1(2)}e^{-u_1z}e^{-i\lambda x} \quad \text{Equation 3.5}$$

3.3.1 VERTICAL CONTACT: H-POLARIZATION

H-polarization indicates that the horizontal magnetic field is parallel to the contact strike as illustrated in figure 3.26. In the model, the electromagnetic wave is set coming along the X axis and the magnetic field is perpendicular to it as indicated by the arrows in figure 3.27. The streamlines describe the current flow direction in the ground. The slice plot represents the horizontal component of the magnetic field which ranges from 1.9204 A/m to -0.1803 A/m. The model domain has a size of 200m*200m*200m. 20 kHz frequency is used for the plane wave when modeling and the angle of incidence is $\pi/2 - \pi/40$. $\sigma_1 = 0.05$ S/m ($X < 0$) and $\sigma_2 = 0.01$ S/m ($X > 0$) are the values used for the ground electric conductivity.

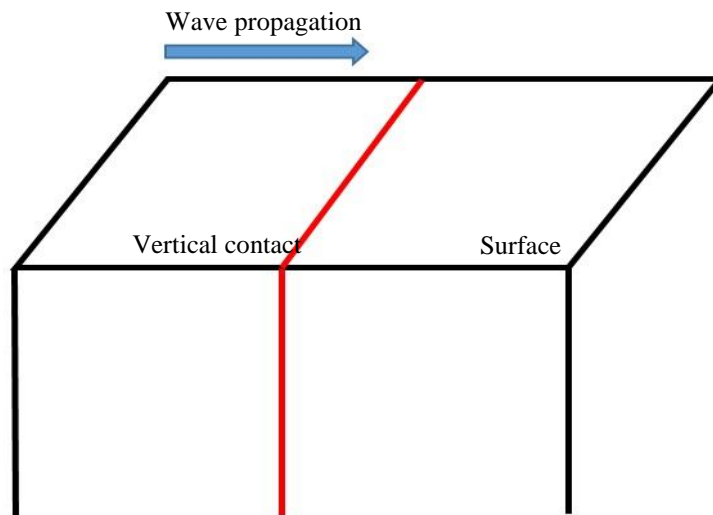


Figure 3.26 3D view of H- polarization. The blue arrow indicates the wave propagation direction in the air, and red line indicates the strike of the vertical contact.

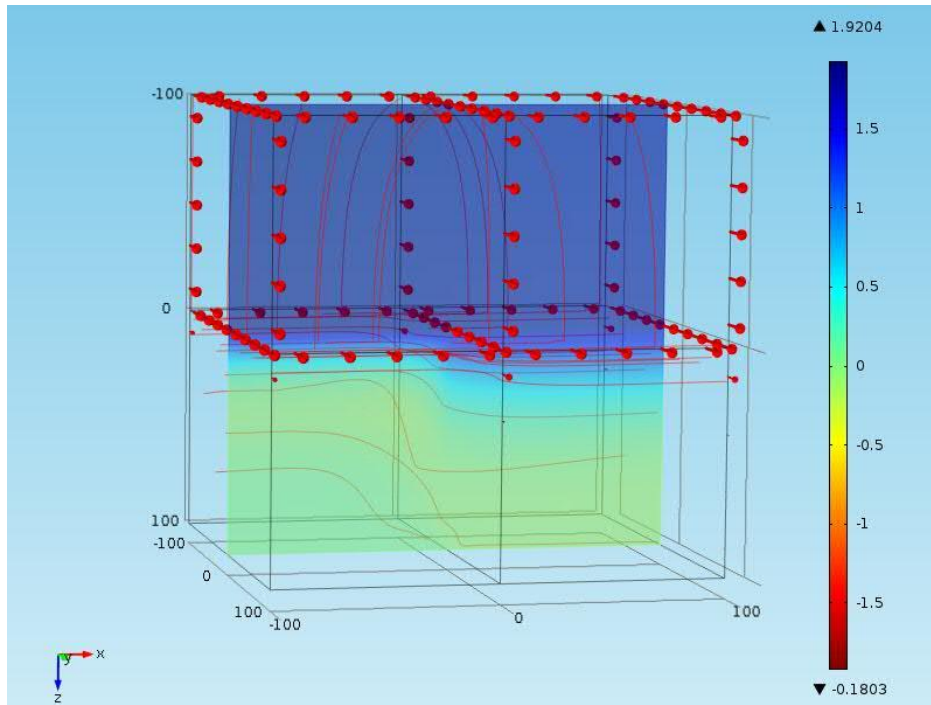


Figure 3.27 3D simulation results of H-polarization. The streamlines describe the current flow direction in the ground. The slice plot represents the horizontal component of the magnetic field

As the simulation results show in figure 3.27, the magnetic field on the surface shows no variation when crossing the strike of the contact. This can be simply explained at a large distance away from the contact on either the 0.05 S/m or 0.01 S/m side; it is a homogeneous half-space situation and it has constant electric field and magnetic field in the air. However, due to different ground electrical conductivities, the skin depths on either side of the contact are different which affects the rate at which the horizontal magnetic field drops to zero. As illustrated in figure 3.28, in a more conductive layer, the horizontal magnetic field decays faster than in a less conductive layer.

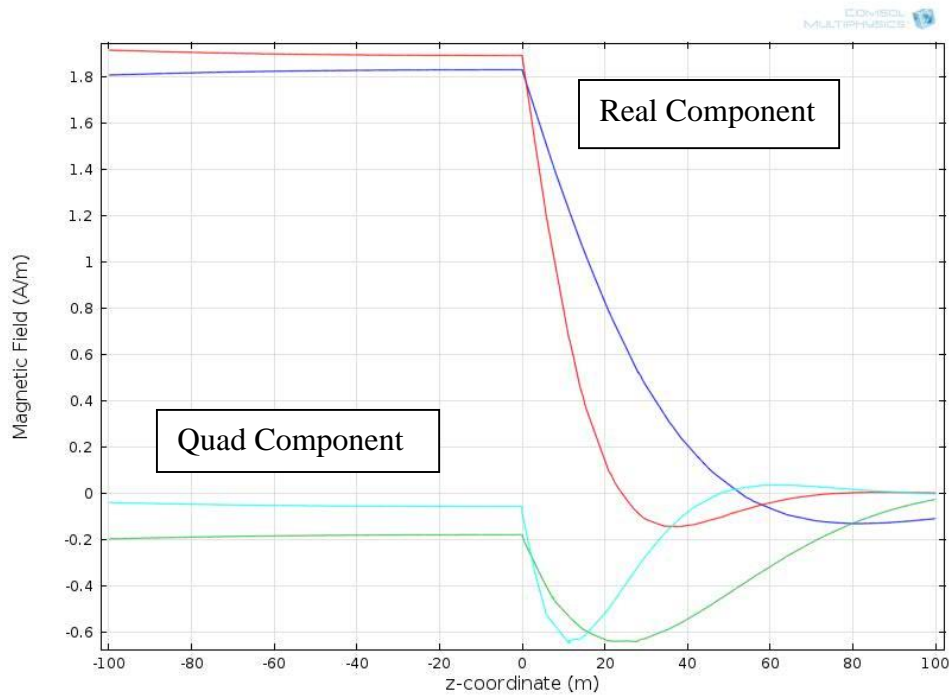


Figure 3.28 Horizontal magnetic field component plot of H-polarization. The red and cyan lines are the real and quadrature components of the horizontal magnetic field in the higher conductivity side, and the blue and green lines are the real and quadrature components of horizontal magnetic field in the less conductive side. Both vertical profiles are picked far away from the vertical contact.

The streamlines in figure 3.27 indicate that the current is deflected downward when passing through the contact from the higher conductivity medium to the lower conductivity one. Based on the general law of continuity of current and $\mathbf{J} = \sigma \mathbf{E}$, the same amount of current must be running through the different material, and a different voltage gradient is required. This illustrates that charges are induced at the interface so as to alter the electric field and maintain current continuity. Based on these principles, it can be shown that (McNeill & Labson, 1991),

$$\frac{E_{1x}}{E_{2x}} = \frac{\sigma_2}{\sigma_1}$$

Equation 3.6

Equation 3.6 indicates that the electric field changes discontinuously across the interface and this result can also be observed in figure 3.29. The figure is plotted on the surface along the X axis which is perpendicular to the strike of the vertical contact. In figure 3.29,

$\frac{E_{1x}}{E_{2x}}$ is approximately 0.22 which is similar to the ratio of conductivities set in the model

at 0.2.

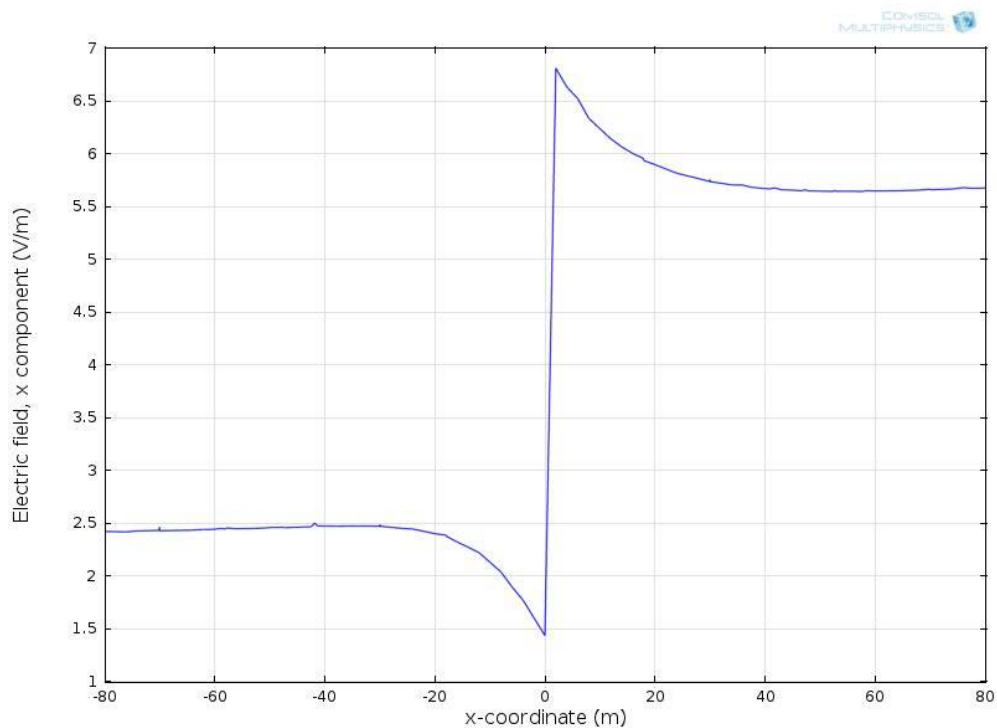


Figure 3.29 Tangential electric field component (Ex) plot of H-polarization at Z=0 & Y=0 along the X axis.

In the H-polarization case, the magnetic field is parallel to the vertical contact and no tilted component can be observed. Therefore there is no reading of inphase, Quad or Tilt on the surface. Figure 3.30 displays the inphase colored blue and Quad colored green plot along the X axis crossing the interface on the surface. Figures 3.31 and 3.32 are plots of the simulated vertical magnetic field reading and tilt angle. In all three, the values are changing by a small amount and can be considered as numerically zero.

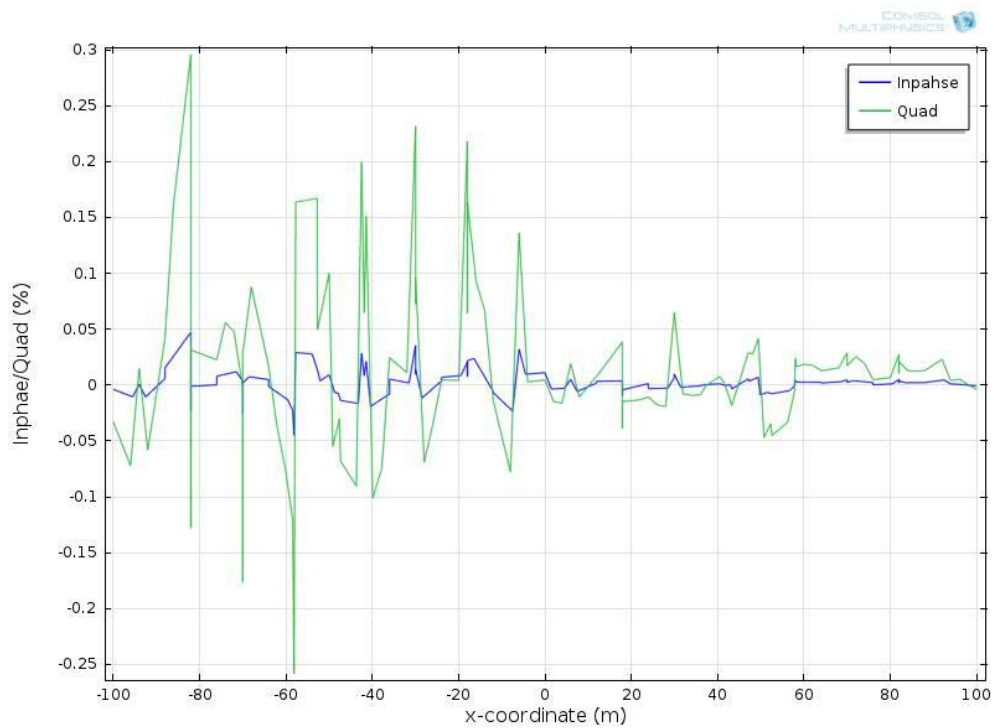


Figure 3.30 inphase/Quad plots of H-polarization at Z=0 & Y=0 along the X axis.

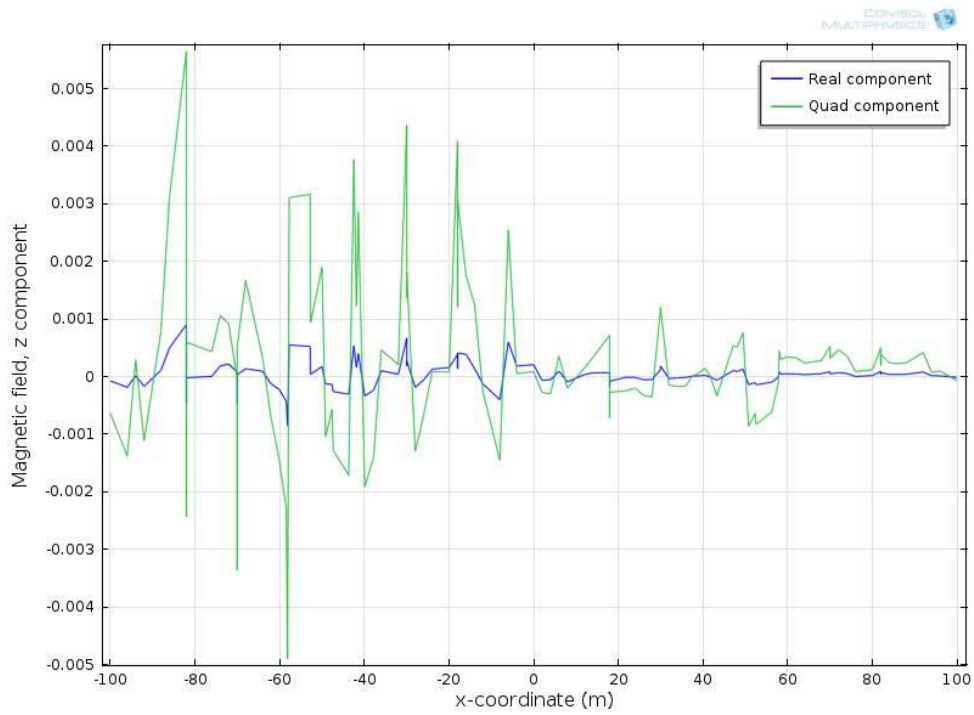


Figure 3.31 Vertical magnetic field component plot of H-polarization at Z=0 & Y=0 along the X axis.

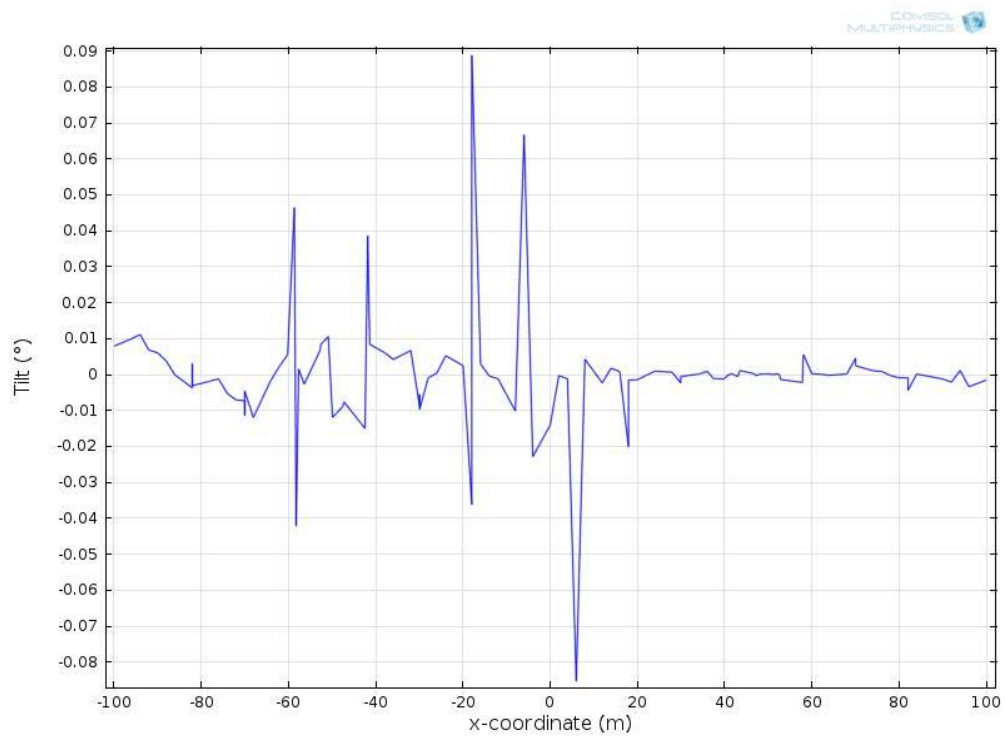


Figure 3.32 Tilt plot of H-polarization at Z=0 & Y=0 along the X axis

The horizontal electric field varies across the contact and quantities that depend on this field allow detection of the vertical contact. In figure 3.33, the phase angle shifts from 45 degree which is the value in a homogeneous half-space, climbs up to 51 degree and drops to 42.5 degree when crossing the interface. In the higher conductivity medium the phase decays more sharply.

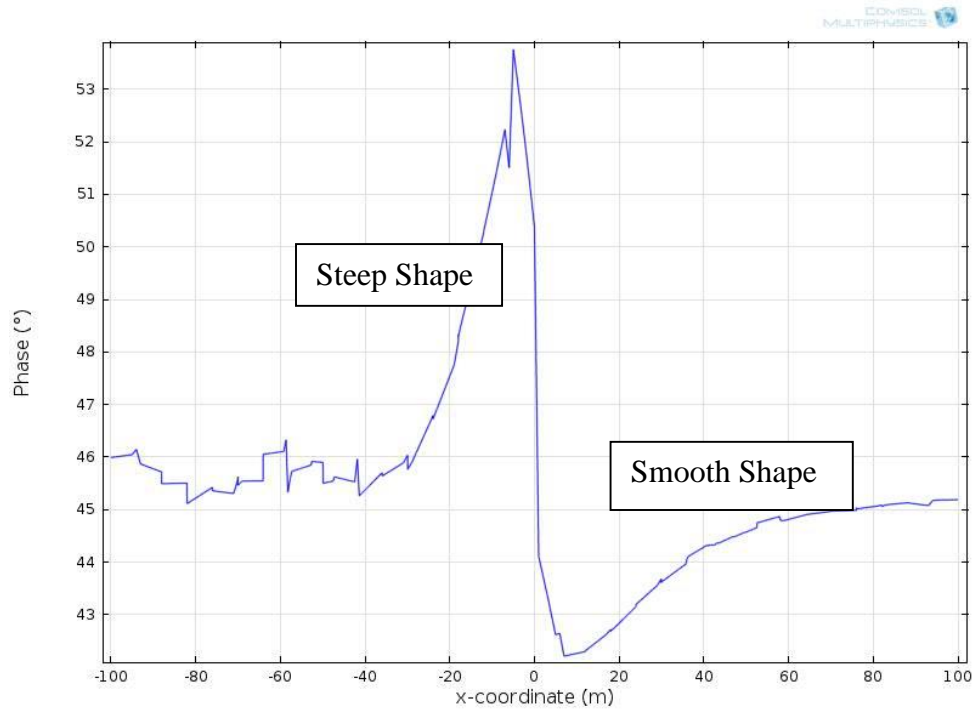


Figure 3.33 Phase plot of H-polarization at $Z=0$ & $Y=0$ along the X axis.

The calculated conductivity (equation 2.32) is plotted in figure 3.34. As can be seen, at the boundary of the vertical contact, the calculated conductivity value spikes. When moving far away from the vertical contact, the calculated conductivity converges to the actual conductivities of the media.

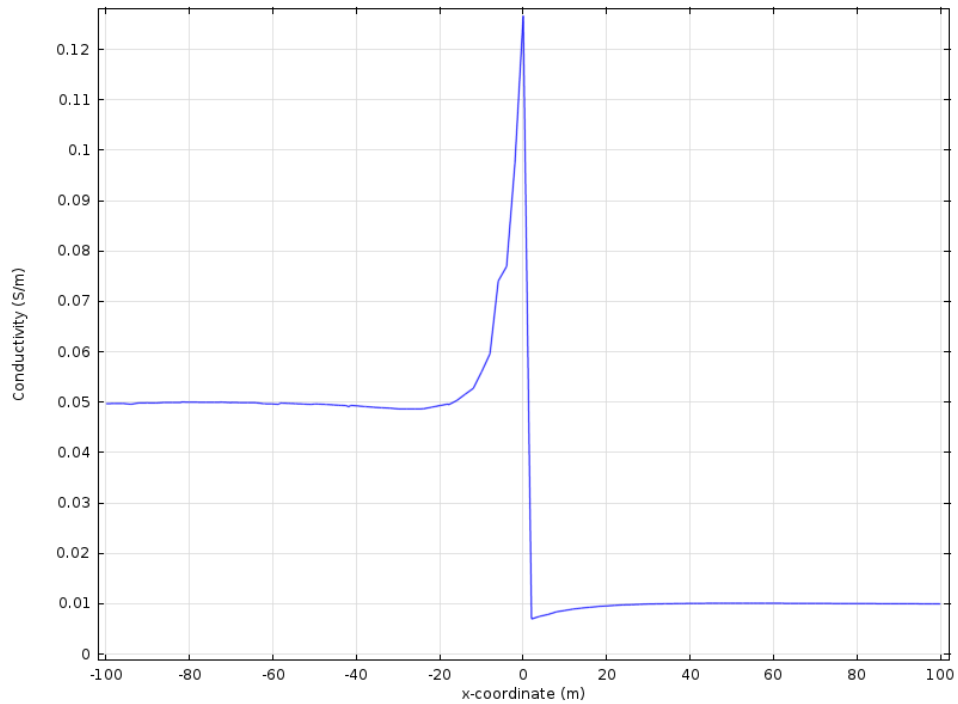


Figure 3.34 Calculated conductivity plot of H-polarization at $Z=0$ & $Y=0$ along the X axis.

The effect on the phase angle of different conductivity contrasts is studied. In the model, most of the parameters are kept the same including the conductivity of the left medium which is 0.05 S/m. The other medium electrical conductivity is varied with values of 0.01 S/m, 0.005 S/m, 0.0025 S/m and 0.00125 S/m. The ratios of electrical conductivity $\frac{\sigma_1}{\sigma_2}$ are 5, 10, 20 and 40. As illustrated in figure 3.35, when the electrical conductivity of medium 2 ($X>0$) decreases, the phase shift differences between maximum and minimum value increase. When the contrast ratio is increased, the graphs become much steeper on the conductive side and smoother on the resistive side. As can be seen in the plots, even though the electrical conductivity of medium 1 ($X<0$) stays the same, the phase reading varies in value. This indicates that the phase angle is a function of the contrast, not the actual conductivities of the media.

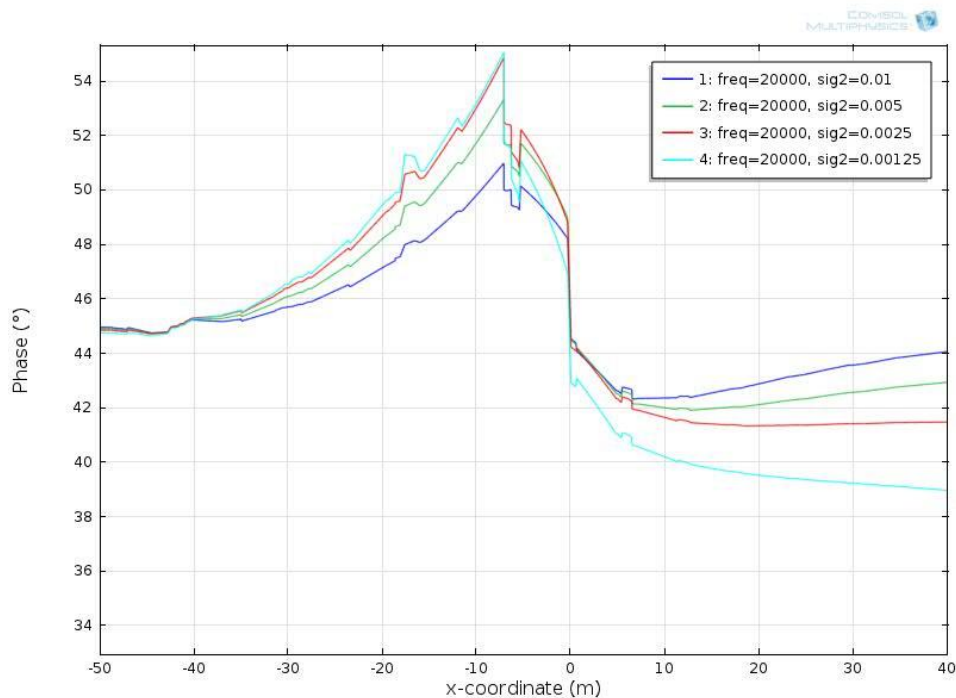


Figure 3.35 Phase plot with varying conductivity of medium 2 of H-polarization at $Z=0$ & $Y=0$ along the X axis.

3.3.2 VERTICAL CONTACT: E-POLARIZATION

In the E-polarization case, the plane wave propagates with horizontal electric field parallel to the strike of the vertical contact as shown in figure 3.36. The model is modified from H-polarization modeling by rotating the vertical contact by 90 degrees. The electric conductivities of the ground are 0.05 S/m ($Y < 0$) and 0.01 S/m ($Y > 0$). For the results shown in figure 3.37, the arrows represent the magnetic field and the slice indicates the horizontal magnetic field which ranges from 2.1667 A/m to -0.1699 A/m.

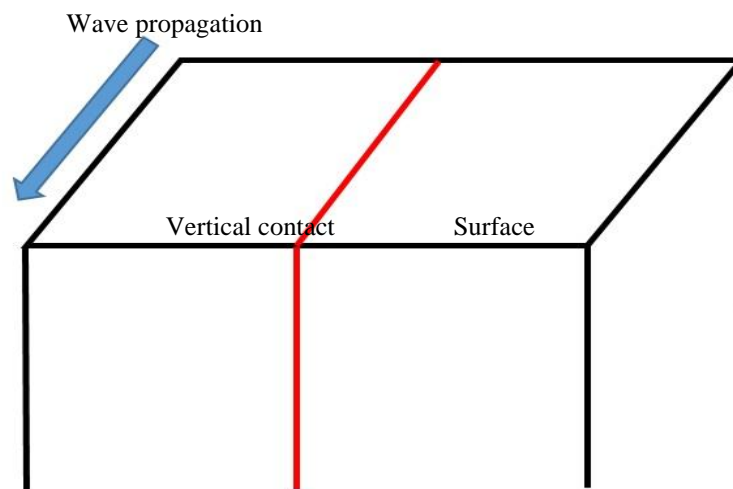


Figure 3.36 3D view of E-polarization. The blue arrow indicates the wave propagation direction in the air, and red line indicates the strike of the vertical contact.

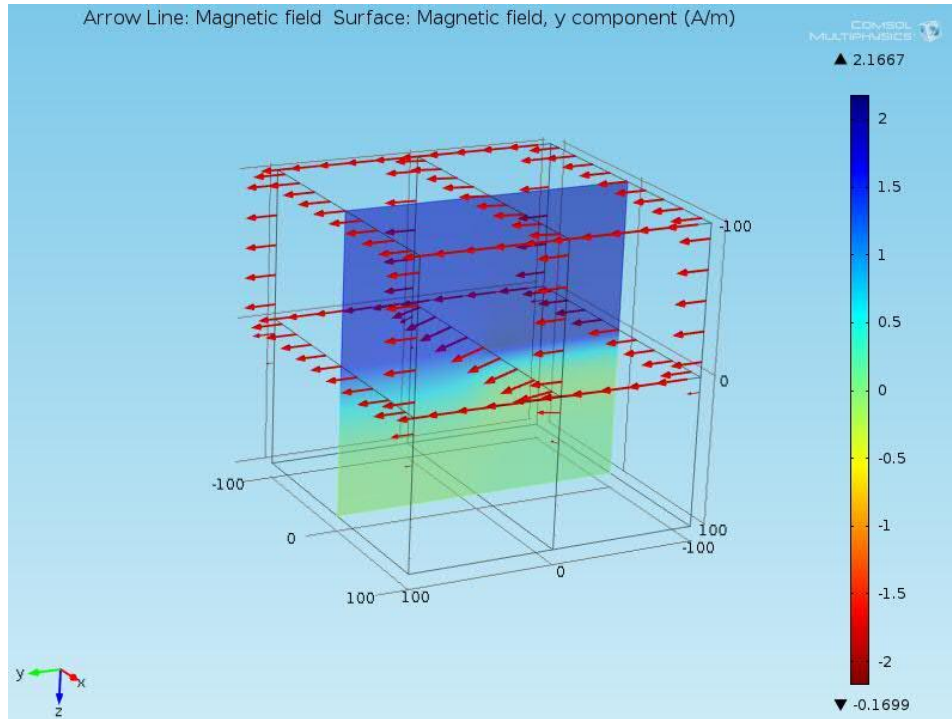


Figure 3.37 3D simulation results of E-polarization. The arrows represent the magnetic field and the slice indicates the horizontal magnetic field

In the case of E polarization, the horizontal electric field is parallel to the contact so there are no induced charges accumulating on the interface. On the other hand, the horizontal magnetic field continuously varies when crossing the contact. At a far distance away from the contact, the contact between air and ground can be considered as a homogeneous half-space and there is a constant value of horizontal magnetic field in the air. When approaching the vertical contact, the magnetic field is tilted and causes significant changes of the magnetic field in the Y and Z directions.

Figure 3.38 shows the horizontal magnetic field plotted along the Z axis in different materials. The blue & green lines represent the real and quadrature components in resistive material (0.01 S/m), while red & cyan colors represent the real and quadrature components in conductive material (0.05 S/m). Although both sets of profiles are located near the vertical contact, the values of the real and quadrature components at the interface between the air and ground ($Z=0$) are not equal. As illustrated, regarding skin depth, the real and quadrature components of the horizontal magnetic field in the conductive medium ($Y<0$) are decaying to zero faster than those in the resistive medium.

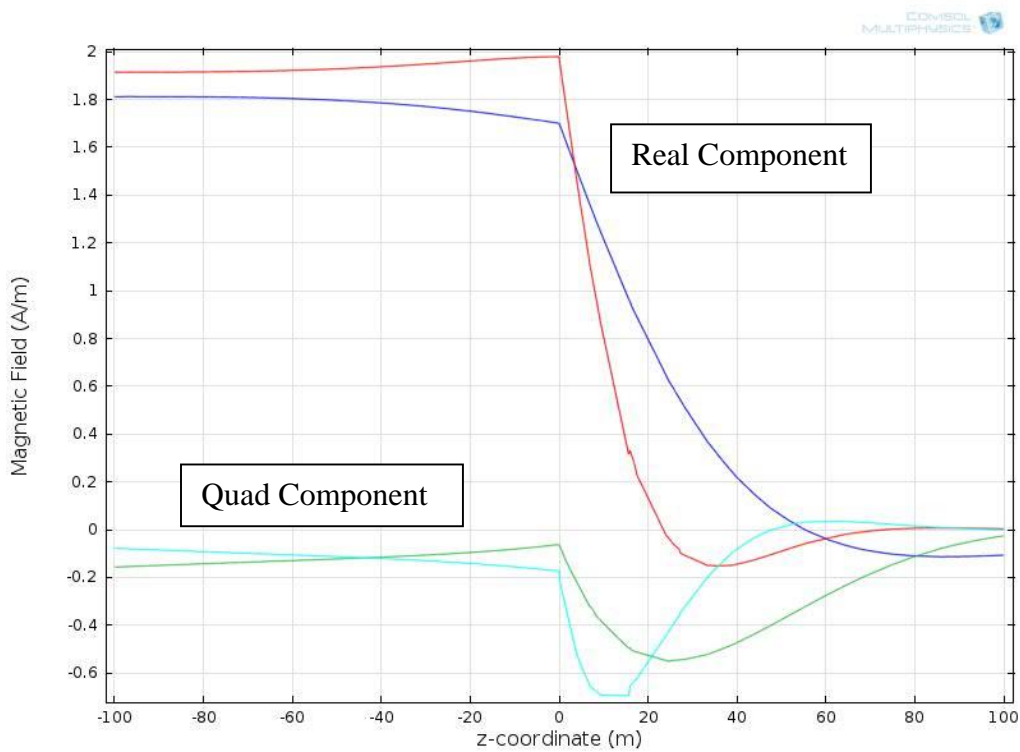


Figure 3.38 Horizontal magnetic field component plots of E-polarization plotted along Z axis at $X=0$, $Y= -50$ (conductive medium) and $X=0$, $Y=50$ (resistive medium)

Figures 3.39 and 3.40 are plots of the Y and Z components of magnetic field along the Y axis on the surface. In both figures, at a large distance on either side of the contact, the values are their half-space values. In figure 3.39, near the contact, an enhancement can be observed on the conductive side and a reduction on the resistive side. On the resistive side, the horizontal magnetic field is decreasing more slowly. In figure 3.40, the vertical magnetic field peaks right at the vertical contact and decays on both side. It falls slowly on the resistive side ($Y>0$) in accord with skin depth arguments. The quadrature component decreases from zero far from the contact and reaches minima on both sides of the contact and then increases to approximately zero at the vertical contact. It changes more rapidly in the more conductive medium ($Y<0$).

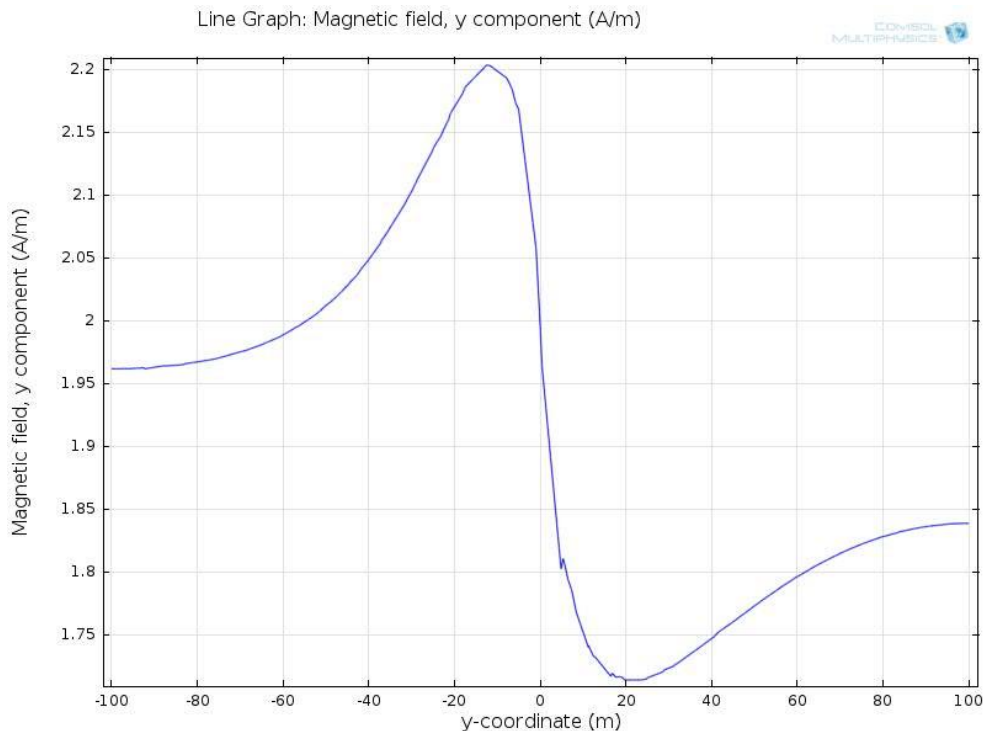


Figure 3.39 Horizontal magnetic field component at $X=0$ & $Z=0$ along the Y axis of E-polarization

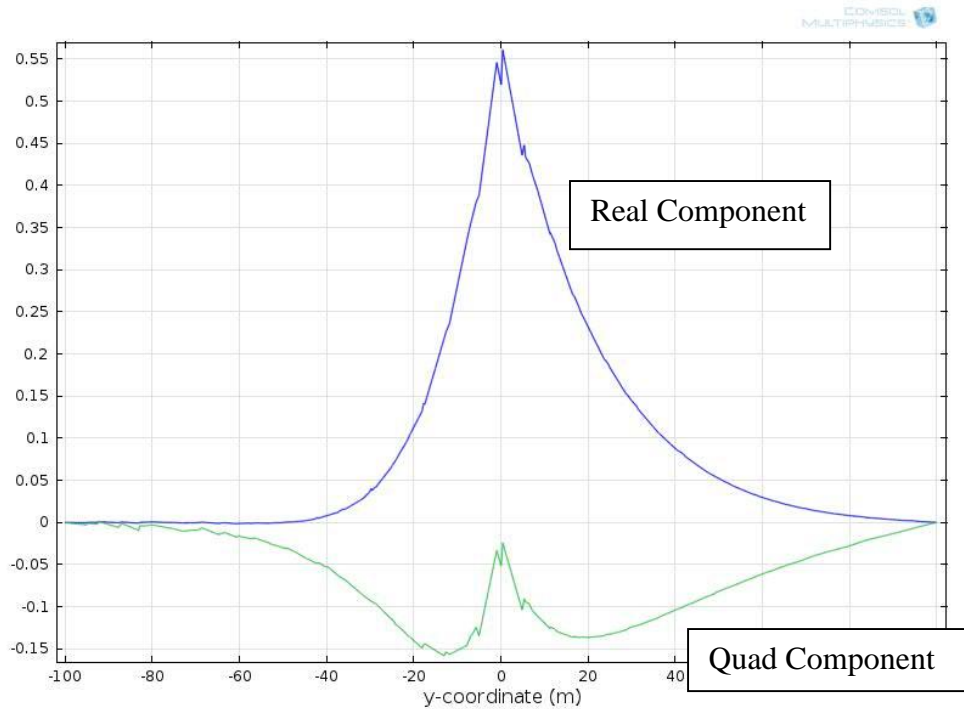


Figure 3.40 Vertical magnetic field component at $X=0$ & $Z=0$ along the Y axis of E-polarization.

The majority of VLF measurements are made of only the magnetic field and the case of E-polarization is more important than H-polarization because it can be detected from the magnetic field measurement. Figures 3.41, 3.42 and 3.43 are plots of inphase/Quad, Tilt and Phase of simulation results along the Y axis direction on the surface. Even though both vertical and horizontal components of magnetic field are changing, the inphase & Quad have a similar shape to the vertical magnetic field plot. This indicates that the change in the vertical magnetic field is dominant compared to horizontal components. The Tilt is calculated as the arctan of inphase, therefore tilt is essentially the same shape as the inphase plot. In figure 3.43, a reduction of the phase angle on the conductive side

and an enhancement on the resistive side can be observed. This is the opposite of what is seen for the horizontal magnetic field.

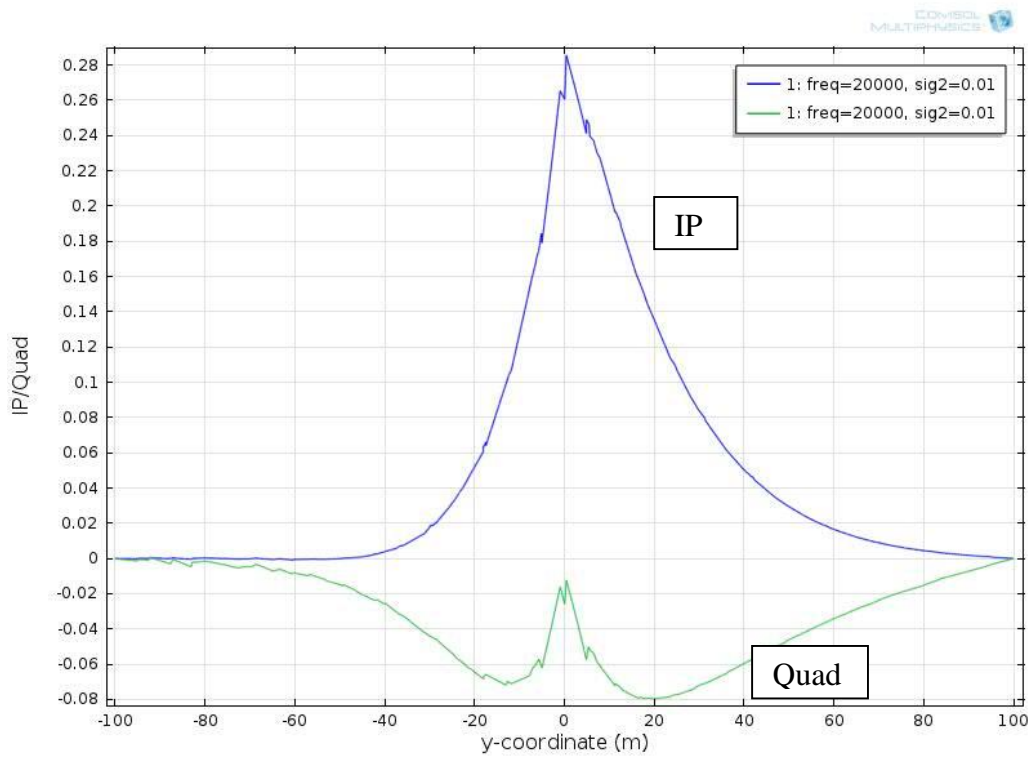


Figure 3.41 Inphase & Quad plots at X=0 & Z=0 along the Y axis of E-polarization.

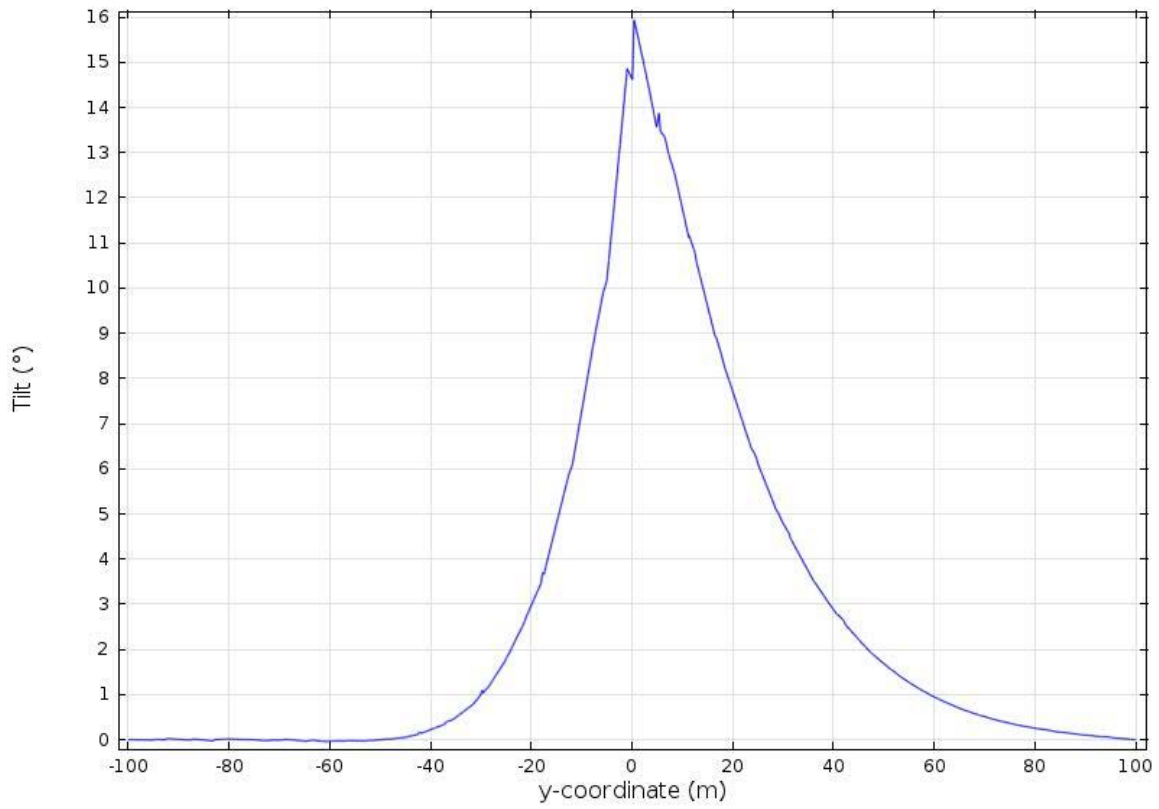


Figure 3.42 Tilt plot at $X=0$ & $Z=0$ along the Y axis of E-polarization

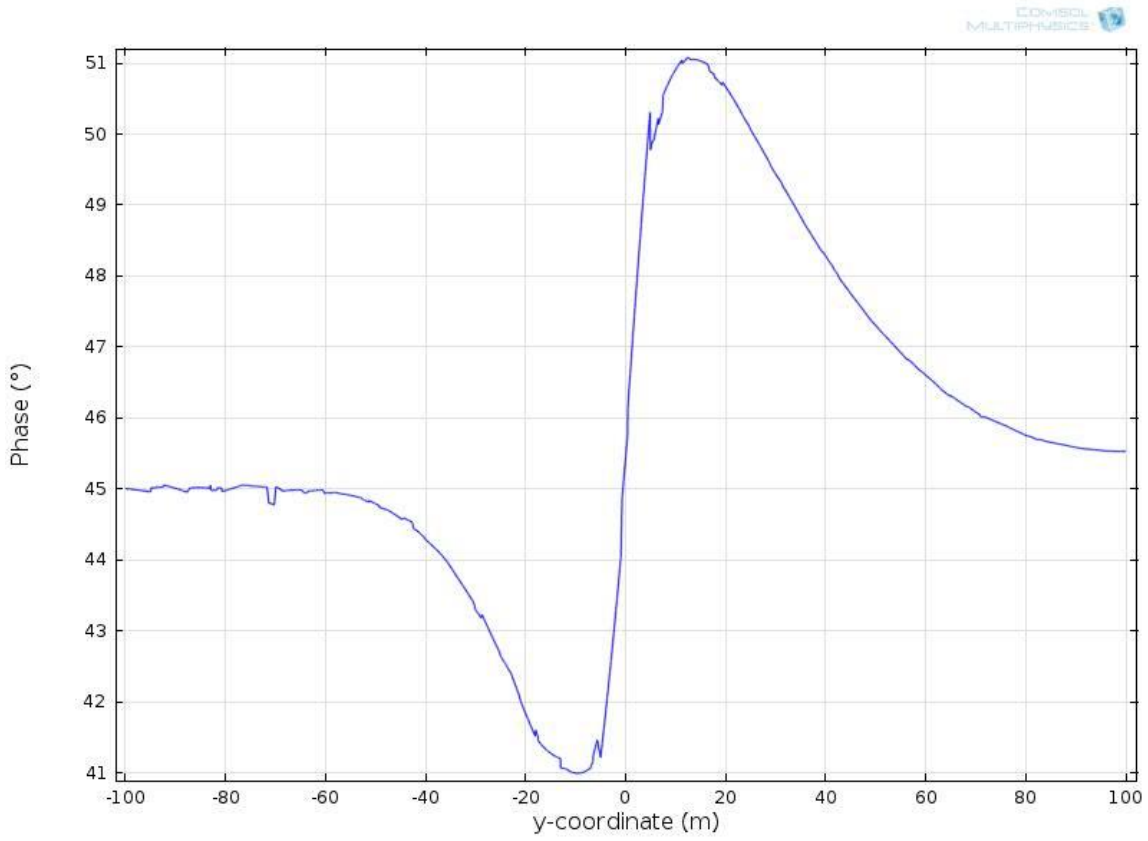


Figure 3.43 Phase plot at $X=0$ & $Z=0$ along Y axis of E-polarization.

The calculated conductivity is plotted in figure 3.44. Values of 0.05 S/m and 0.01 S/m can be seen when far away from the vertical contact, and the results match the input values. Unlike the case of H-polarization, at the vertical contact, the calculated conductivity is the average value of media 1 and 2.

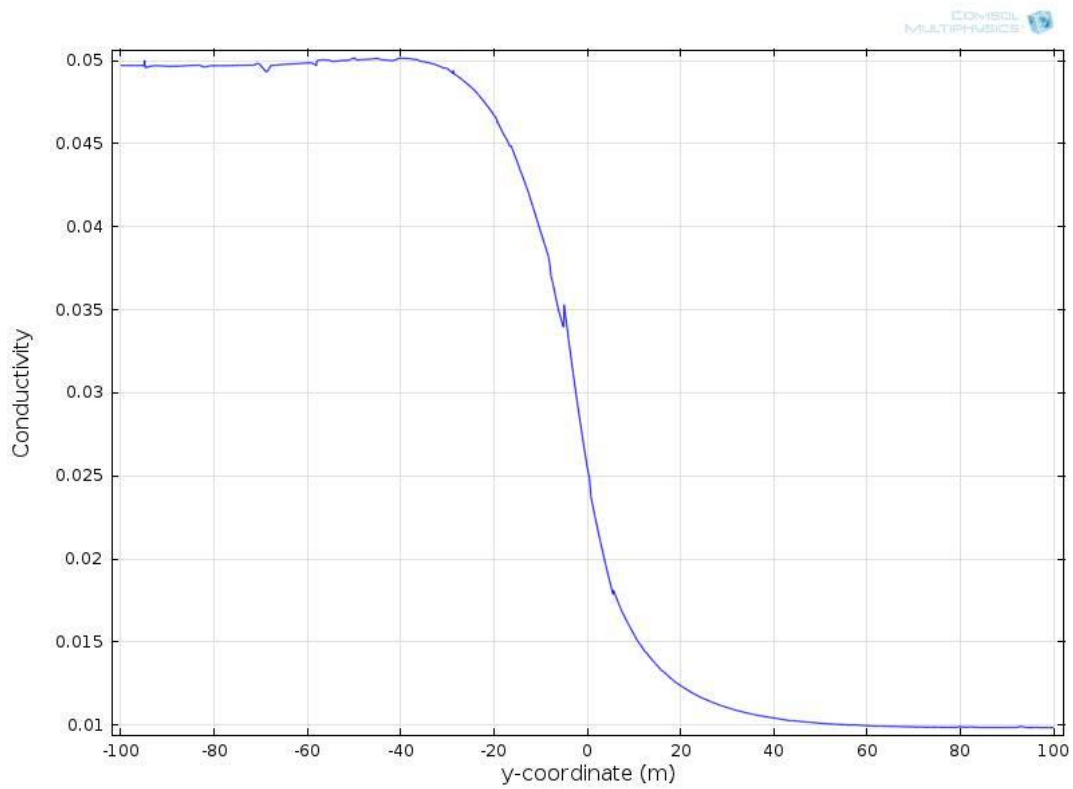


Figure 3.44 Calculate conductivity plot at X=0 & Z=0 along Y axis of E-polarization.

The effects of different conductivity contrasts are studied. In the model, most of the parameters are kept the same including the conductivity of the conductive medium ($Y < 0$) which is 0.05 S/m. The other medium ($Y > 0$) electric conductivity is given values 0.01 S/m, 0.005 S/m, 0.0025 S/m and 0.00125 S/m.

Figure 3.45 displays inphase & Quad plots for different conductivity contrasts. As the resistive side ($Y > 0$) becomes more resistive, the inphase and Quad peak values increase.

For ratios of $\frac{\sigma_1}{\sigma_2}$ over 10, the Quad changes from negative to positive at the vertical contact. As can be seen in figure 3.46, the tilt has a very similar shape to the inphase curves in figure 3.45.

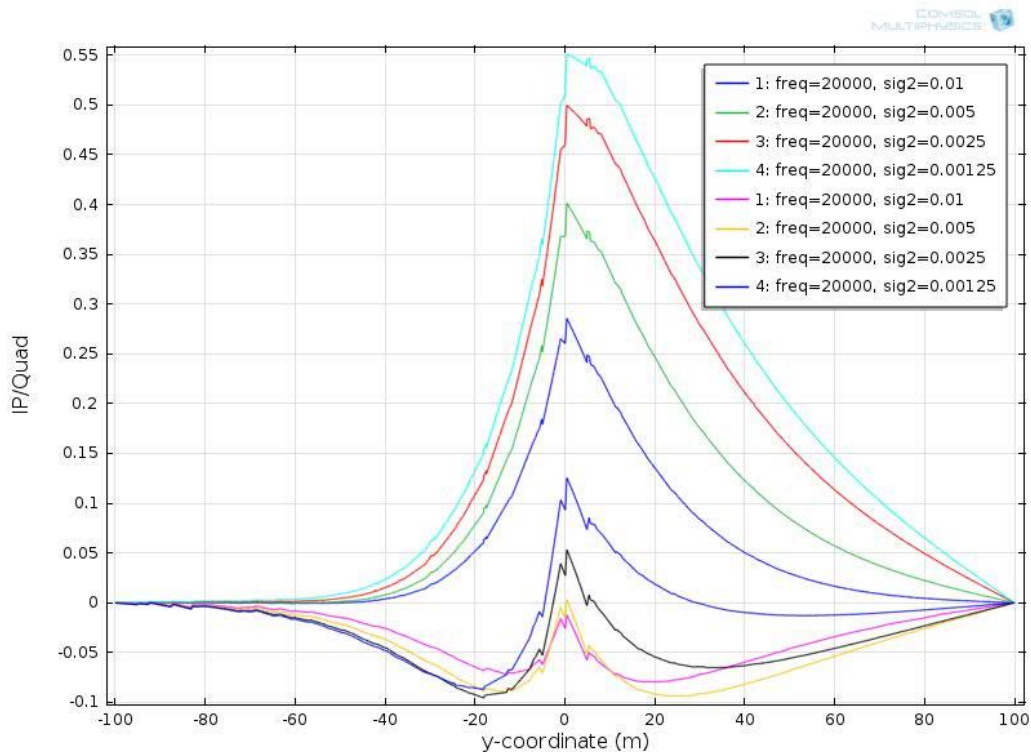


Figure 3.45 inphase & Quad plots with varying conductivity of medium 2 of E-polarization at $X=0$ & $Z=0$ along the Y axis.

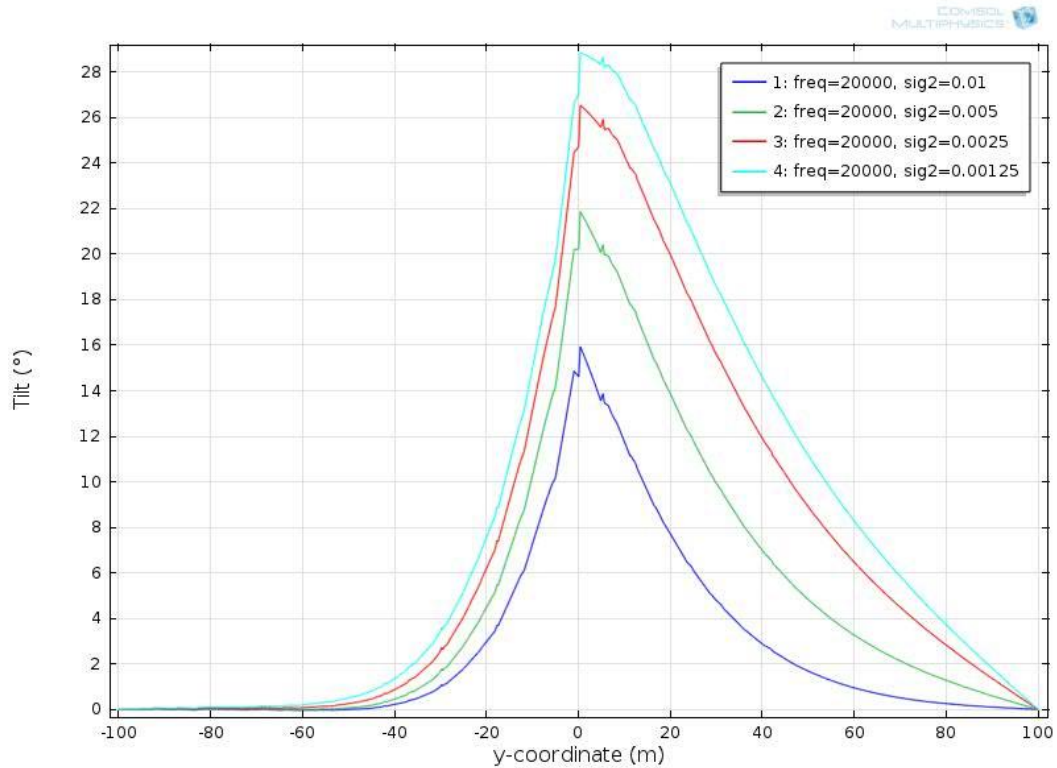


Figure 3.46 Tilt plots with varying conductivity of medium 2 of E-polarization at $X=0$ & $Z=0$ along the Y axis.

Figures 3.47 and 3.48 display phase and calculated conductivity plots for different conductivity contrasts. Like the case of H-polarization, as illustrated in figure 3.47, when the electrical conductivity of medium 2 ($Y>0$) decreases, the phase shift differences between maximum and minimum value increase. As also can be seen in the plots, even though the electrical conductivity of medium 1 ($Y<0$) stays the same, the phase reading varies in value. This indicates that the phase angle is a function of the contrast, not the actual conductivities of the media. In figure 3.48, we can see that the actual values of conductivities are recovered at large distances from the contact.

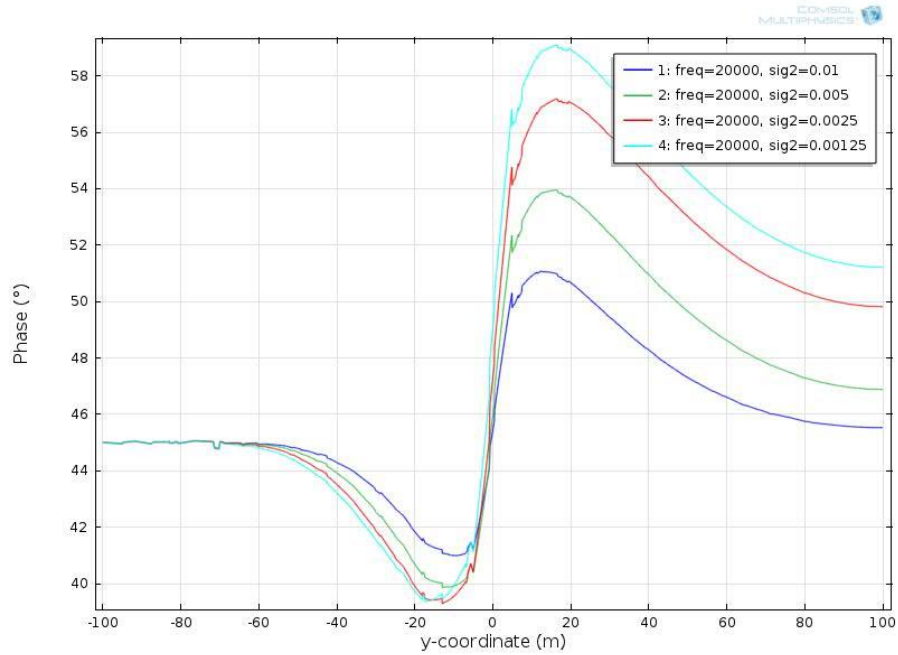


Figure 3.47 Phase plots with varying conductivity of medium 2 of E-polarization at $X=0$ & $Z=0$ along the Y axis.

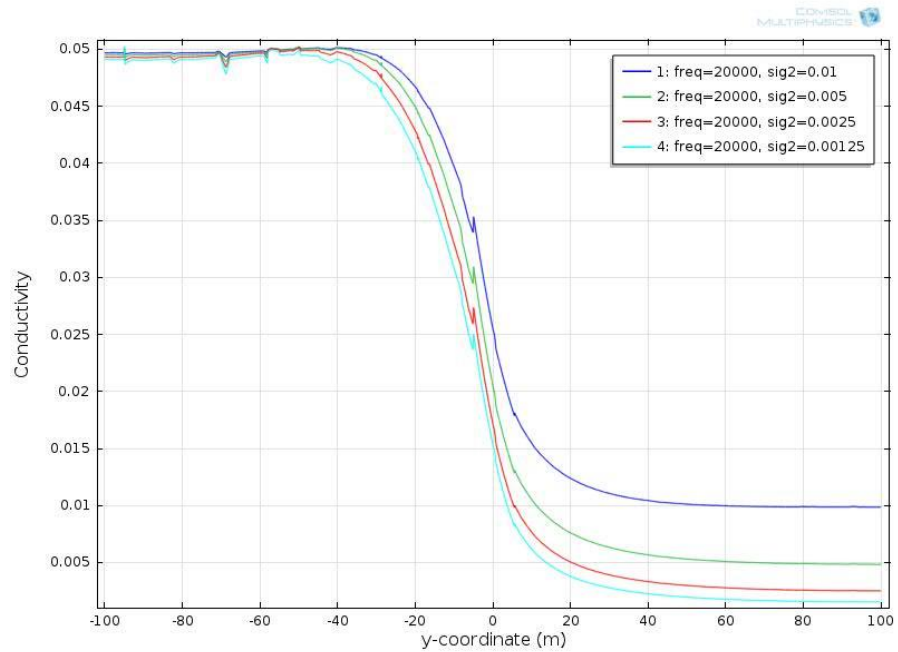


Figure 3.48 Calculated Conductivity plots with varying conductivity of medium 2 of E-polarization at $X=0$ & $Z=0$ along the Y axis.

3.3.3 VERTICAL CONTACT: COMBINATION OF E-POLARIZATION & H-POLARIZATION

As previously mentioned, it is easy to distinguish the advantages and disadvantages of E-polarization and H-polarization. In E-polarization or TE mode, the location of a vertical contact can be observed as the peak of inphase, Quad or Tilt plots. Which side is more resistive or conductive can also be observed by checking the rate of decay. By comparing with simulation results, the conductivity contrast ratio of a vertical contact in the ground can be estimated. On the other hand, in H-polarization or TM mode, the vertical contact underground can only be observed from a plot of the phase or resistivity measurement when surveying. However, due to their similar shapes, it is difficult to distinguish between E and H-polarization from a phase plot. In general, more information can be inferred from E-polarization than H-polarization contacts.

In reality when doing a field VLF survey, the orientations of underground structure such as vertical contact or non-vertical contact are unknown, and we cannot control the direction of wave propagation. It is impossible to determine whether the measurements are E-polarization or H-polarization. Most cases are a linear combination of H-polarization and E-polarization and the E-polarization can be considered a maximum response and H-polarization as a minimum response in the magnetic field. In the field, usually several transmitters are picked as sources rather than one transmitter station. The purpose is to record electromagnetic waves from different orientations, so that significant E-polarization is recorded.

CHAPTER 4
TOPOGRAPHY AND LAKE
MODELS AND ANALYSIS

4.1 TOPOGRAPHY MODELING - HILL

In VLF-EM prospecting, one of the factors influencing measured data is the effect of topography in the survey areas. Uneven terrain contributes significant anomalies which cause the observed VLF data to depart from the pattern which would be expected on flat ground (Abdul-Malik et al., 1985). In this section, the VLF plane wave response of a hill is discussed in detail.

Section 3.3 represents the VLF response at a vertical resistivity contrast, and the case of uneven topography can be considered as a special case of a vertical contact. In this case, there are resistivity contrasts between air and hill material. Referring to the theory, the VLF wave components in air are constant and the air has infinite resistivity. In the ground, the resistivity value is much smaller than that in the air and the VLF wave components decay with depth.

We model a cubic domain of dimensions 200m (width) * 200m (depth) * 150m (height). 20 kHz frequency is used for the plane wave when modeling and the angle of incidence is $\pi/2 - \pi/40$. The ground resistivity is constant at 100 ohm*m which gives a skin depth of 35.58m. A Gaussian function is used to represent the hill.

$$hill = -hillheight \times \exp\left(-\frac{(x \sin \theta + y \cos \theta)^2}{hillwidth^2}\right) \quad \text{Equation 4.1}$$

θ is the angle between the strike of the hill and the X axis. The hill has a negative value due to the basic modeling set-up that the elevation in the air has negative values. *hillheight* indicates the elevation differences, and *hillwidth* is the standard deviation of the hill function.

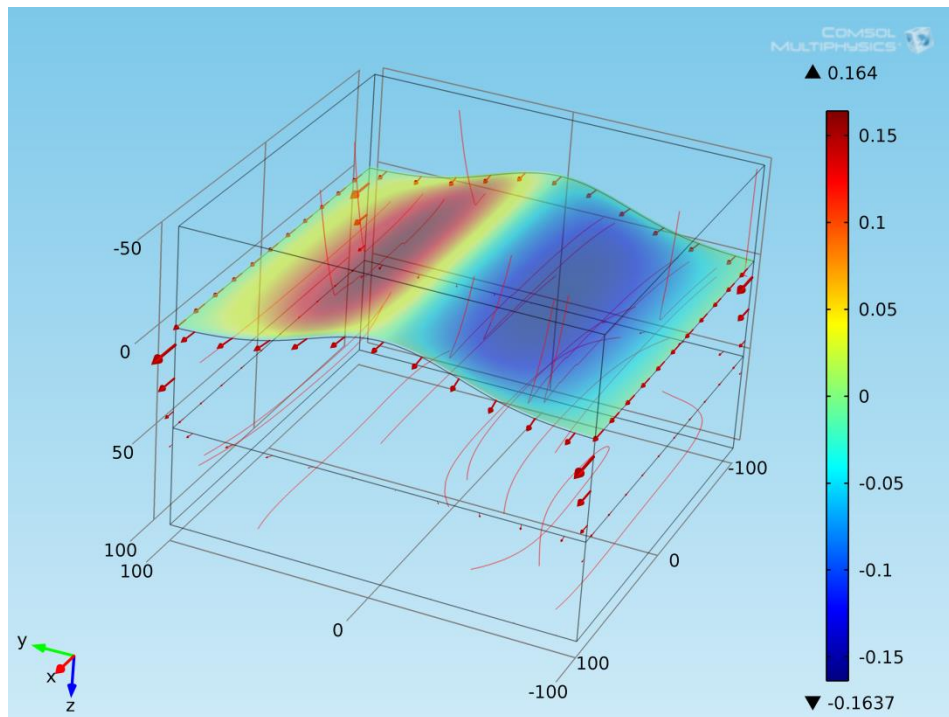


Figure 4.1 3D view of topography modeling results. The streamlines describe orientation of the electric field in the air and in the ground. The arrows represent the current flowing in the ground. The slice plot represents inphase plot on the surface.

As shown in figure 4.1, for this simulation, the elevation of the hill varies only in the Y direction ($\theta = 0^\circ$). The hill in the model uses a parameterized surface that separates the ground from the air domains. In the model, a few new parameters are added to indicate the orientation of the hill and the incoming waves. The angle α is the angle between the incoming electromagnetic wave and the X axis. The angle β is the angle between the line walked by an imaginary person with a VLF receiver and the X axis. In this model, the

angle α is set at 0° . The streamlines in figure 4.1 are showing the orientation of the electric field in the air and in the ground. The arrows represent the current flowing in the ground. In this case, the electromagnetic wave is parallel to the X axis and the strike of the hill. The main component of the horizontal magnetic field in the air crossing the hill body is tilted due to the uneven surface contact, causing maximum inphase and Quad responses.

Besides the additions of various angles, the model is modified by including a non-flat interface between the air and ground. Therefore, the magnetic field equations are modified. The Z in the original equations 2.15 and 2.16 is changed to $(z - hill)$ where $(z - hill) > 0$ is the ground component and $(z - hill) < 0$ is the air component. The X in equations 2.15 and 2.16 refers to the direction of the wave propagation and is replaced by $x \times \cos \alpha + y \times \sin \alpha$. The magnetic field imposed on the outer boundaries of the numerical model become,

in air

$$\begin{bmatrix} H_x \\ H_y \\ H_z \end{bmatrix} = \begin{bmatrix} - (a_0 e^{-u_0(z-hill)} + b_0 e^{u_0(z-hill)}) e^{-i\lambda(x \cos \alpha + y \sin \alpha)} \times \sin \alpha \\ (a_0 e^{-u_0(z-hill)} + b_0 e^{u_0(z-hill)}) e^{-i\lambda(x \cos \alpha + y \sin \alpha)} \times \cos \alpha \\ 0 \end{bmatrix}, \quad \text{Equation 4.2}$$

in ground

$$\begin{bmatrix} H_x \\ H_y \\ H_z \end{bmatrix} = \begin{bmatrix} - a_1 e^{-u_1(z-hill)} e^{-i\lambda(x \cos \alpha + y \sin \alpha)} \times \sin \alpha \\ a_1 e^{-u_1(z-hill)} e^{-i\lambda(x \cos \alpha + y \sin \alpha)} \times \cos \alpha \\ 0 \end{bmatrix}. \quad \text{Equation 4.3}$$

Also, since the analytical solution for the magnetic field is derived with the assumption of flat ground, the boundary conditions are only approximately correct.

Different geometry parameters are used to characterize the topographic effect on measured VLF data. In tables 4.1 to 4.7, hillheight is given values 10m, 20m 30m and 40m, and hillwidth is given values 20m, 30m, 40m and 50m. Different ground resistivity values are also involved in the analysis. For each simulation, the skin depth of the ground material, max slope, max inphase, and max Quad are recorded.

Hillheight	10					
Hillwidth	50					
Resistivity	Skin Depth	SkinD/Width	SkinD/Height	max(slope)	max Ip	max Quad
100	35.5881	0.7118	3.5588	0.1715	0.0797	0.0381
200	50.3292	1.0066	5.0329	0.1715	0.0586	0.0331
500	79.5775	1.5915	7.9577	0.1715	0.037	0.0233
800	100.6584	2.0132	10.0658	0.1715	0.0292	0.0182
1000	112.5395	2.2508	11.2540	0.1715	0.0262	0.016

Table 4.1 Data analysis of hill model at height 10m and width 50m

Hillheight	20					
Hillwidth	50					
Resistivity	Skin Depth	SkinD/Width	SkinD/Height	max(slope)	max Ip	max Quad
100	35.5881	0.7118	1.7794	0.3431	0.1628	0.0756
200	50.3292	1.0066	2.5165	0.3431	0.1191	0.0663
500	79.5775	1.5915	3.9789	0.3431	0.0747	0.0485
800	100.6584	2.0132	5.0329	0.3431	0.059	0.0363
1000	112.5395	2.2508	5.6270	0.3431	0.0529	0.0319

Table 4.2 Data analysis of hill model at height 20m and width 50m

Hillheight	30					
Hillwidth	50					
Resistivity	Skin Depth	SkinD/Width	SkinD/Height	max(slope)	max Ip	max Quad
100	35.5881	0.7118	1.1863	0.5146	0.251	0.1124
200	50.3292	1.0066	1.6776	0.5146	0.1825	0.0997
500	79.5775	1.5915	2.6526	0.5146	0.1137	0.0704
800	100.6584	2.0132	3.3553	0.5146	0.0896	0.0549
1000	112.5395	2.2508	3.7513	0.5146	0.0802	0.0482

Table 4.3 Data analysis of hill model at height 30m and width 50m

Hillheight	40					
Hillwidth	50					
Resistivity	Skin Depth	SkinD/Width	SkinD/Height	max(slope)	max Ip	max Quad
100	35.5881	0.7118	0.8897	0.6862	0.3496	0.1505
200	50.3292	1.0066	1.2582	0.6862	0.2527	0.1354
500	79.5775	1.5915	1.9894	0.6862	0.1558	0.0953
800	100.6584	2.0132	2.5165	0.6862	0.1222	0.0743
1000	112.5395	2.2508	2.8135	0.6862	0.1093	0.0653

Table 4.4 Data analysis of hill model at height 40m and width 50m

Hillheight	20					
Hillwidth	40					
Resistivity	Skin Depth	SkinD/Width	SkinD/Height	max(slope)	max Ip	max Quad
100	35.5881	0.8897	1.7794	0.4288	0.1753	0.0888
200	50.3292	1.2582	2.5165	0.4288	0.1267	0.075
500	79.5775	1.9894	3.9789	0.4288	0.0793	0.0509
800	100.6584	2.5165	5.0329	0.4288	0.0627	0.0394
1000	112.5395	2.8135	5.6270	0.4288	0.0562	0.0346

Table 4.5 Data analysis of hill model at height 20m and width 40m

Hillheight	20					
Hillwidth	30					
Resistivity	Skin Depth	SkinD/Width	SkinD/Height	max(slope)	max Ip	max Quad
100	35.5881	1.1863	1.7794	0.5716	0.1835	0.1044
200	50.3292	1.6776	2.5165	0.5716	0.1306	0.0834
500	79.5775	2.6526	3.9789	0.5716	0.0817	0.0545
800	100.6584	3.3553	5.0329	0.5716	0.0647	0.0417
1000	112.5395	3.7513	5.6270	0.5716	0.0581	0.0365

Table 4.6 Data analysis of hill model at height 20m and width 30m

Hillheight	20					
Hillwidth	20					
Resistivity	Skin Depth	SkinD/Width	SkinD/Height	max(slope)	max Ip	max Quad
100	35.5881	1.7794	1.7794	0.857	0.1814	0.1213
200	50.3292	2.5165	2.5165	0.857	0.1268	0.0905
500	79.5775	3.9789	3.9789	0.857	0.0798	0.0564
800	100.6584	5.0329	5.0329	0.857	0.0636	0.0426
1000	112.5395	5.6270	5.6270	0.857	0.0572	0.0371

Table 4.7 Data analysis of hill model at height 20m and width 20m

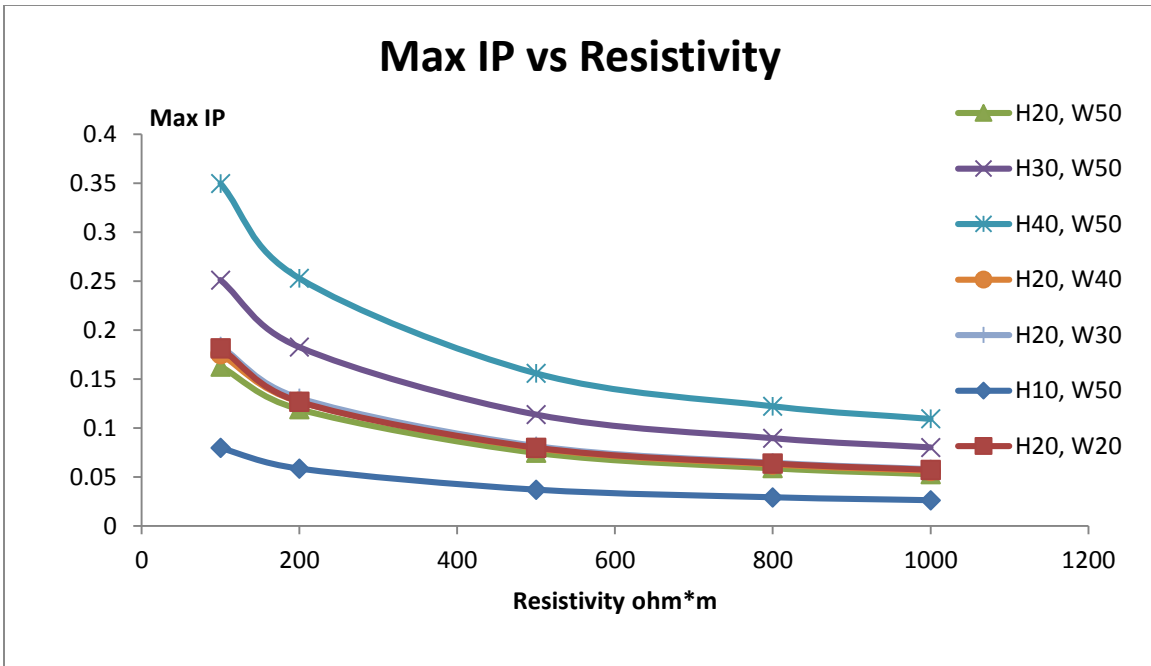


Figure 4.2 Max inphase vs Ground Resistivity of hill model

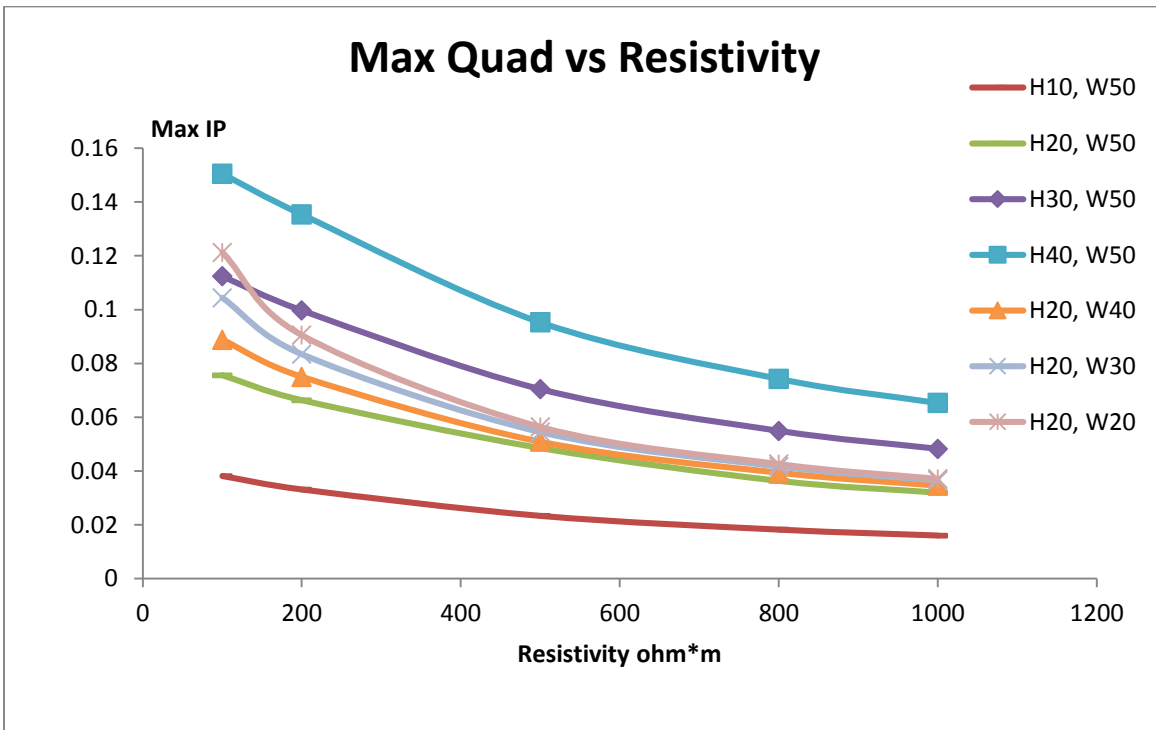


Figure 4.3 Max Quad vs Ground Resistivity of hill model

Figures 4.2 and 4.3 show Max inphase and Quad vs different ground resistivity values. The max inphase and Quad can be seen to be decreasing with increasing ground resistivity. This agrees with the prior discussion that the inphase and Quad decrease with decreasing resistivity contrast between the air and ground.

A trend that can be observed in these two figures is that the Max inphase and Quad graphs are shifted down when the height of the hill is decreased while the width of the hill stays the same. By checking the light blue, purple, green and blue graphs in figure 4.2, the graph has steeper slopes with bigger elevation changes. As expected, when the height of the hill becomes zero, which is a flat surface, the electromagnetic wave won't be tilted and there will be no inphase or Quad.

Another trend that can be observed in figures 4.2 and 4.3 is that the Max inphase and Quad are almost independent of the width of the hill. In figure 4.3, the pink, light blue, orange and green graphs represent Quad response at different width values. These simulations give very different values for small values of the resistivity but converge at around 4% for large values of resistivity. Similar trends can be observed in figure 4.2, and those four lines almost coincide for the same hill height.

From these two figures, we can determine that the height of the hill dominates the effects on VLF measurement data compared with the width of the hill. However, for all of the results shown, the hill width is similar to or less than the electromagnetic skin depth.

Figures 4.4 and 4.5 are plots of max inphase / max slope and max Quad / max slope versus skin depth / hill width. Trends that can be observed in these two figures are that the data collapse into two power law functions. A trend line function $y = 0.3531x^{-0.965}$ can be observed for figure 4.4, and $y = 0.1893x^{-0.783}$ can be observed for figure 4.5. For a given hill, when skin depth / hill width becomes greater, which may occur because the ground is becoming more resistive, smaller max inphase and Quad readings will be observed. These graphs can be used to predict max inphase and Quad readings when elevation data and the resistivity of the terrain is known.

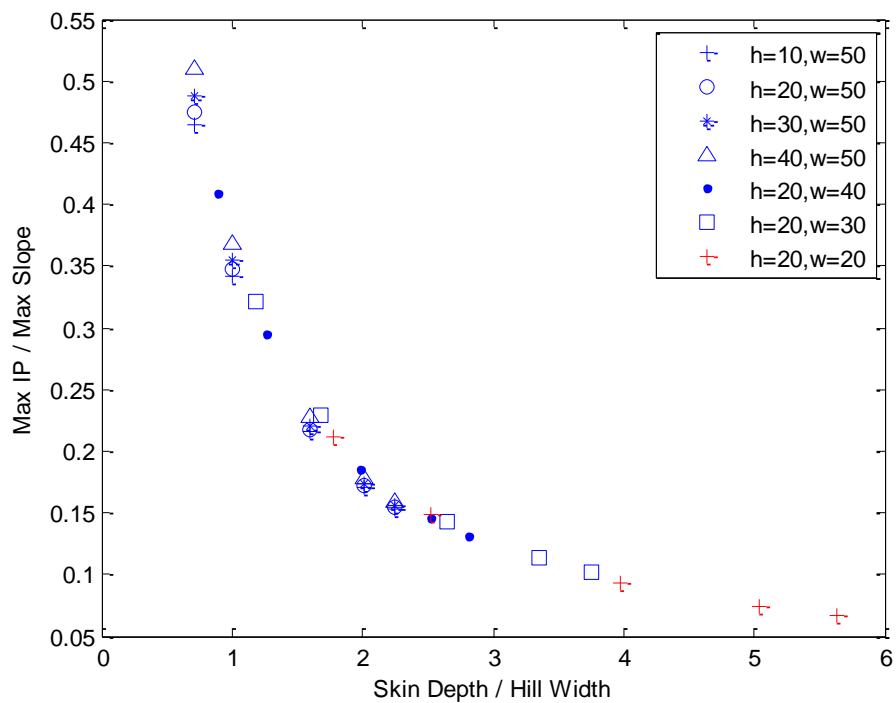


Figure 4.4 Max inphase/Max Slope vs Skin Depth/Hill Width

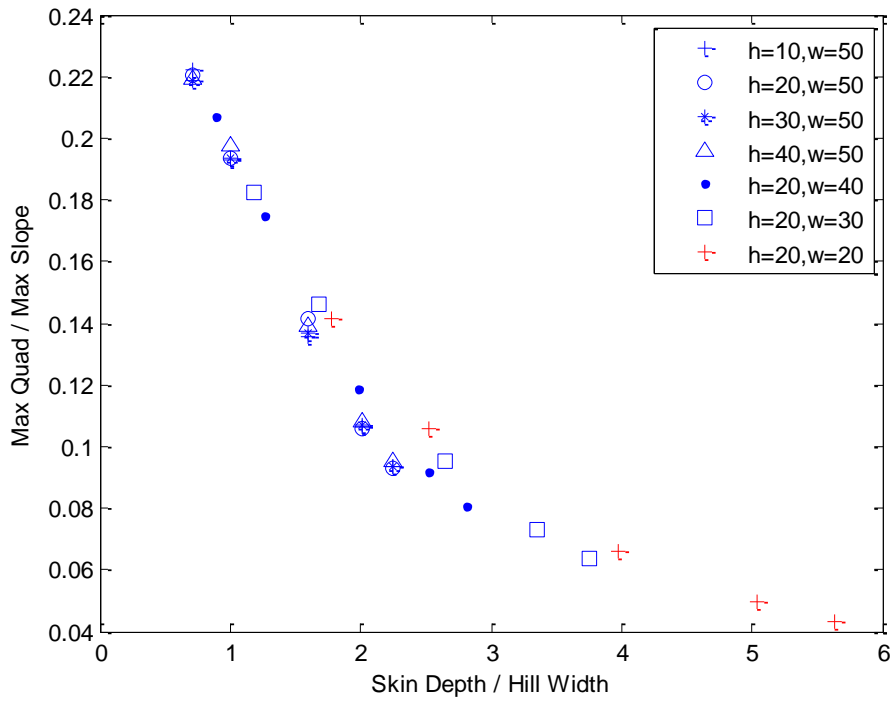


Figure 4.5 Max Quad/Max Slope vs Skin Depth/Hill Width

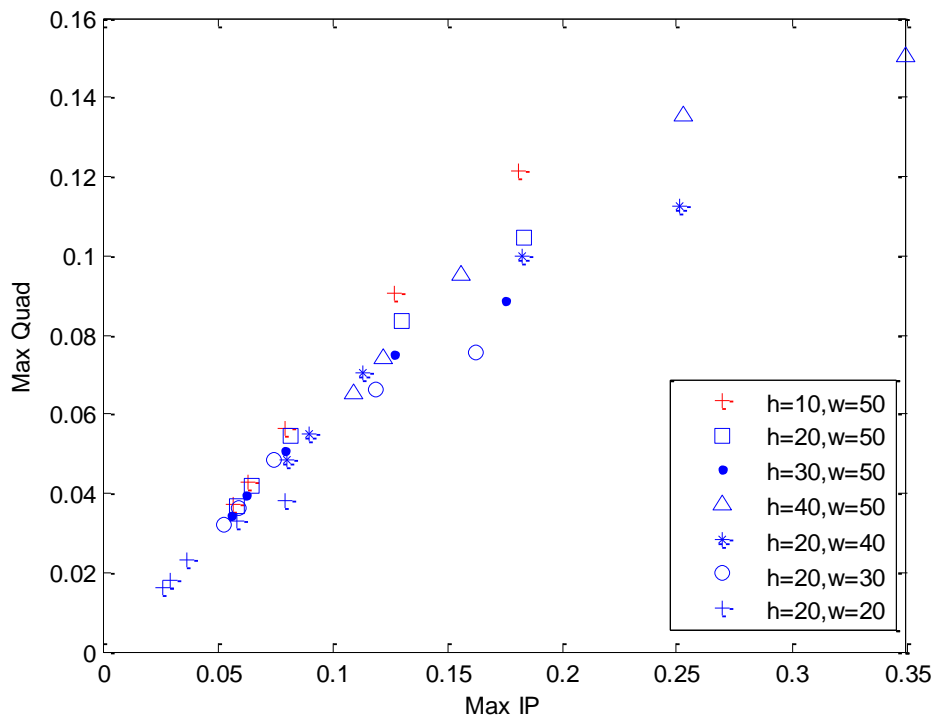


Figure 4.6 Max inphase vs Max Quad of hill modeling

The max inphase vs max Quad is plotted in figure 4.6. A trend function $y = 0.0997 \ln(x) + 0.291$ can be observed based on the plot. However, when Max inphase and Quad fall in a small range (less than 15% of Max reading), the relationship trends are roughly linear with a slope of approximate 0.5.

4.2 LAKE MODELING

In VLF-EM prospecting, another factor influencing measured data is the effect of water in the survey areas. Lake water has a resistivity contrast with the air and the surrounding soil, therefore causing a VLF response in the field survey. In this section, the VLF plane wave response of a lake is discussed in detail.

Section 4.1 represents the VLF response of a hill, and the case of a lake can be considered similarly. However, there are clearly differences between them. In the hill model, the major VLF response is caused by the contact between the air and the hill material. Referring to the model assumptions, the air has zero conductivity; therefore, the electromagnetic wave isn't decaying when travelling in air while it is decaying in hill material. In the lake model, the major VLF response is caused by the contact between the water and surrounding material with the electromagnetic wave decaying in both of them. This will cause a different VLF response.

The model domain consists of a rectangular prism of dimensions 200m (width) * 200m (depth) * 150m (height). 20k Hz frequency is used for the plane wave when modeling and the angle of incidence is $\pi/2 - \pi/40$. The ground resistivity is constant at 1000 ohm*m which gives a skin depth of 50.33m. The lake is 75m (width) * 75m (depth) * 20m (height) with 20 ohm*m resistivity.

Figure 4.7 shows the 3D simulation results of the lake model. The arrows describe the current flowing direction in the ground. The streamlines describe the electric field. The slice plot represents the inphase response.

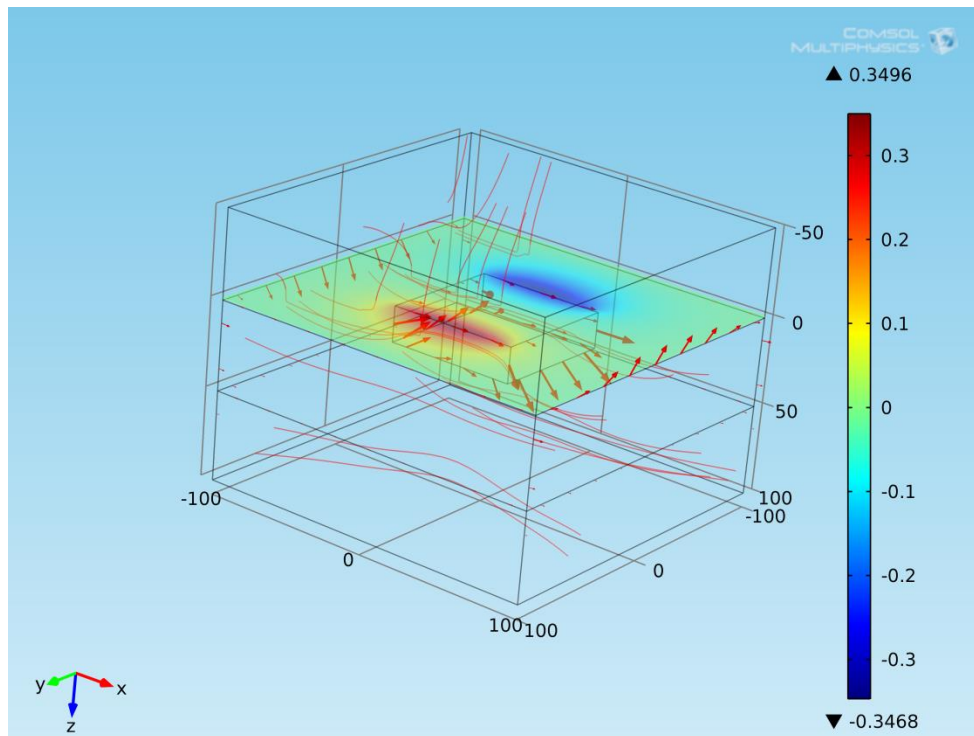


Figure 4.7 3D Results of inphase Response of Lake Model. The streamlines describe orientation of the electric field in the air and in the ground. The arrows represent the current flowing in the ground. The slice plot represents inphase plot on the surface.

Figure 4.8 is the horizontal magnetic field vertical profile through the horizontal center of the lake. There are two points at which the derivative changes discontinuously indicated with red circles in the plot which show the two contacts between air/water and water/soil. The field has a fairly constant value of 2 A/m in the air, and drops quickly in the water while decreasing much more slowly in the soil. In the model, the water is much more conductive than the ground material. The water is acting as a protective shield and is decreasing the signal penetration.

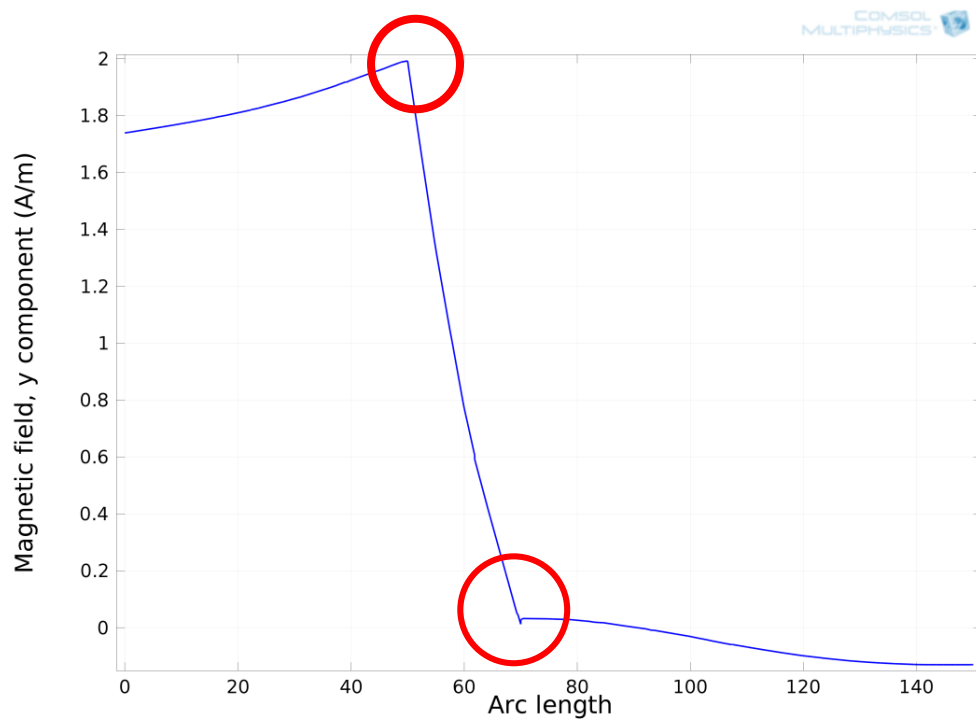


Figure 4.8 Horizontal Component of Magnetic Field in Lake Model at X=0 & Y=0 along the Z axis

Figures 4.9 and 4.10 show the inphase responses of the lake model. As seen, the current in the ground (arrows) bends in the direction of the magnetic field which is perpendicular to the direction of wave propagation. The inphase response reaches its maximum and minimum values on the edge of the lake along the direction of the magnetic field.

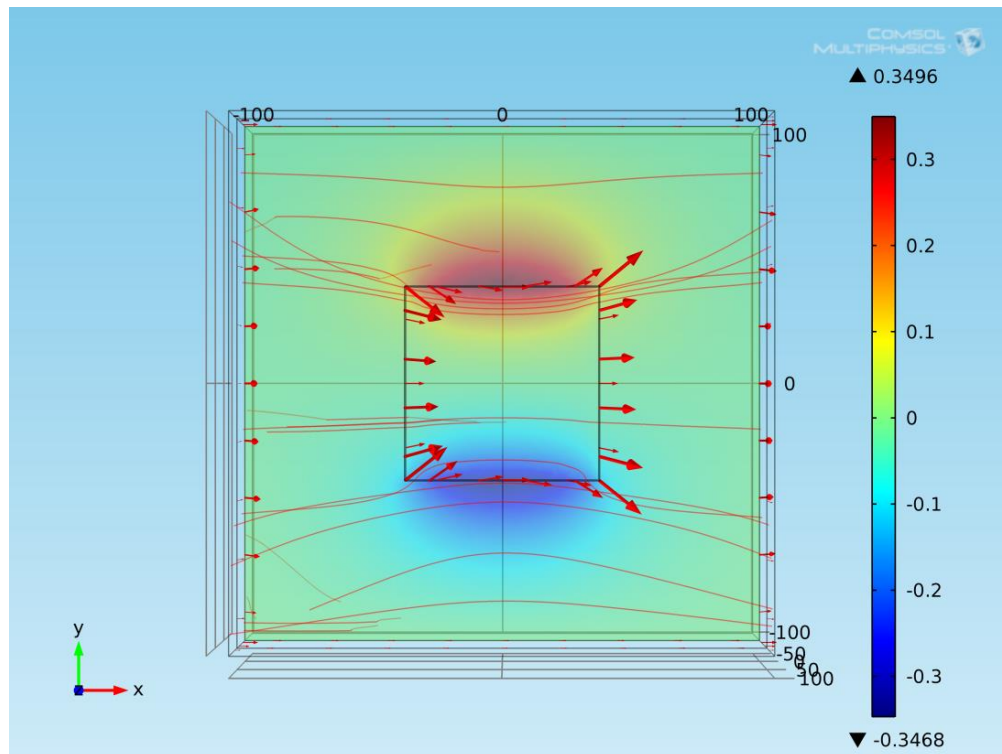


Figure 4.9 Top view of inphase Response in Lake Model. The streamlines describe orientation of the electric field in the air and in the ground. The arrows represent the current flowing in the ground. The slice plot represents inphase plot on the surface.

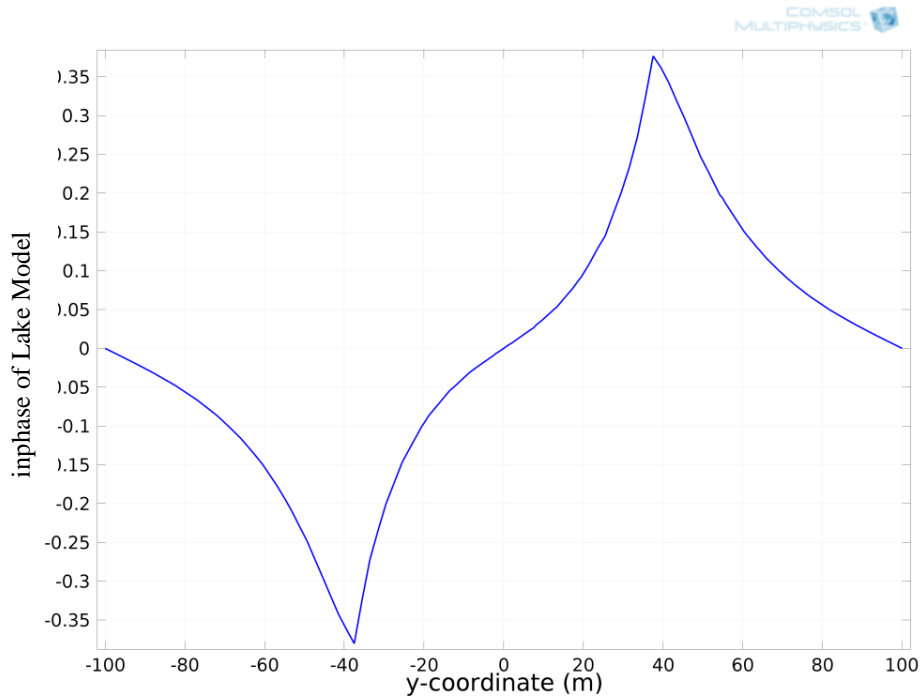


Figure 4.10 Inphase Response in Lake Model at X=0 & Z=0 along Y axis.

Figures 4.11 and 4.12 display the Quad responses of the lake model. Unlike the inphase plots, there are a couple of points of discontinuous derivatives. On the edge of the lake along the Y axis, we can observe the maximum and minimum points. On each side of those turning points, the slopes are determined by the different materials (water and ground). This agrees with the prior studies of the vertical contact. However, within the lake, the Quad reading flips between positive and negative.

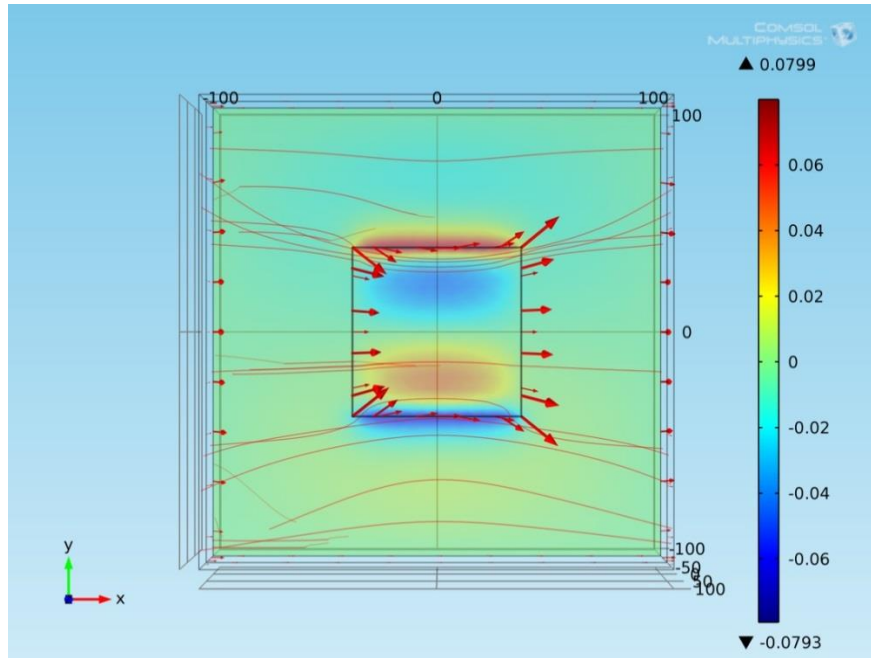


Figure 4.11 Top view of Quad Response in Lake Model. The streamlines describe orientation of the electric field in the air and in the ground. The arrows represent the current flowing in the ground. The slice plot represents Quad plot on the surface.

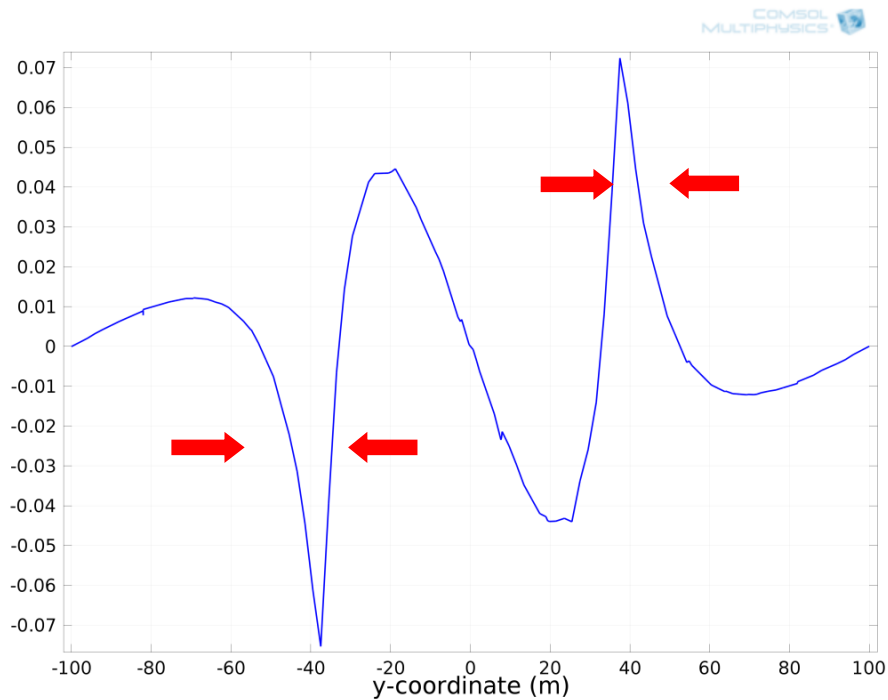


Figure 4.12 Quad Response in Lake Model at X=0 & Z=0 along Y axis

A different geometry of lake is also studied. In the model, the lake is changed to a half sphere of radius 37.5 m. Compared to the square shaped lake model, the current in the lake is affected less on the edges. The current is mainly running parallel to the wave propagation direction rather than mainly parallel to the lake edge. From figure 4.13 and 4.14, the half spherical shaped lake model has a small inphase reading and a greater Quad reading. The percentage of maximum inphase and Quad changes are 12.9% and 12.4 %.

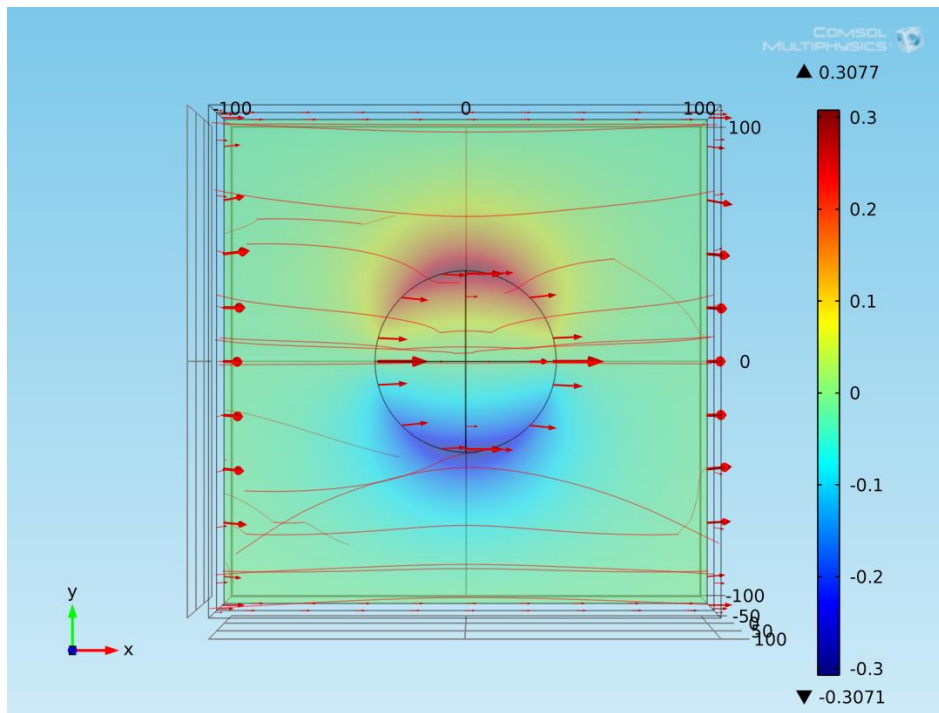


Figure 4.13 Top view of inphase Response in Lake Model of Half Sphere Shape. The streamlines describe orientation of the electric field in the air and in the ground. The arrows represent the current flowing in the ground. The slice plot represents inphase plot on the surface.

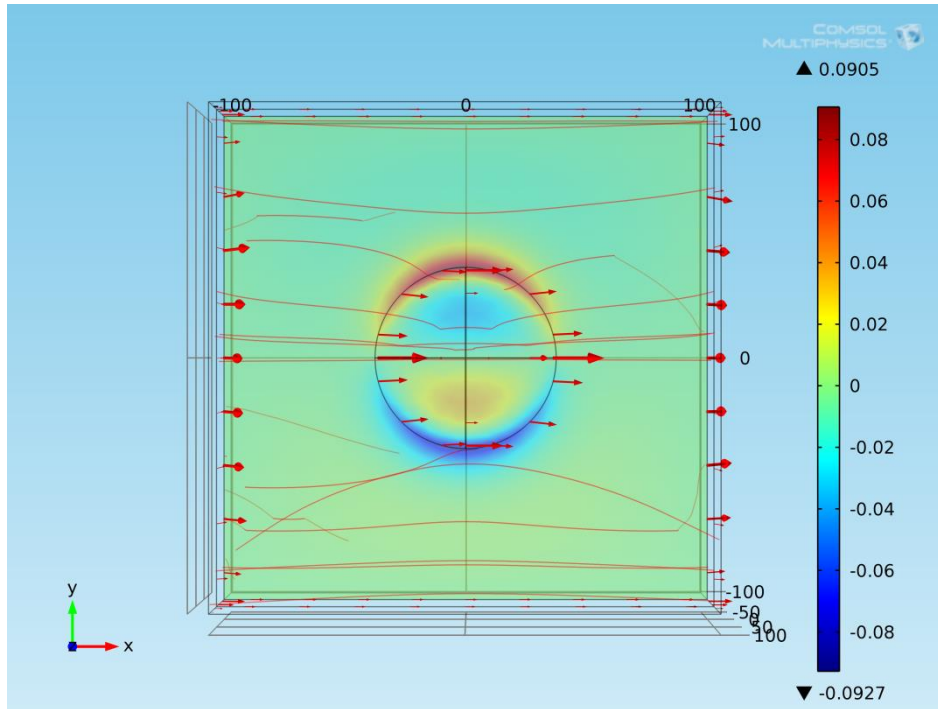


Figure 4.14 Top view of Quad Response in Lake Model of Half Sphere Shape. The streamlines describe orientation of the electric field in the air and in the ground. The arrows represent the current flowing in the ground. The slice plot represents Quad plot on the surface.

The lake model can be thought of as a conductive object buried near the surface. In nature, the resistivity of water varies from lake to lake, and pure water has a very high resistivity. However, lakes and rivers usually have fairly high concentrations of dissolved ions and so fairly low values of resistivity and in most cases the water is more conductive than surrounding ground material.

The lake model is a combination of layer modeling and vertical contact modeling. Taking the square shaped lake model as an example, the four vertical surfaces are vertical

contacts and the two horizontal surfaces are layers. Like those models, the inphase and Quad are mainly dominated by the resistivity contrast ratio and the ratio of skin depth to the depth of the lake. When the resistivity contrast increases, it tends to have a bigger inphase and Quad response. When the ratio of skin depth of lake water to the actual depth of the lake decreases, which also means the electromagnetic signal is blocked more by the lake, less effect of the bottom layer can be observed in the inphase and Quad response.

CHAPTER 5

SASKATOON DIEFENBAKER HILL

MODELS AND ANALYSIS

In 2012, a detailed VLF survey at Diefenbaker Hill, which is located in Diefenbaker Park of Saskatoon, was carried out to investigate the topographic effect on VLF data.

The survey spacing was three meters. Three different frequencies were recorded: 24 kHz (station located in Cutler, Maine & azimuth of 277 °) 24.8 kHz (station located in Jim Creek, Washington & azimuth of 82 °) and 25.2 kHz (station located in LaMoure, North Dakota & azimuth of 322 °). The orientations of electromagnetic waves generated from each transmitter station are shown in figure 5.1. GPS data and the resistivity of the ground at each measurement spot were also recorded. A Wenner array with 1m spacing between each electrode was chosen for the resistivity survey.

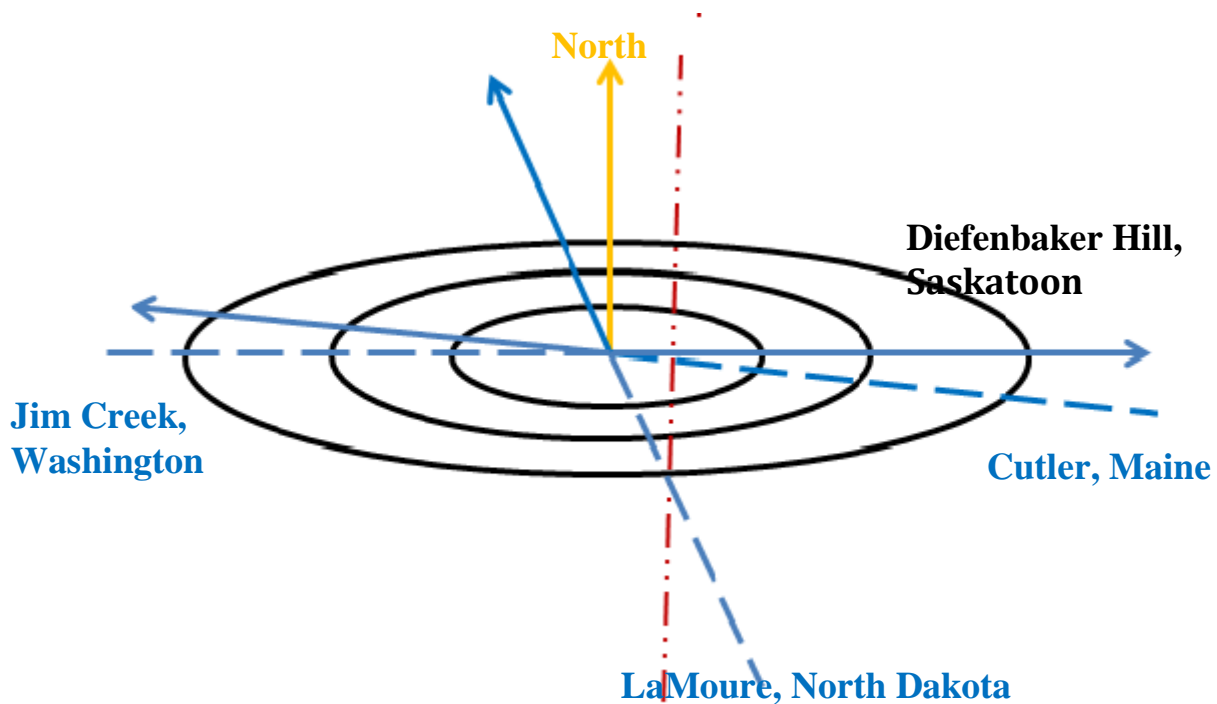


Figure 5.1 Azimuth plots for different transmitter stations. The black lines show an approximate contour map of Diefenbaker Hill, and the yellow line indicates the direction of North. The red dotted line represents the measurements profile.



Figure 5.2 VLF Measurement equipment

The VLF data is recorded using a ground system (EDA module F0151 & omni plus A151) as shown in figure 5.2. This ground system requires a single operator and uses a backpack configuration. This system is comprised of a data recorder (left side in the figure 5.2) and a sensor (right side in the figure 5.2). Since VLF measurements do not need ground contact, the operator can gather data very fast and there is capability for high volume surveying with minimal cost.

This VLF system measures a variety of parameters which includes inphase, Quad, Tilt, Total Field, DIR, CULT, 4-FRA, and 5-FRA for individual frequencies. The frequencies are input into the data recorder prior to the field measurement. The inphase and Quad are percentage values. The Tilt is the arctan of inphase in degrees. The Total Field is a

reference value with no unit, but it is proportional to the magnitude of the magnetic field. The DIR is the angle in degrees between the direction the operator is facing and the direction of wave propagation. CULT is a field that you can enter if there is something that might cause “cultural” noise like a fence or power lines. 4 FRA and 5 FRA are Fraser filtered values.

The measured inphase and Quad of three different frequencies are plotted in figures 5.3 and 5.4. As seen in figure 5.1, the azimuth directions of 24 kHz and 24.8 kHz are nearly 180 degrees to each other, so they have similar VLF responses which can be observed in figure 5.3. Also the directions of the 24 kHz and 24.8 kHz waves are close to parallel to the strike of the hill which makes their cases an approximately TE mode and they have a bigger response than those of the 25.2 kHz wave which can also be seen in figure 5.3. From the resistivity survey data, 100 ohm*m is roughly the value of ground resistivity and therefore the skin depth can be calculated to be 35m. The width of the hill is roughly 50m which gives a skin depth / hill width ratio of roughly 0.7. Based on the trend functions $y = 0.3531x^{-0.965}$ and $y = 0.1893x^{-0.783}$ (figures 4.4 and 4.5), the max inphase / max slope & max Quad / max slope can be calculated at values of 0.5 and 0.25. The slope of the hill is calculated by taking the derivation of the survey GPS data. As shown in figures 5.3 and 5.4, inphase and Quad responses are consistently matching the change of the slope of the hill. In figure 5.3, the inphase component from the 24 kHz (Cutler, Maine) and 24.8 kHz (Jim Creek, Washington) fit better with the 0.5 times the slope curve while 25.2 kHz (LaMoure, North Dakota) is a little offset. The similar results can be observed in figure 5.4.

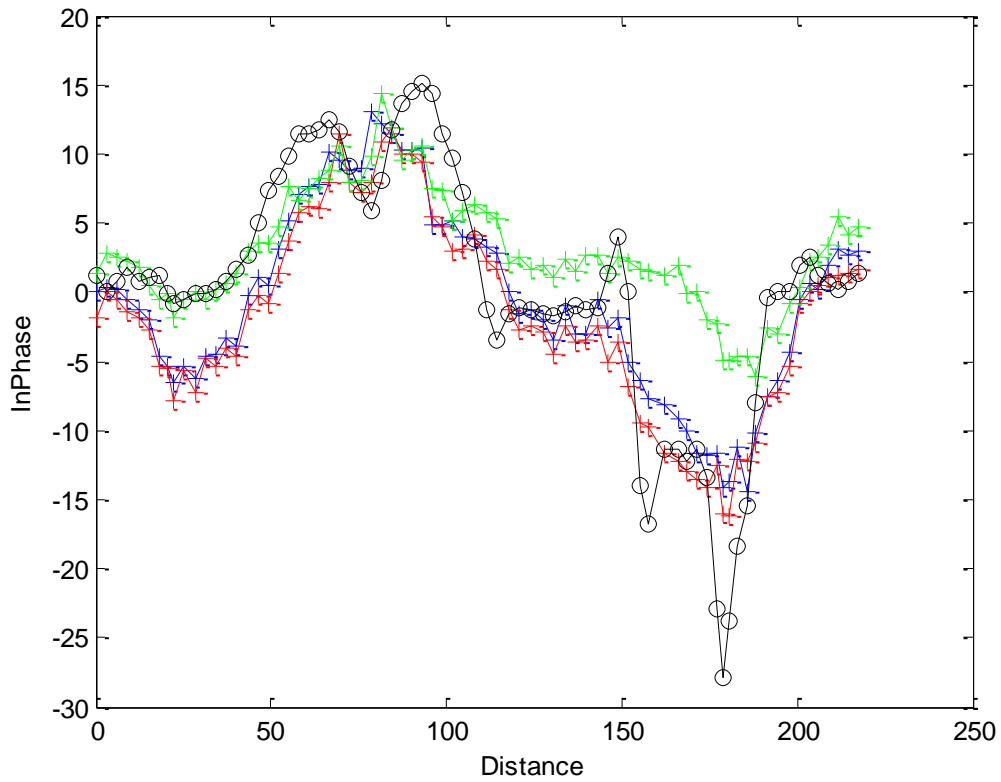


Figure 5.3 Field inphase reading vs. distance and 0.5 times slopes of Diefenbaker hill. The blue plot represents frequency of 24 kHz, the red plot represents frequency of 24.8 kHz, and green plot represents frequency of 25.2 kHz. The black plot represents 0.5 times of the slope of the Diefenbaker hill.

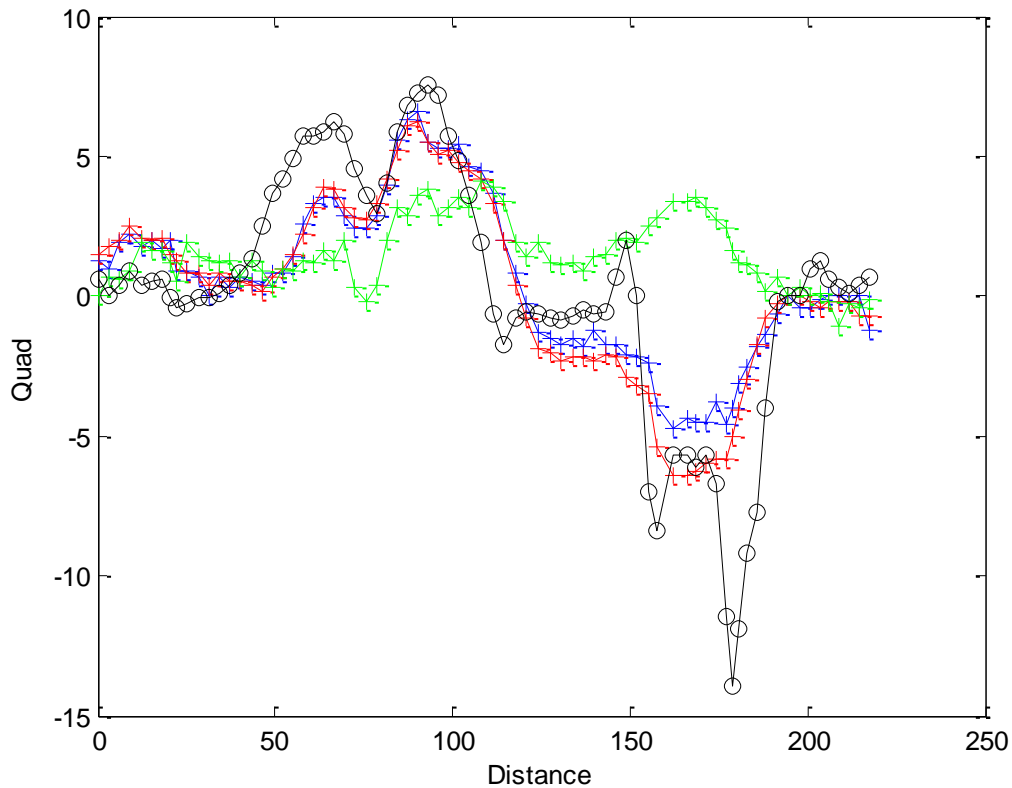


Figure 5.4 Field Quad reading vs. distance and 0.25 times slopes of Diefenbaker hill. The blue plot represents frequency of 24 kHz, the red plot represents frequency of 24.8 kHz, and green plot represents frequency of 25.2 kHz. The black plot represents 0.25 times of the slope of the Diefenbaker hill.

Figures 5.5 and 5.6 are additional plots of 25.2 kHz inphase and Quad field reading. The azimuth of 25.2 kHz wave, θ , is approximate 46 degrees. The inphase and Quad plots should fit better with $0.5 * \cos(46^\circ)$ and $0.25 * \cos(46^\circ)$ times slopes of Diefenbaker hill. The inphase plot is not too far off while the Quad plot does not fit well. The reason causing the differences in the Quad plot could be that the measurement data have small amplitudes and the signal to noise ratio is smaller.

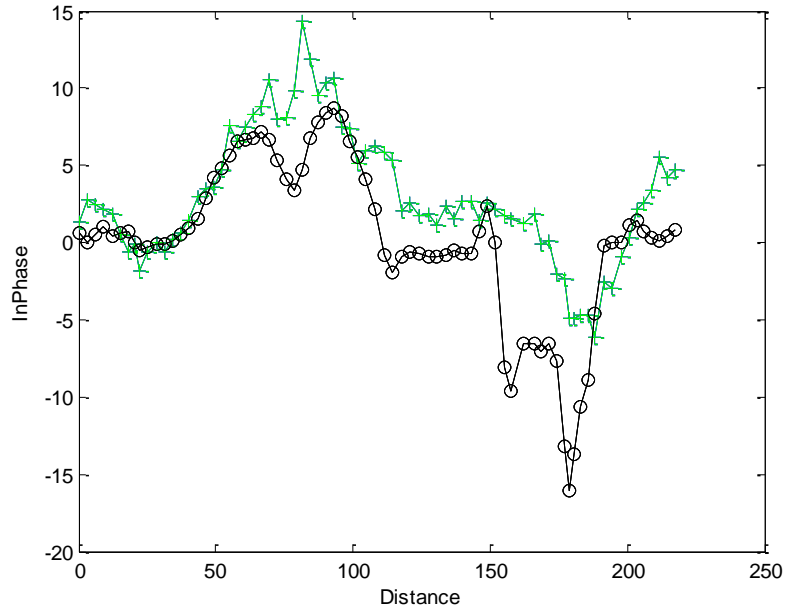


Figure 5.5 25.2 kHz inphase reading vs. distance and $0.5 \times$ slopes of Diefenbaker hill $\times \cos(46^\circ)$. The green plot represents frequency of 25.2 kHz. The black plot represents 0.5 times of the slope of the Diefenbaker hill times $\cos(46^\circ)$.

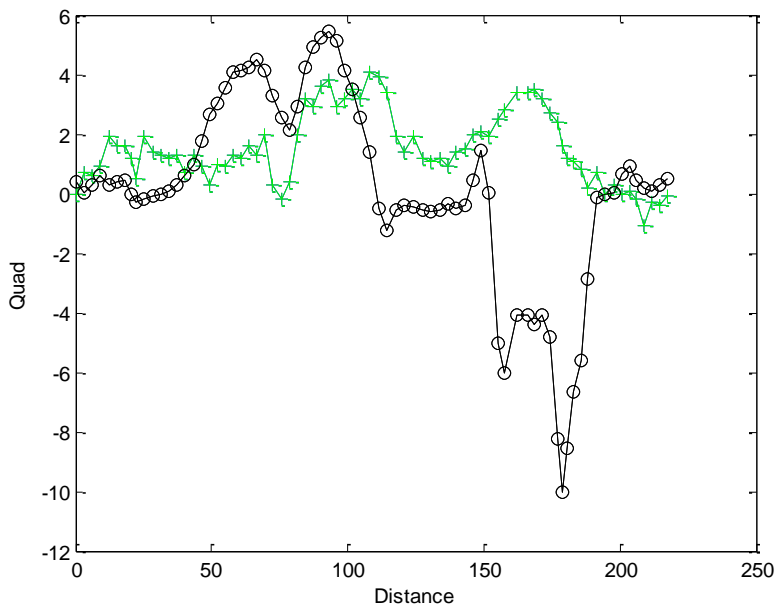


Figure 5.6 25.2 kHz Quad reading vs. distance and $0.25 \times$ slopes of Diefenbaker hill $\times \cos(46^\circ)$. The green plot represents frequency of 25.2 kHz. The black plot represents 0.25 times of the slope of the Diefenbaker hill times $\cos(46^\circ)$.

Diefenbaker hill is modeled using Comsol to investigate the topographic effect on VLF data. As shown in figure 5.7, a best fitting Gaussian function is calculated based on the GPS data, and input as topography into the Comsol model. A value of 0.01 S/m for ground conductivity is used which is roughly the average from the resistivity survey data. Figure 5.8 shows the 3D simulation results for the frequency of 24 kHz. The color slice represents the simulated quadrature responses of the topographic effect. The comparisons between simulation results and measurement data for the 24 kHz wave are plotted in figure 5.9 and 5.10. As can be seen, the amplitudes of inphase and Quad responses of the measurements and simulation results are similar. However the simulated hill is 2D and the resistivity of the ground is assumed to be constant, and so the simulated results are smoother than the measured ones.

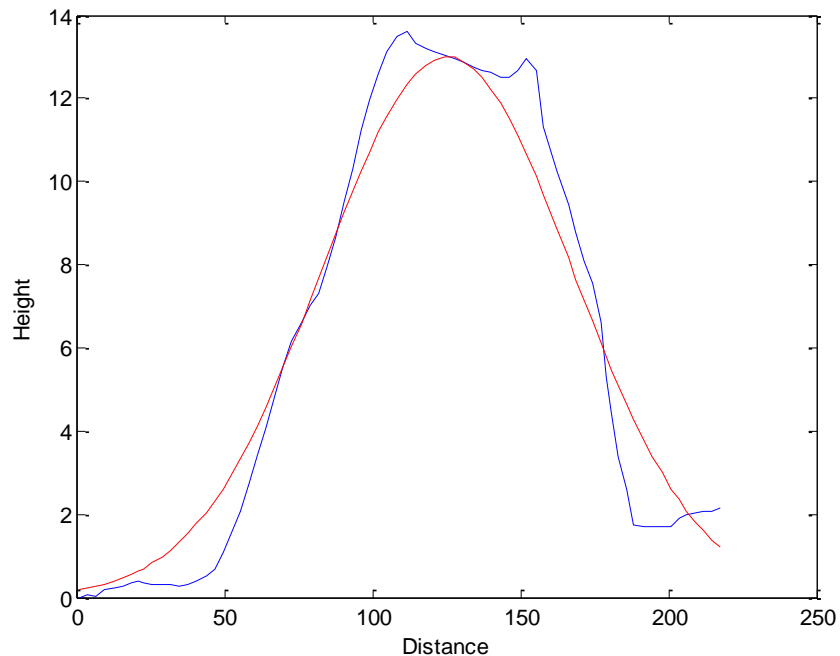


Figure 5.7 Topographic profiles of Diefenbaker hill (blue line) and best fitting Gaussian function (red line)

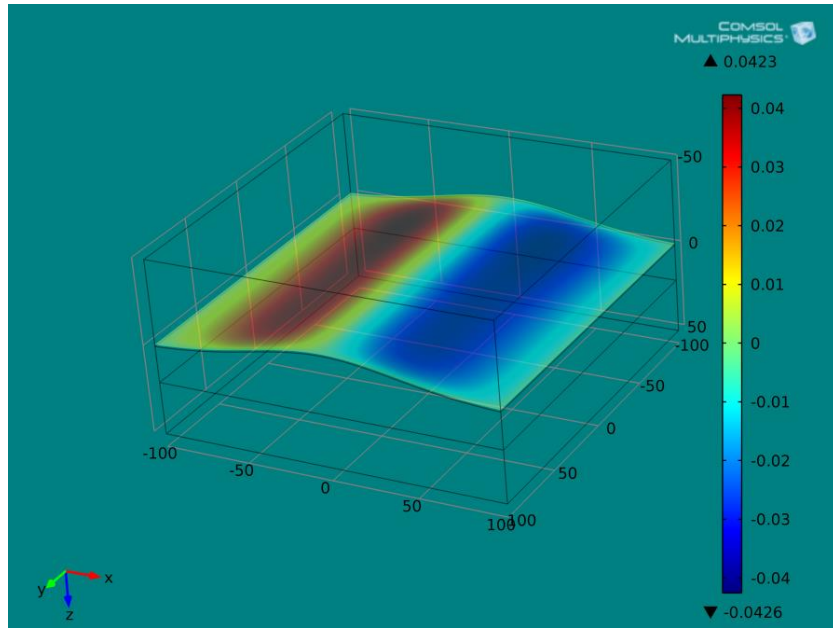


Figure 5.8 3D simulation results of Diefenbaker hill at 24.8 kHz. The color slice represents the simulated quadrature responses of the topographic

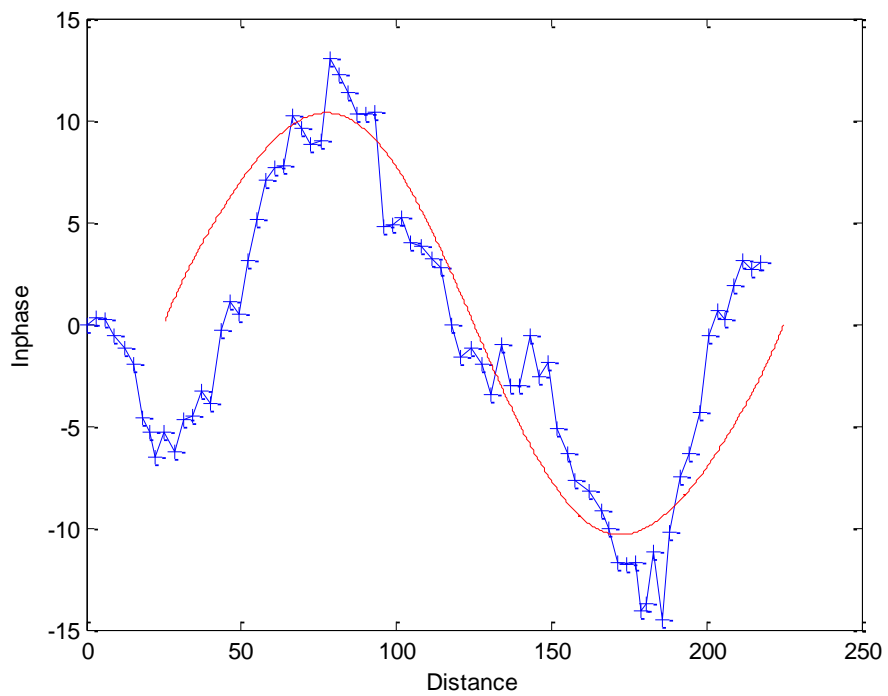


Figure 5.9 Field measurement and simulation results comparison of inphase components of 24 kHz

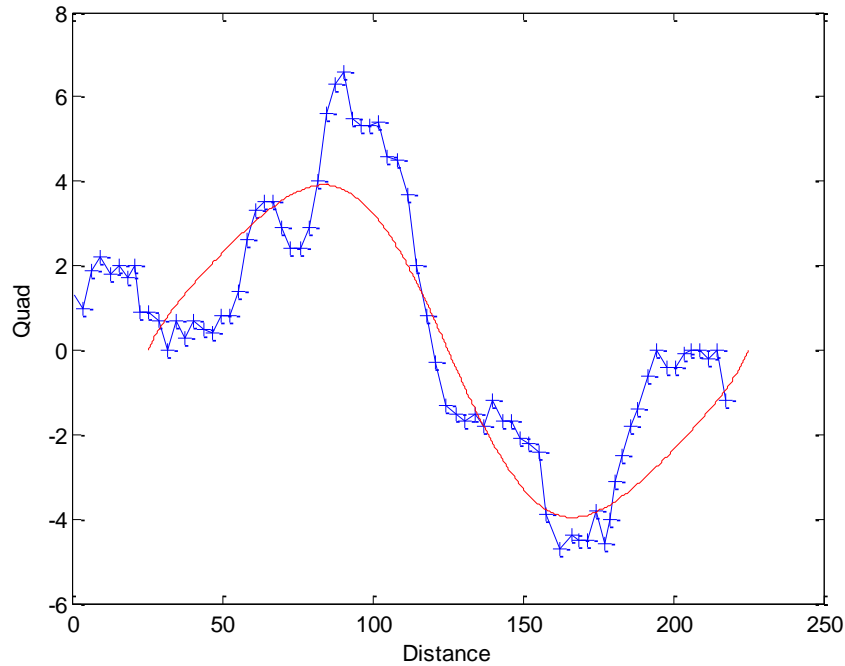


Figure 5.10 Field measurement and simulation results comparison of quadrature components of 24 kHz

The waves with frequencies 24.8 kHz and 25.2 kHz with different azimuths are also modeled. The simulation results of inphase & Quad and measurement data are plotted in figures 5.11 to 5.14. As illustrated, the 24.8 kHz (Jim Creek) and 24 kHz (Cutler) are both approaching the TE mode. As a result, larger inphase and Quad responses can be expected. Figures 5.11 and 5.12 show that the simulation results of inphase and Quad have the same shape as the measured data and the range also matches. However the simulation results of 25.2 kHz (LaMoure) do not quite match the data. The inphase plots have the same shape but offset values. The Quad measurement data of 25.2 kHz all have positive values rather than fluctuating about 0. This could be caused by the reading values being small and approaching to the noise level.

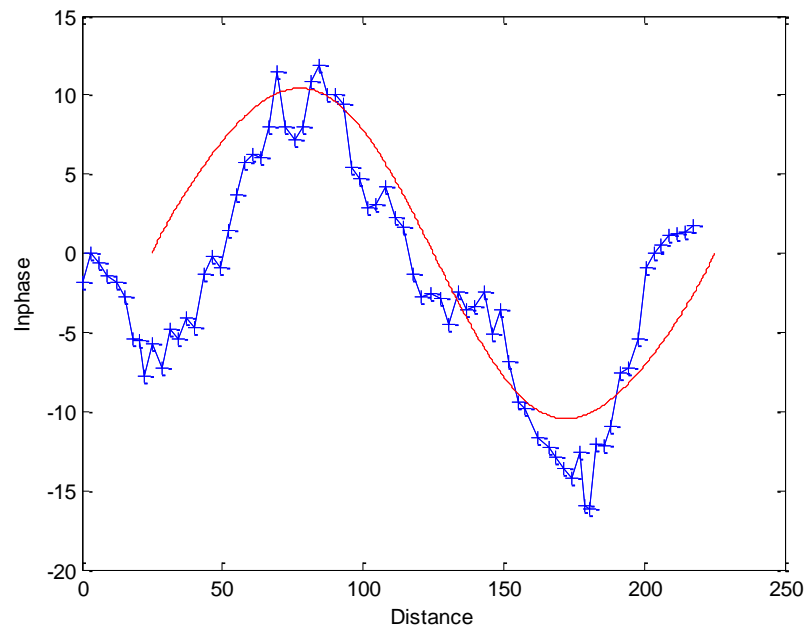


Figure 5.11 Field measurement and simulation results comparison of inphase components of 24.8 kHz

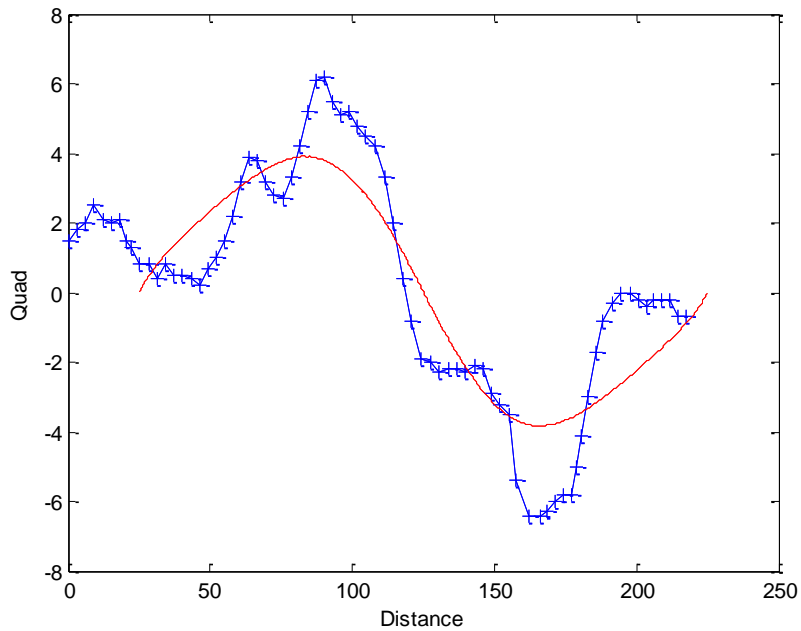


Figure 5.12 Field measurement and simulation results comparison of quadrature components of 24.8 kHz

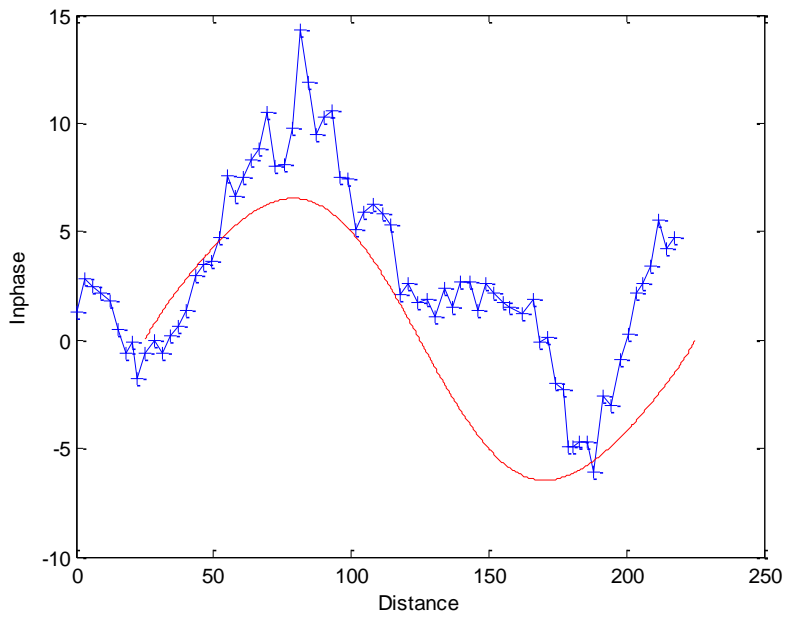


Figure 5.13 Field measurement and simulation results comparison of inphase components of 25.2 kHz

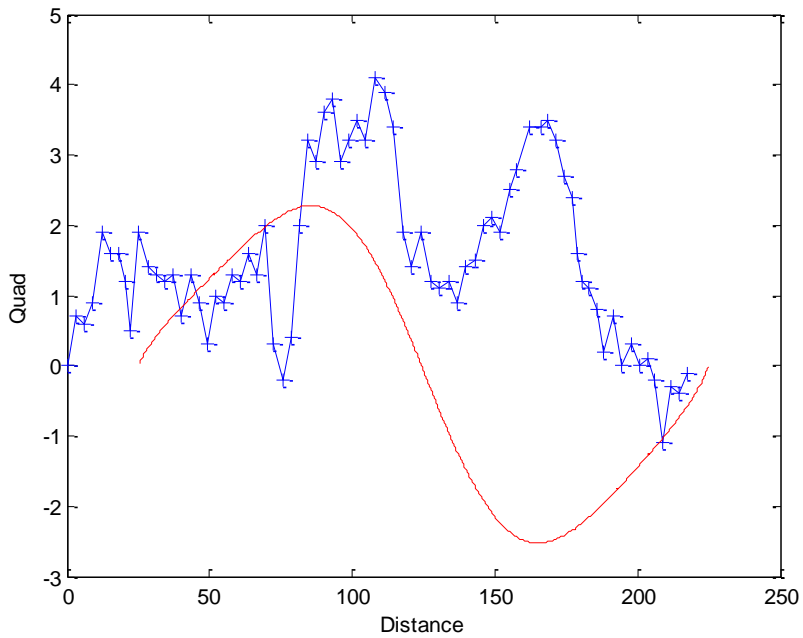


Figure 5.14 Field measurement and simulation results comparison of quadrature components of 25.2 kHz

CHAPTER 6
CAMECO CREE EXTENSION
VLF SURVEY & SIMULATION

Between July 15th and July 24th, 2006, personnel from Cameco Corporation performed a VLF survey over a one square kilometers region near Slush Lake using EM16 equipment. The purpose of the survey was to detect, if possible, shallow structure in an area where the Millennium mineshaft is to be placed. Two different frequencies were recorded which are NAA 24 kHz (station located in Cutler, Maine) and NLK 24.8 kHz (station located in Jim Creek, Washington).

On September, 2012, Tyler Mathieson from Cameco Corporation, Mary Liang (graduate student) and I carried out a VLF and resistivity survey over the same region. The VLF survey was following the same cut lines as the survey in 2006, but different equipment (figure 5.2) was carried and an additional frequency of 25.2 kHz (station located in LaMoure, North Dakota) was recorded. Resistivity surveys were carried out at several different locations in the region as well. The purpose of the survey was to compare the different equipment recordings, and investigate the topographic and lake effects in the region.

The topography of the Cameco Cree extension region is plotted in figure 6.1. The elevations of the region range from 530m to 558m. Three hills trend NE to SW crossing the map (labeled Hill #1, #2 and #3) , and two lakes are located in the NW corner and the middle of the map (labeled Lake #1 and #2).

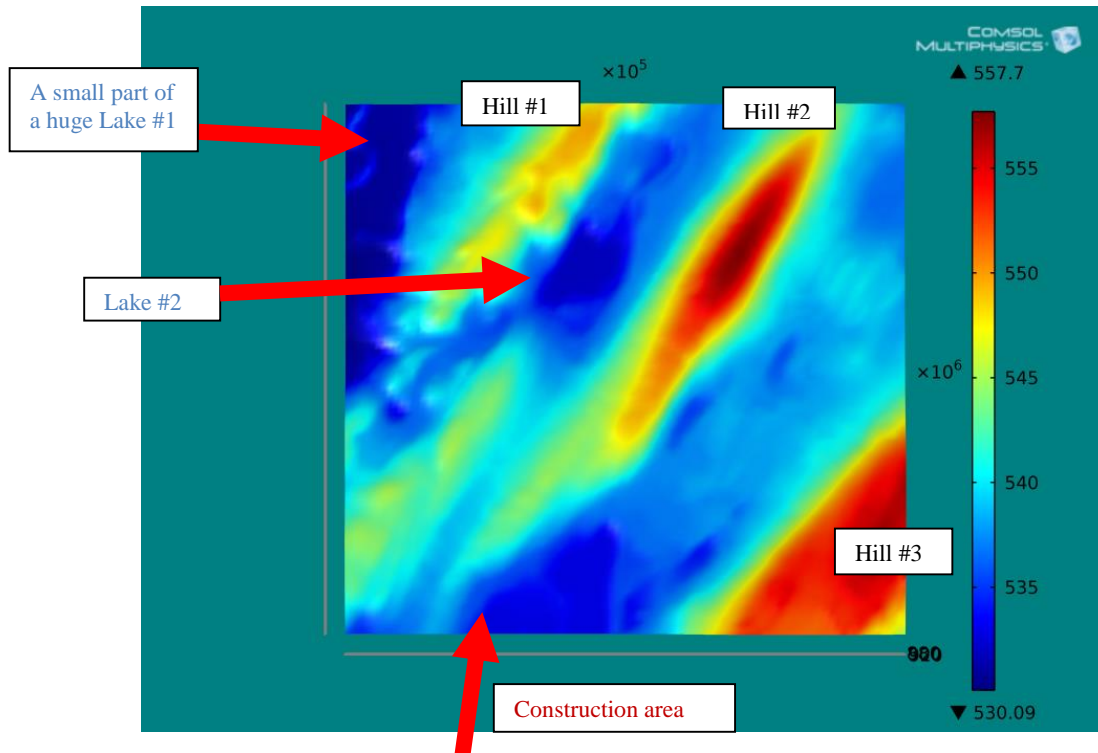


Figure 6.1 Topography of Cameco Cree Extension regions in meters.

Figures 6.2 and 6.3 show the 2006 original Cameco VLF measured inphase and Quad data of 24k Hz (NAA) over the region. The electromagnetic wave generated from Cutler, Maine is propagating in the roughly southeast to northwest direction. The magnetic field is perpendicular to the direction of wave propagation and parallel to the strikes of hills in the region; therefore, lesser inphase and Quad readings of 24 kHz are expected. In figures 6.2 and 6.3, there are no patterns that can be observed to indicate lakes or hills in the region. However, due to the existence of the huge lake in the northwest corner (Lake #1) and the construction area where a lot of power lines are underground in the south (indicated in the figure 6.1), the readings at those two spots are extremely high or low compared to the rest of the data. These large contrasts make it more difficult to identify more subtle features in the plotted data.

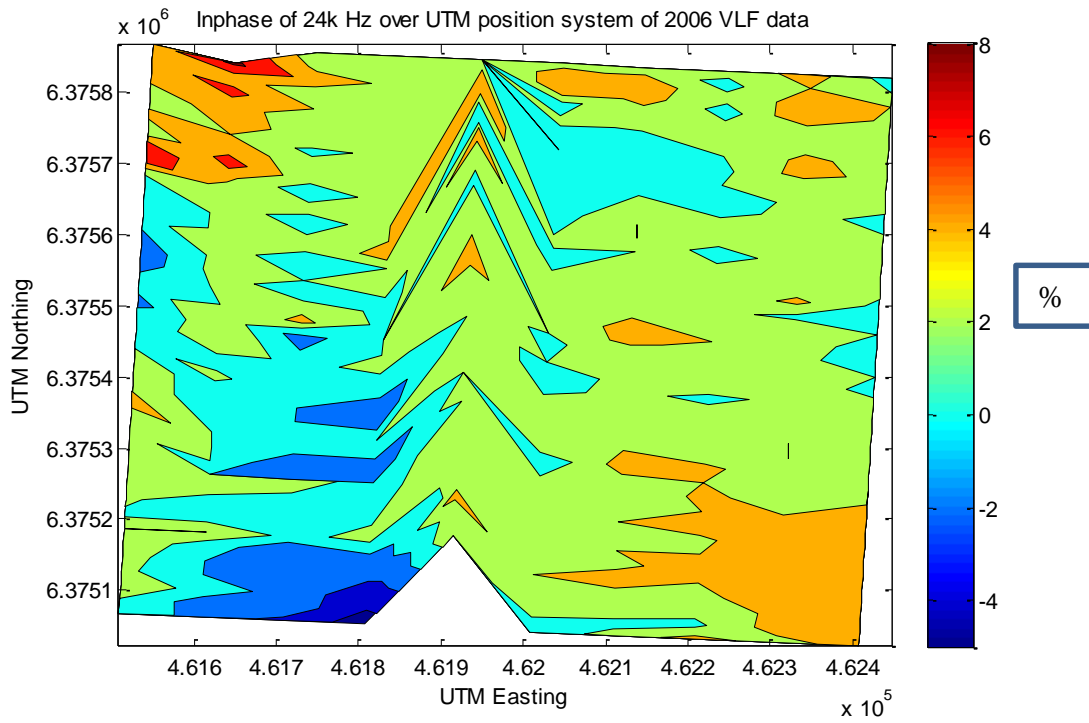


Figure 6.2 Inphase of 24k Hz over UTM position system of 2006 VLF data

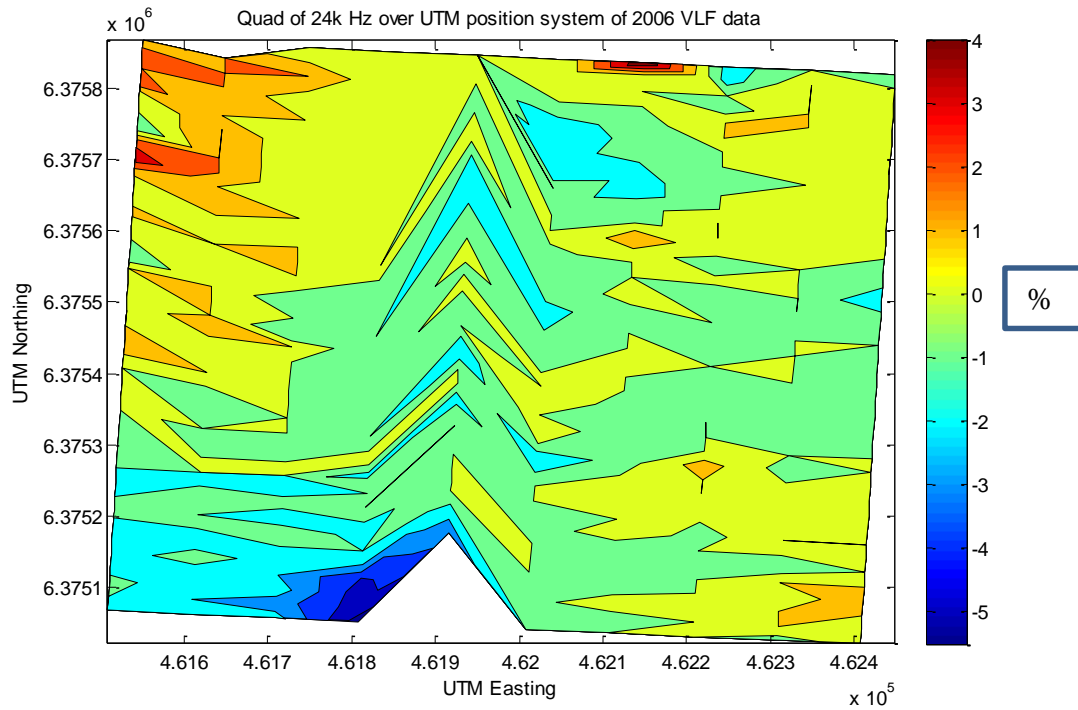


Figure 6.3 Quad of 24k Hz over UTM position system of 2006 VLF data

Figures 6.4 and 6.5 show the 2006 original Cameco VLF measured inphase and Quad data of 24.8 kHz (NLK) over the region. The electromagnetic wave generated from Jim Creek, Washington is roughly propagating in the southwest to northeast direction, and bigger responses of inphase and Quad could be predicted. In the both figures, the evidences of the huge lake (Lake #1) effect on the VLF data are obvious. In figure 6.4, the data in the rest of the region are relatively flat and no hill effects are observed. But in figure 6.5, a clear anomaly along the strike of hill #2 can be seen and it is marked with the red circle. However, the hill effects in the southeast corner are not noticeable.

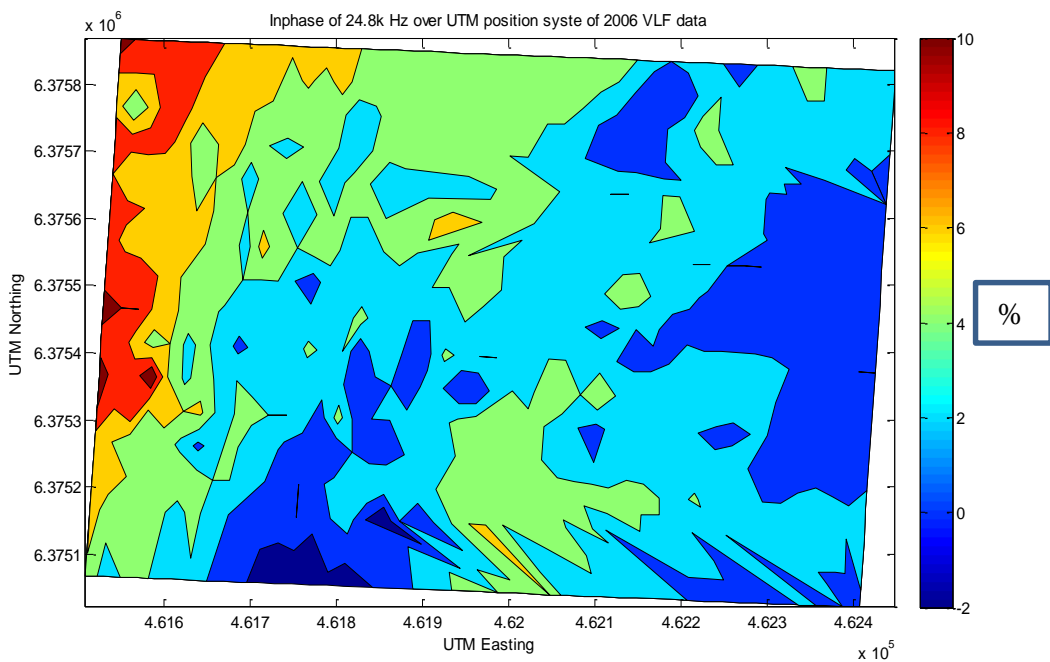


Figure 6.4 Inphase of 24.8 kHz over UTM position system of 2006 VLF data

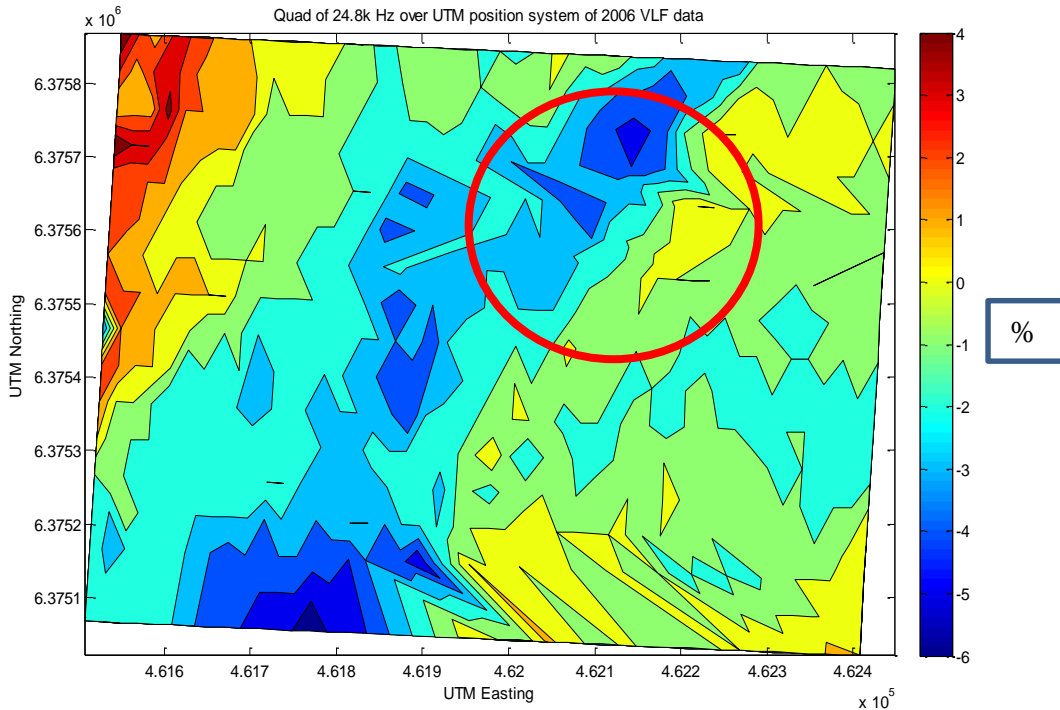


Figure 6.5 Quad of 24.8 kHz over UTM position system of 2006 VLF data

In order to examine smaller amplitude variations, Cameco staff reduced the range of the color scale. The modified Quad data plots of 24 kHz and 24.8 kHz are shown in figures 6.6 and 6.7. In figure 6.6, as can be seen, the range of the data is changed from 12% to 4%. However, due to the wave propagation direction, still no patterns can be observed to be correlated with hills or lakes. In figures 6.7, the range of the data is changed from 10% to 5%, and three anomalies can be identified with one side having negative values and one side having positive values. These three anomalies are marked with red lines, and they approximate the strikes of the three hills in the region.

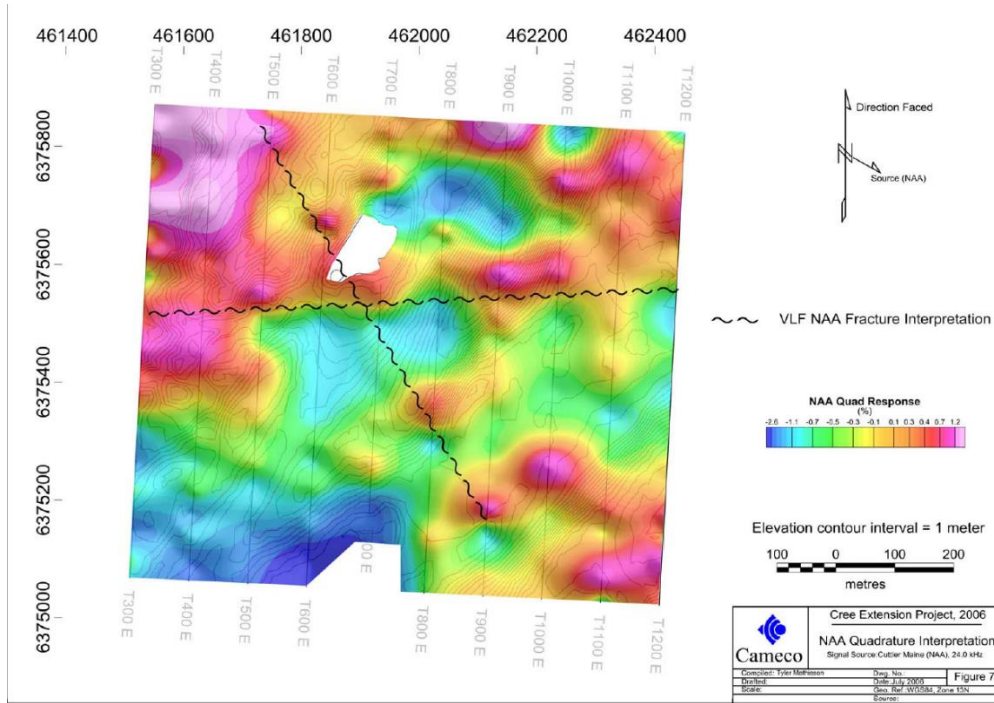


Figure 6.6 2006 Cameco NAA fixed Quad data (Mathieson, July 2006)

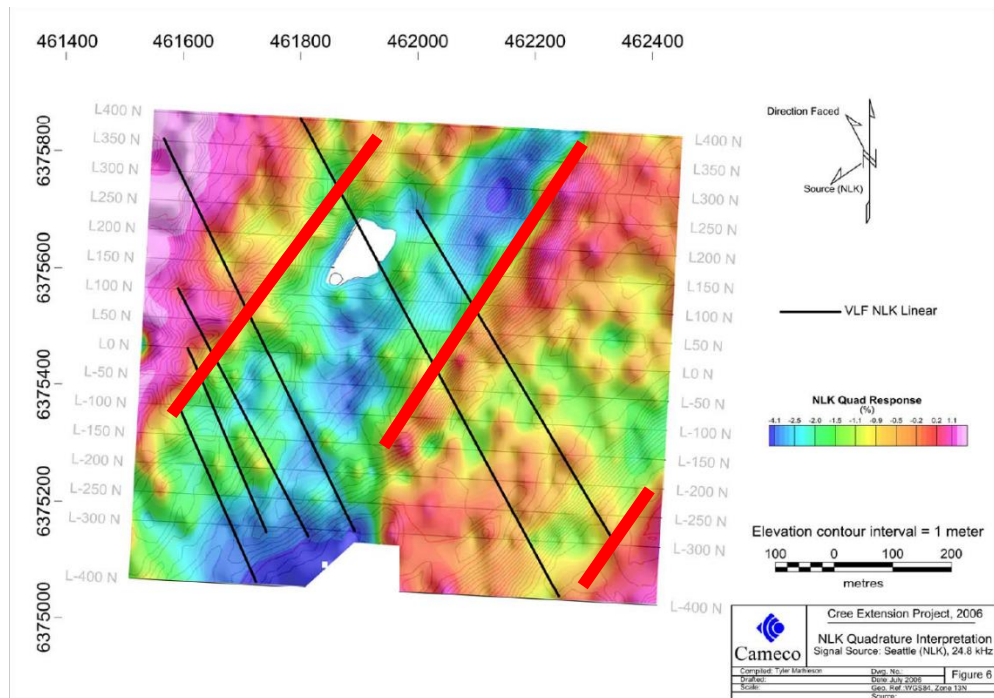


Figure 6.7 2006 Cameco NLK fixed Quad data (Mathieson, July 2006)

The 2012 measurement data are plotted in figure 6.8 to figure 6.15. The positions of measurement lines over the topographic map are shown in figure 6.8. Blue, red, black and green colors indicate the data of different measurement lines. Unfortunately, the data are not sufficiently dense to generate a contour map.

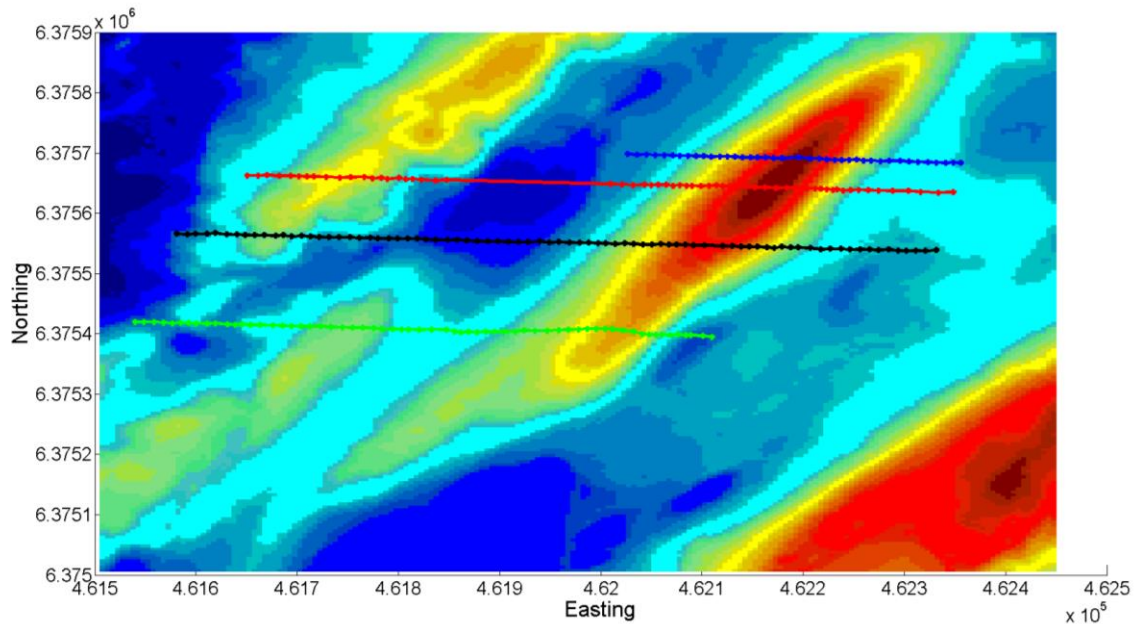


Figure 6.8 Positions of four different measurement lines of 2012 VLF data

Figures 6.9 and 6.10 are inphase and Quad plots measured at frequency 24 kHz of 2012 VLF data. Blue, red, black and green colors indicate the data of different measurement lines. Compared to the data in 2006, the 2012 inphase data is in the same range with the original data, while the 2012 Quad data is roughly in the same range with the 2006 optimized result (figure 6.7). Even though there are some changes in the measurement data, it is hard to connect them with the topographic or lake effects.

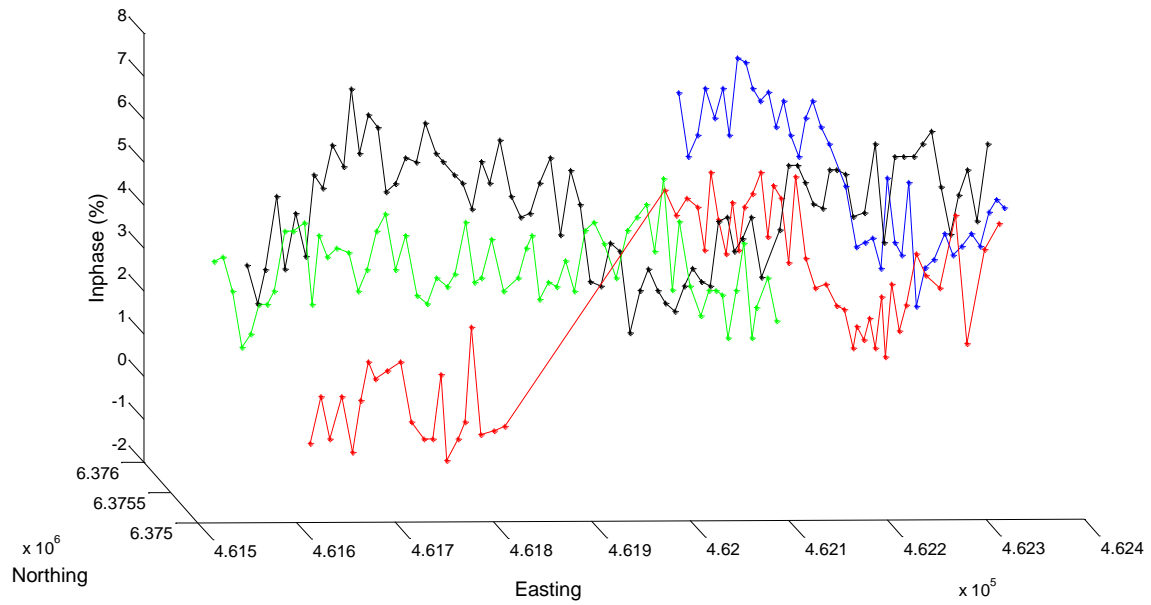


Figure 6.9 24 kHz inphase plot of 2012 VLF data. Each color represents a set of measurement data from the same colored measurement line in the figure 6.8.

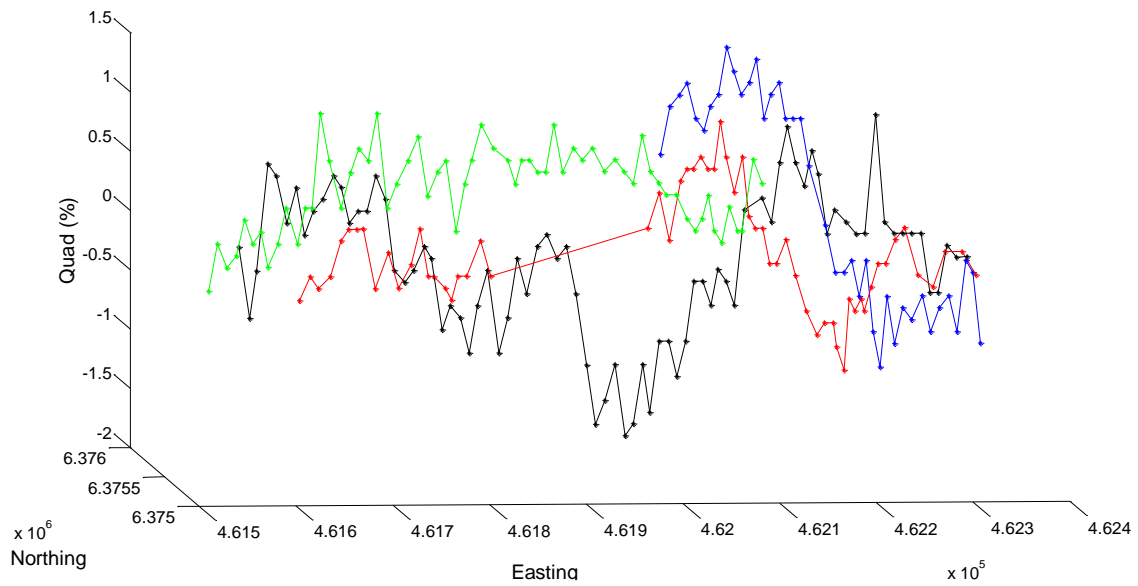


Figure 6.10 24 kHz Quad plot of 2012 VLF data. Each color represents a set of measurement data from the same colored measurement line in the figure 6.8.

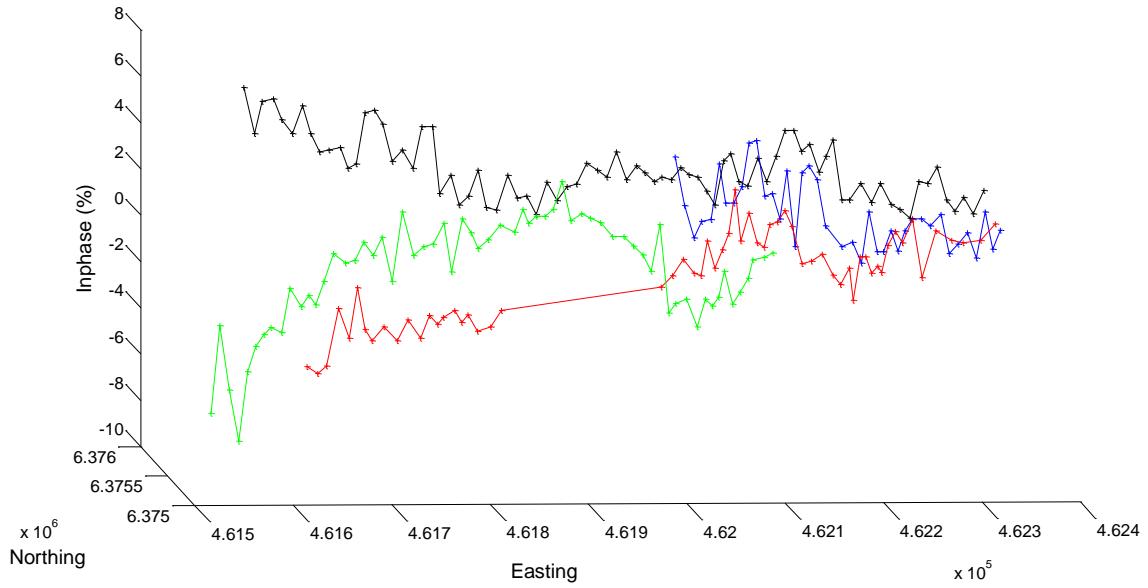


Figure 6.11 24.8 kHz inphase plot of 2012 VLF data. Each color represents a set of measurement data from the same colored measurement line in the figure 6.8.

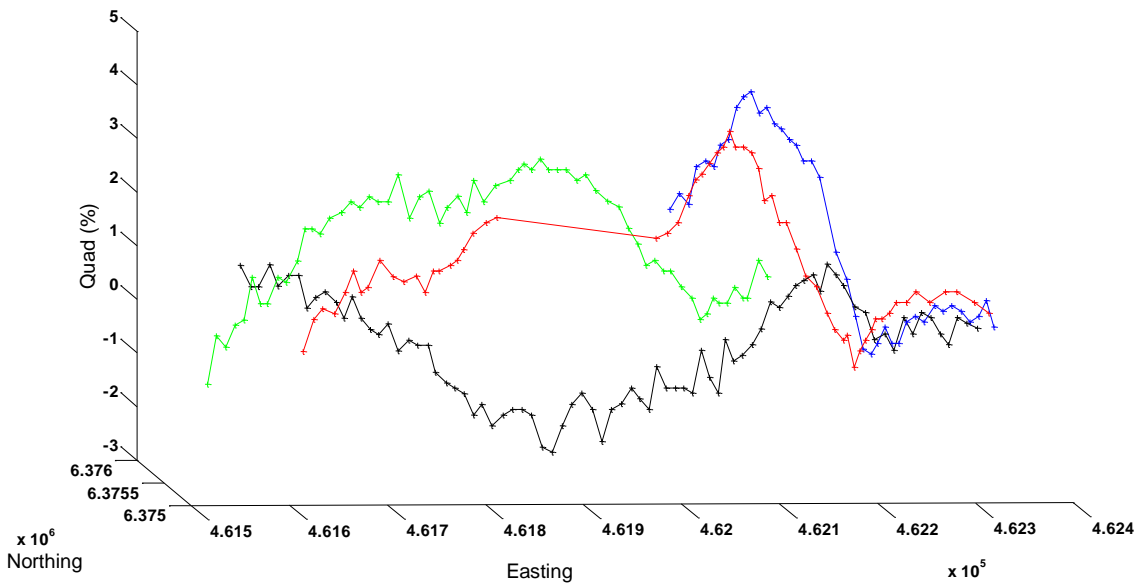


Figure 6.12 24.8 kHz Quad plot of 2012 VLF data. Each color represents a set of measurement data from the same colored measurement line in the figure 6.8.

Figures 6.11 and 6.12 are the inphase and Quad measurement data of 24.8 kHz in 2012. As discussed, we expect that the responses due to hills and lakes would be significant. Even though there is not much evidence shown to indicate the effects of hill #1 in each of measurement lines, hill #2 can be observed in the 2012 measurement data. An individual measurement line is chosen and plotted in figure 6.13. The blue color represents 0.3 times the GPS elevation data. 0.3 is chosen to match the data in the same range with no actual meaning. As seen, there is a maximum point and a minimum point when crossing hill #2. The left side marked with the black circle doesn't show any anomaly. The reason could be that the effects of Lake #1 are much greater than those due to hill #1 in the black circle region. Horizontal distance

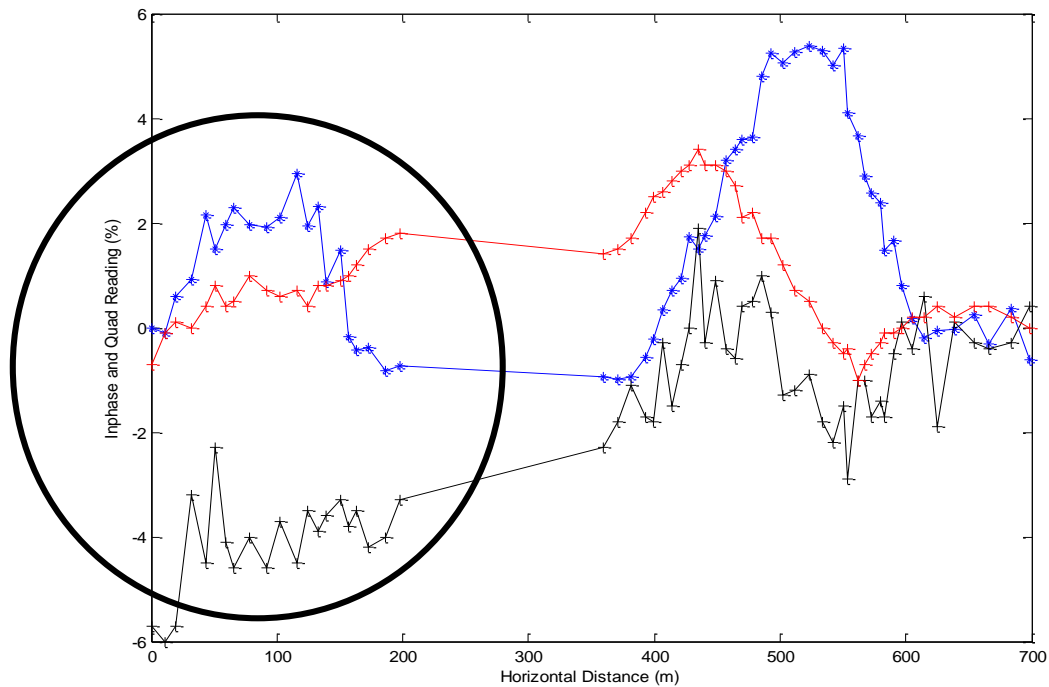


Figure 6.13 24.8k Hz inphase and Quad plot of an individual measurement line of 2012 VLF data. The blue color represents 0.3 times the GPS elevation data. The red color represents the inphase reading and the black color indicates the Quad reading.

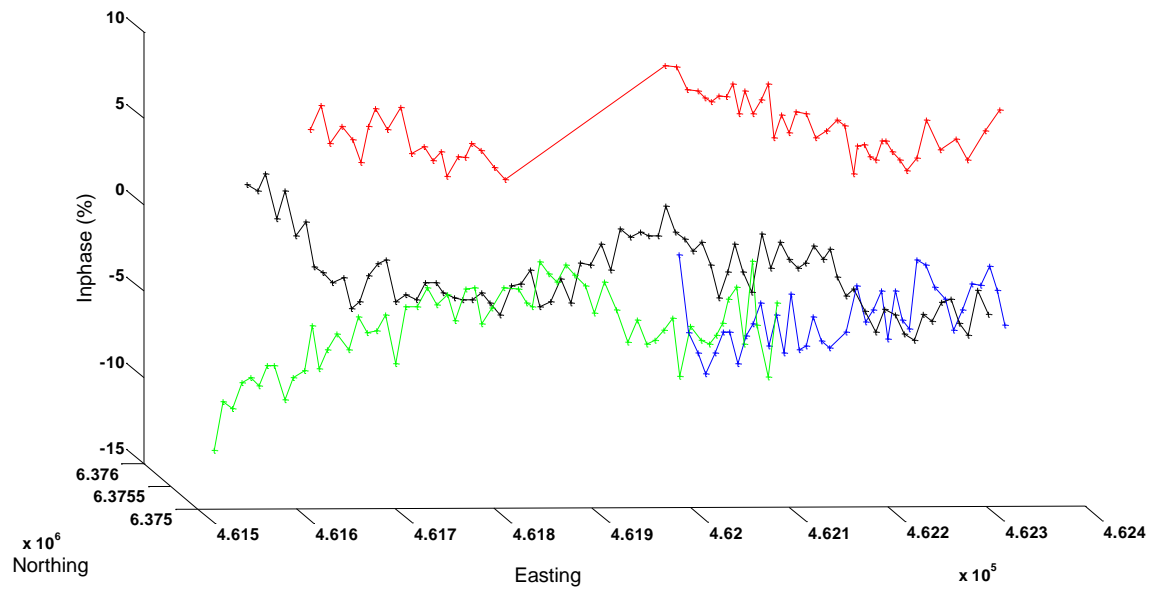


Figure 6.14 25.2 kHz inphase plot of 2012 VLF data. Each color represents a set of measurement data from the same colored measurement line in the figure 6.8.

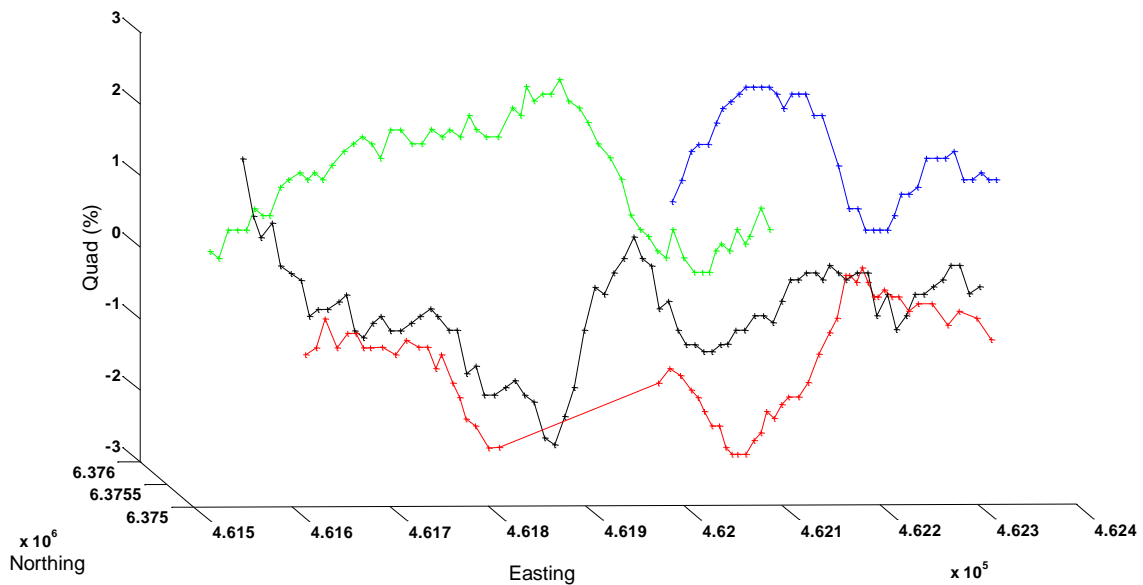


Figure 6.15 25.2 kHz Quad plot of 2012 VLF data. Each color represents a set of measurement data from the same colored measurement line in the figure 6.8.

Figures 6.14 and 6.15 are inphase and Quad plots of 25.2 kHz of 2012 VLF data. According to the azimuth directions of the three different frequencies, the wave propagation direction of 25.2 kHz (LaMour, North Dakota) lies between the directions of the 24 kHz and 24.8 kHz frequency waves. As per the prior discussion, measurements are expected to have smaller values while the 24.8 kHz signal is expected to be larger. The responses of 25.2 kHz are expected to be intermediate. As shown in figure 6.15, a VLF response of hill #2 can be observed in the right hand of the figure. Compared to the values in figure 6.12, a smaller response is seen, which is consistent with our expectations. Similar to the results of 24.8 kHz, there is not much to indicate hill #1.

Based on the Cameco topographic radar data in the region shown in figure 6.16, A VLF model of the region is created. The model is created at 895m (northing) * 945m (easting) * 300m (thickness), with 100m in the air and 200m underground. The actual topographic data are inputted into the model for the interface between the air and the ground. The survey in 2012 indicates the resistivity of the region is ranging from 5000 ohm*m to 20000 ohm*m. 5000 ohm*m and 10000 ohm*m of ground resistivity values are chosen, and the ground is treated as having constant resistivity.

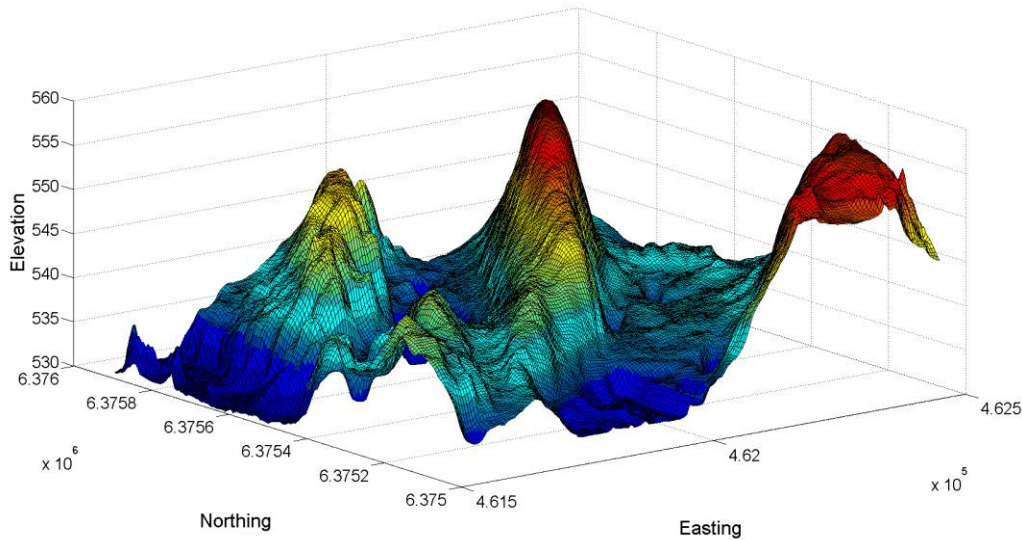


Figure 6.16 Cameco topographic radar data in Slush Lake region

The water quality and characteristics are typical of the Athabasca Basin with a relatively constant conductivity from 3 $\mu\text{S}/\text{cm}$ to 26 $\mu\text{S}/\text{cm}$ (Steane, 2009). An average value of 15 $\mu\text{S}/\text{cm}$ is used as the water conductivity in the simulations. Due to the large region modeled and the restrictions of the model resolution, both lakes in the model are deep. The small lake in the middle is modeled as a 140m * 140m square with 20m depth, and the large lake at the northwest corner is set as 439m * 96m with also 20m depth.

Two different frequencies are modeled at 24 kHz (NAA) with azimuth of 284 ° and 24.8 kHz (NLK) with azimuth of 40 °. The results are shown in the following figures. The legend in each figure in the left represents the elevation, and the legend in the right is the simulation results of inphase or Quad (times 100 for percentage values). The arrows indicate the direction of the current in the ground, and also the direction of the wave propagation.

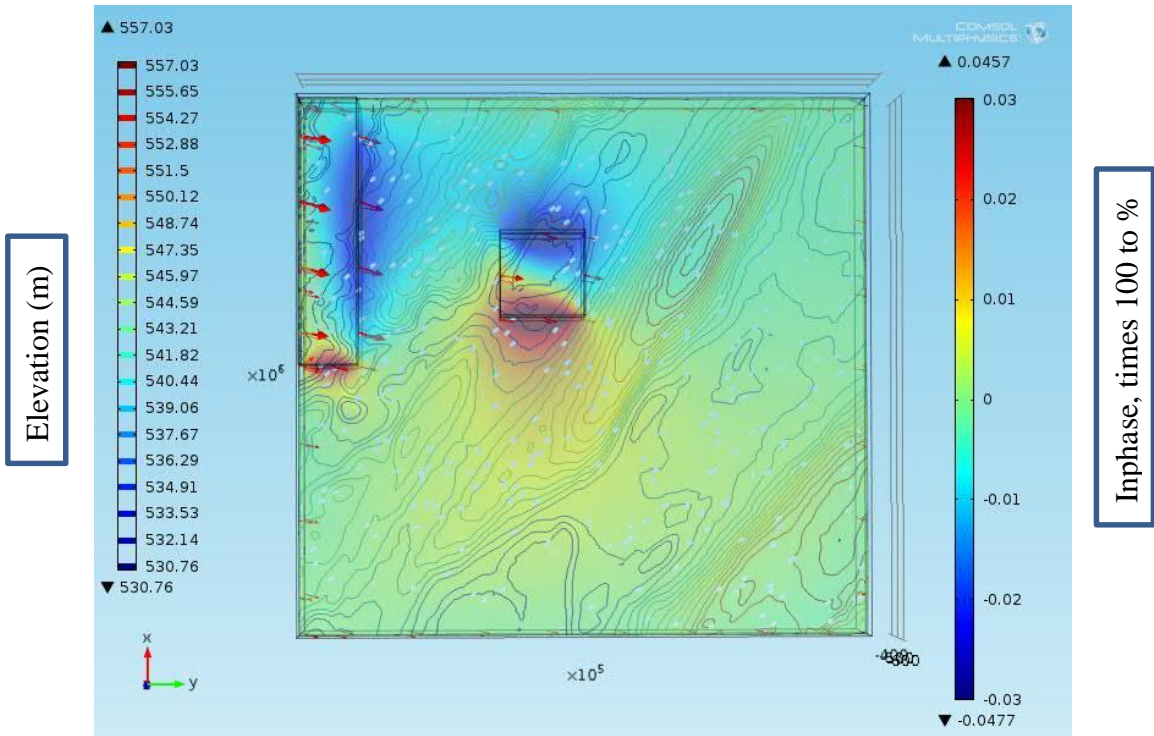


Figure 6.17 Slush lake inphase simulation plot of 24 kHz with 5000 ohm*m of ground resistivity

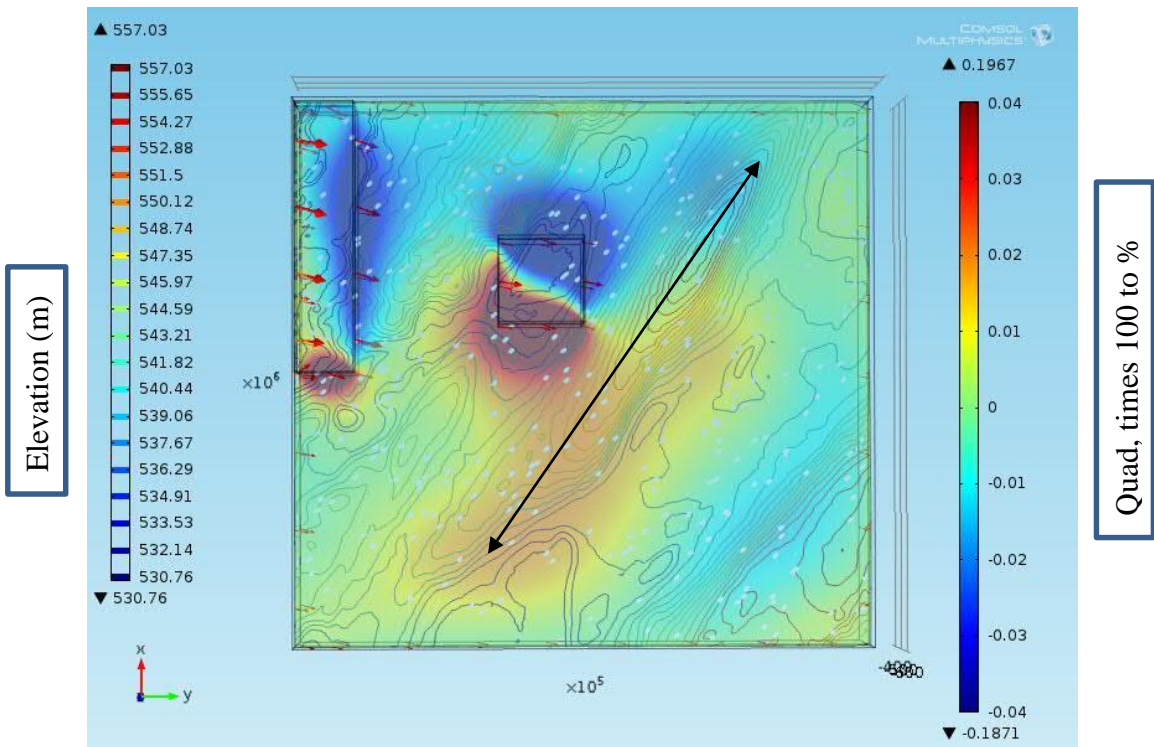


Figure 6.18 Slush lake Quad simulation plot of 24 kHz with 5000 ohm*m of ground resistivity

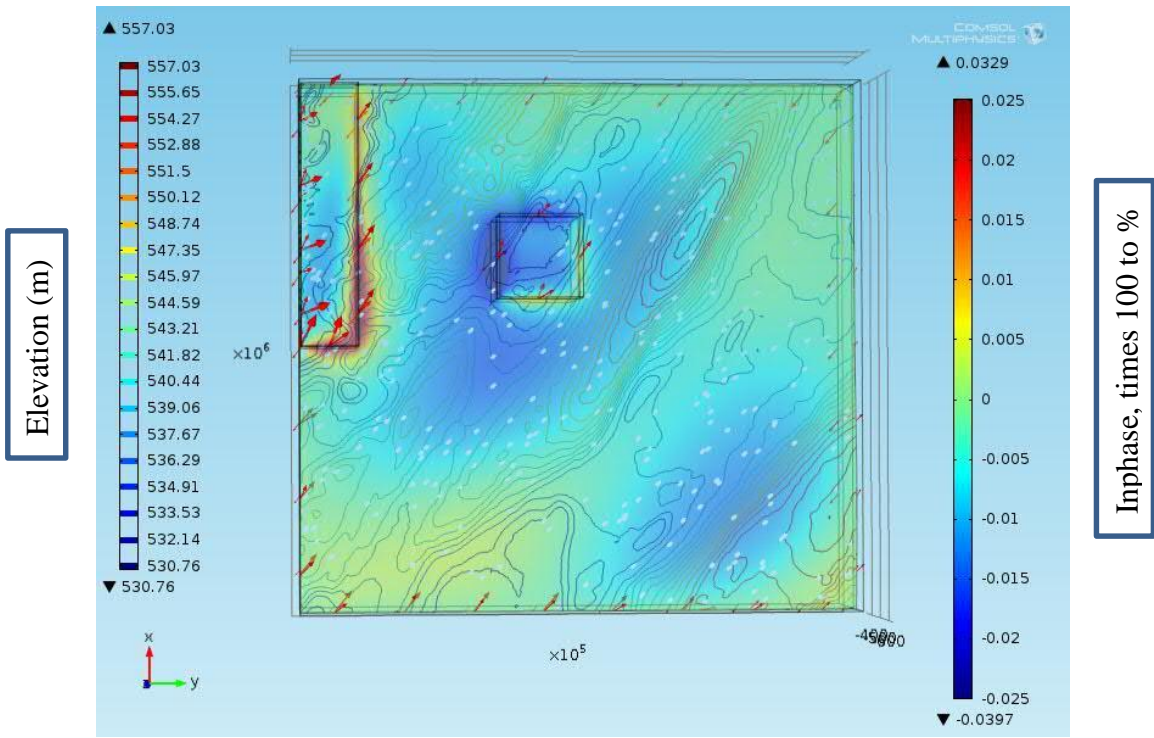


Figure 6.19 Slush lake inphase simulation plot of 24.8k Hz with 5000 ohm*m of ground resistivity

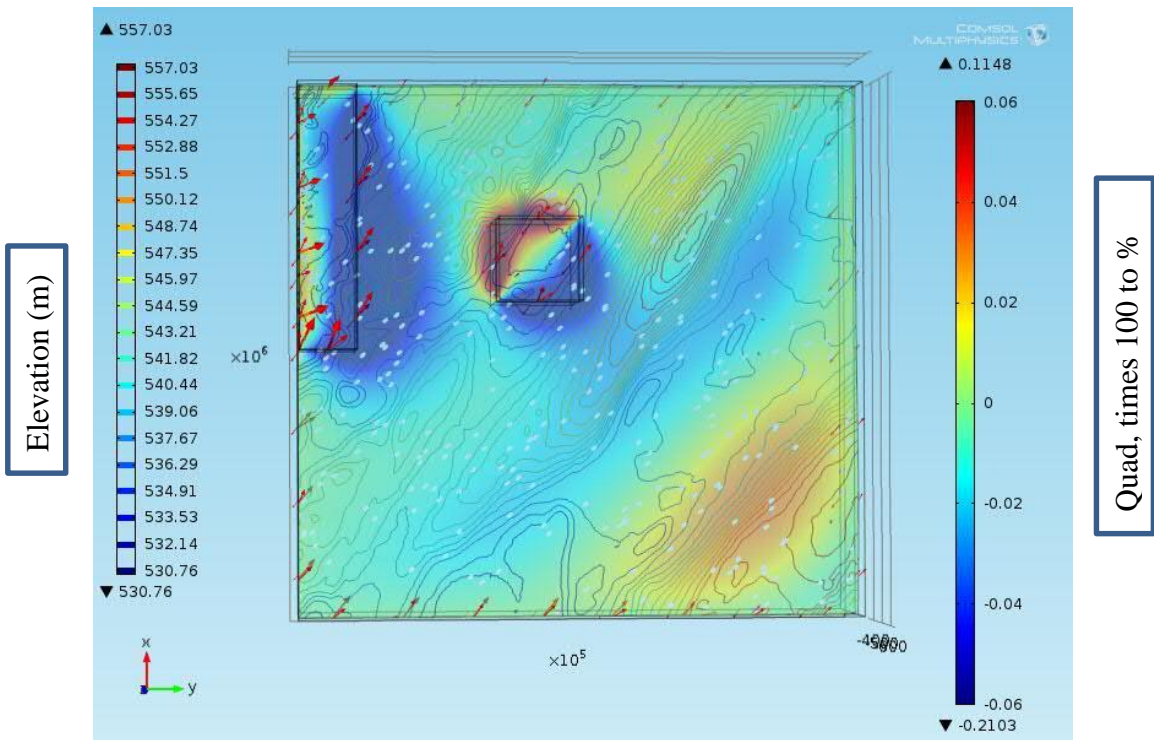


Figure 6.20 Slush lake Quad simulation plot of 24.8 kHz with 5000 ohm*m of ground resistivity

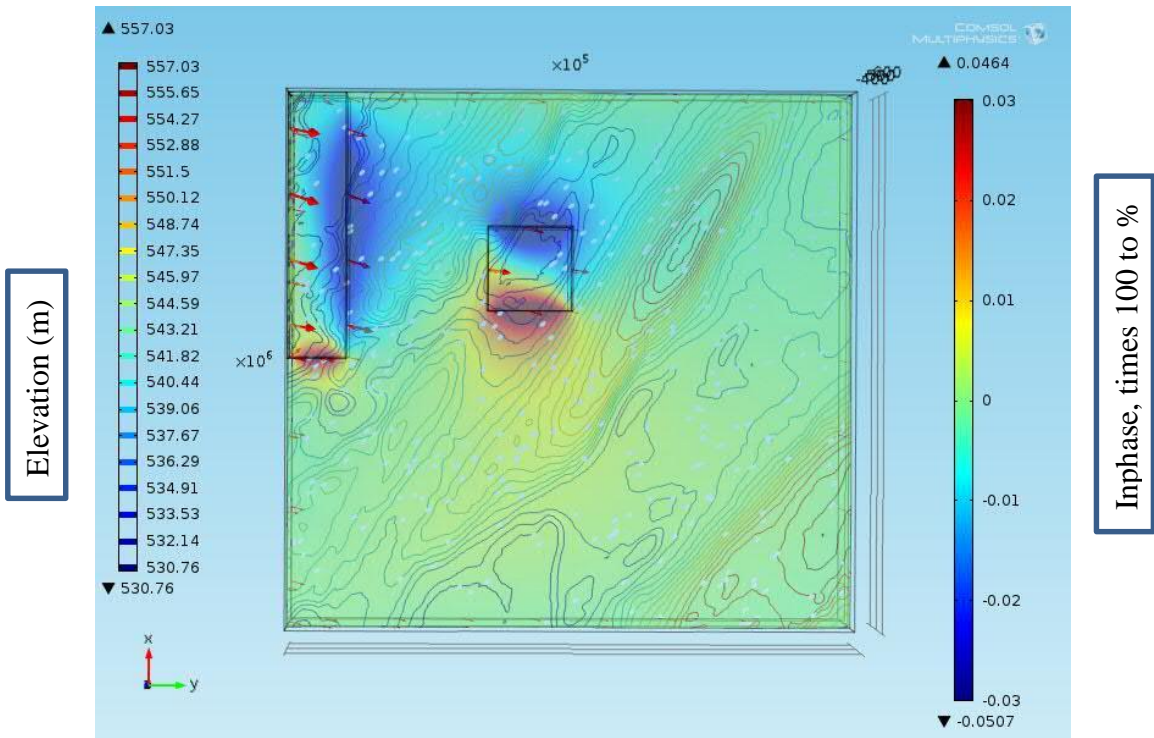


Figure 6.21 Slush lake inphase simulation plot of 24 kHz with 10000 ohm*m of ground resistivity

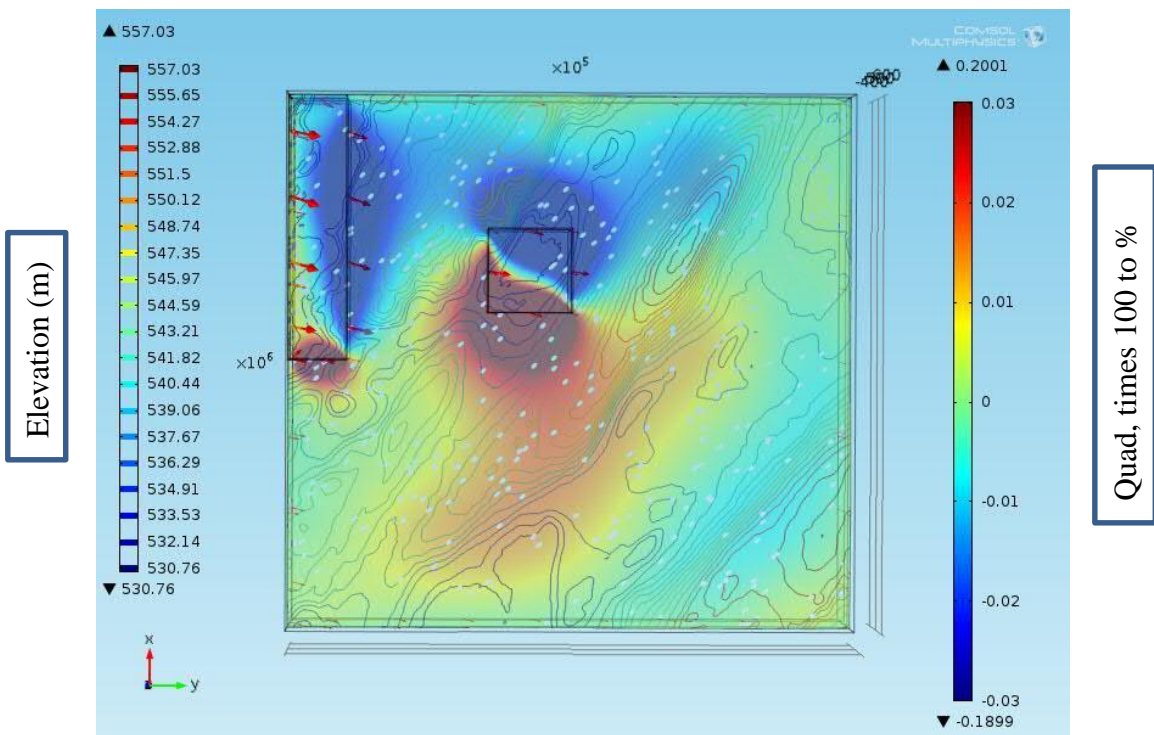


Figure 6.22 Slush lake Quad simulation plot of 24 kHz with 10000 ohm*m of ground resistivity

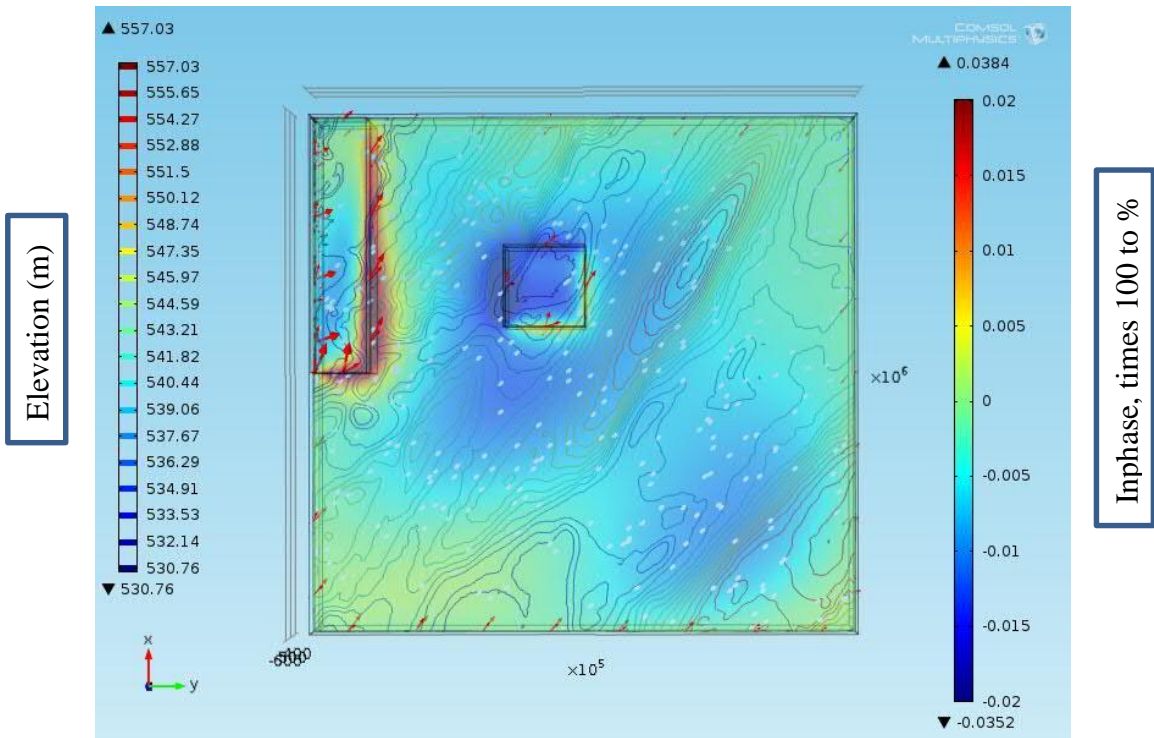


Figure 6.23 Slush lake inphase simulation plot of 24.8 kHz with 10000 ohm*m of ground resistivity

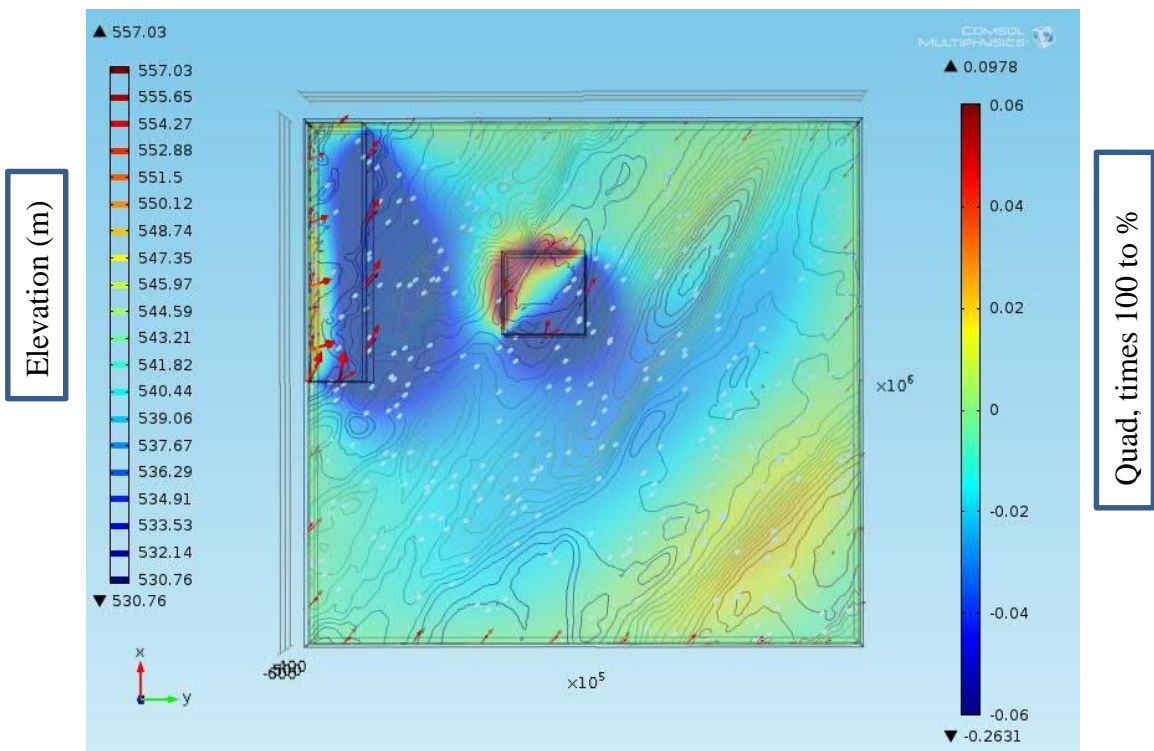


Figure 6.24 Slush lake Quad simulation plot of 24.8 kHz with 10000 ohm*m of ground resistivity

Due to the large conductivity contrast between the lake water and the ground, the two lakes affect the VLF data to a greater degree than the topography, and these large spikes make it impossible to see all of the simulation results in the region. In the last eight figures, the range of the color scale is reduced, so the effect of the hills can be observed. For example, in figure 6.18, the Quad simulations results range from 19.67% to -18.71%, while only 4% to -4% of results are shown in that figure.

When the ground has resistivity 5000 ohm*m, at NAA frequency (24 kHz), since the wave propagation direction is perpendicular to the strikes of the hill, less response is predicted. In figure 6.17, no hill effects can be seen, while in figure 6.18 only a small hill effect can be seen along the northeast to southwest direction which is indicated by the black arrows in the figure. At NLK frequency (24.8 kHz) of 5000 ohm*m, due to the orientations, there should be more effects of the hills which can be observed in figures 6.19 and 6.20.

When the ground is set at 10000 ohm*m, compared to the results of 5000 ohm*m, the same patterns are shown. The inphase and quad simulation results are in the same range. The inphase at 24.8 kHz of 5000 ohm*m is ranging from 3.29% to -3.97%, and the inphase at 24.8 kHz of 10000 ohm*m is ranging from 3.84% to -3.52%. In this case, the ground is already resistive, a different value or higher resistivity for the ground would not affect the VLF inphase and quad simulation results.

The conductive contrast between the ground and the lake water is huge. This causes the lake effect to dominate the VLF responses in the region. This conclusion is verified with the measurement data (2006 & 2012) and simulation results. However, due to overestimating the size of lake #2 in the region, when modeling, the VLF response of this lake could be overestimated, simultaneously making the VLF effect of hill #1 and #2 less visible.

The simulation results agree with the measurement data. In both the measurement data (2006 & 2012) and simulation results, at 24 kHz (NAA), there is not much evidence to indicate hill effects in the inphase plots while a small response of hill #2 in the Quad plots can be seen. At 24.8 kHz (NLK), a bigger response can be observed compared to the readings of 24 kHz in all data and simulation results, and hill #2 can be clearly observed.

The max inphase / max slope and max Quad / max slope versus skin depth / hill width ratios are also evaluated. When the ground resistivity is 5000 ohm*m, the skin depths can be calculated from equation 2.34 to be 251.65m. From the survey data, the widths of hill #1 and hill #2 are approximate 70m and 110m. Therefore, the skin depth / hill width ratios for hill #1 and hill #2 are 3.595 and 2.288. Referring to the trend functions in the figures 4.4 and 4.5, the max inphase / max slope and max Quad / max slope can be evaluated at 0.1 & 0.0695 for hill #1 and 0.15 & 0.099 for hill #2. The max slopes are approximate 0.17 for hill #1 and 0.2 for hill #2 based on the survey data. The max inphase and max Quad readings from calculations are 1.7% & 1.1% for hill #1 and 3% &

1.98% for hill #2. The same calculations are used at the case when the ground resistivity is 10000 ohm*m. The max inphase and max Quad readings are 1.25% & 0.9% for hill #1 and 2.2% & 1.5% for hill #2. The calculation results agree with both the measurement data and simulation results as they are all small scale numbers. The reason could be the terrain is so resistive that the skin depth is greater than the hill width. From the calculation results, it is clearly that hill #2 has more responses than hill #1. The inphase and Quad readings of hill #1 are small and could be approaching the noise level. This also explains why it is hard to observe topographic signal of hill #1 in the region.

The model is limited in many ways. Firstly, in the model, the lake is set as a regular shape. This could cause some model errors. Secondly, the depths of the lakes are greater than the actual values, and the conductivity of lake water is an approximate average value. These could cause the lake effects calculated from our model to be in error. Thirdly, the ground is set as a homogenous layer which is clearly an approximation.

Overall, the purpose of modeling the lakes and the hills is to determine if we could remove their effects from the data in order to help to detect deeper structures. Comparing the measurement data and simulation results, we can observe the effect of hill #2 with similar value ranges in inphase and Quad. Therefore, not much underground structure underneath hill #2 could be predicted. For the wave of frequency 24.8 kHz, we observe bigger VLF responses of hill #3 compared to hill #2 in the simulation results; however, contradictory results are shown in the measurement data. This indicates that there could be some underground structures underneath hill #3. The inphase and Quad due to the

structures are possibly combined with the effects due to hill #3 and causing a total reduction in near surface reading. And again, due to the huge conductivity contrast between the ground and the lake water, near lakes, it is difficult to determine whether the VLF effects are caused by the lakes or other ground structures.

CHAPTER 7
CONCLUSIONS

I have created a model of the Very Low Frequency Electromagnetic (VLF-EM) method using Comsol Multiphysics that is capable of simulating the effects of topography and lakes.

In VLF-EM prospecting, uneven terrain and lakes/streams contribute significant anomalies which cause the observed VLF data to depart from the pattern which would be expected on flat ground. In this report, a new 3D model of VLF using finite element simulations as implemented in Comsol is presented. Topographic and lake effects on VLF data are fully considered and are used to distinguish between such responses and those due to actual subsurface structures.

In this report, several basic models are established using finite-element modeling software, Comsol. These models include a homogeneous half-space case, layered ground and vertical contacts. In each model, the effects of different variable quantities (such as ground resistivity and thickness of layers) to observed data are studied and results are compared with theories. More complex models of hills and lakes are established and the effects of different geometry parameters are analyzed. When modeling topographic effects, two relationships between max inphase / max slope and max Quad / max slope versus skin depth / hill width are found, and can be used to predict topographic effects when the slope of a hill and resistivity of the ground are known.

The model is tested with survey data from Diefenbaker Hill Saskatoon, and applied to the Slush Lake region of Cameco Corporation Company. For Diefenbaker Hill, the

simulation results match the survey data and this indicates the practicability of the model. For the Slush Lake region, the VLF survey data is dominated by the large conductivity contrast between lake water and ground material, and the results are tested with simulations. Hill#2 VLF topographic effect from survey data matches the simulation results, which may indicate that there are less geological structures underneath. However, due to the lack of a full detailed survey and restrictions of the model, little evidence can be shown to indicate the underground structures.

For further analysis of the Slush Lake region to determine the underground structures, more survey data is required. A core sample with resistivity and thickness analysis of different underground layers are required. More detailed surveys of lake water conductivities, the depths of the lakes, and the geometries of the lakes are also required to improve the model. A detailed VLF survey over the region with higher resolution is highly recommended. With those data, better simulation results could be generated from the model and used to remove the topographic and lake effects in the VLF survey data.

REFERENCES

- Abdul-Malik, M. M., Myers, J. O., & McFarlane, J. (1985). Model studies of topographic noise in VAL-EM data: accounting for the direction of morphological strike relative to survey line and magnetic field directions. *Geoexploration*, 23, 217-225.
- Baker, H. A., & Myers, J. O. (1980). A topographic correction for VLF-EM profiles based on model studies. *Geoexploration*, 18, 135-144.
- Baranwal, V. C., Franke, A., Börner, R.-U., & Spitzer, K. (2011). Unstructured grid based 2-D inversion of VLF data for models including topography. *Journal of Applied Geophysics*, 75, 363-372.
- Beamish, D. (2000). Quantitative 2D VLF data interpretation. *Journal of Applied Geophysics*, 45, 33-47.
- d'Erceville, I., & Kunetz, G. (1962). The effect of a fault on the Earth's natural electromagnetic field. *Geophysics*, 651-665.
- Fraser, D. (1969). Contouring of VLF-EM data. *Geophysics*, 34, 958-967.
- Introduction to Comsol Multiphysics. (2014). from Comsol
<http://www.comsol.com/shared/downloads/IntroductionToCOMSOLMultiphysics.pdf>
- Kaikkonen, P. (1979). Numerical VLF modeling. *Geophysical Prospecting*, 27, 815-834.
- Karous, M., & Hjelt, S. E. (1977). Determination of apparent current density from VLF measurements. Finland: Department of Geophysics, University of Oulu
- Karous, M., & Hjelt, S. E. (1983). Linear filtering of VLF dip-angle measurements. *Geophysical Prospecting*, 31, 782-794.

- Karous, M. R. (1979). Effect of relief in EM methods with very distant source. *Geoexploration*, 17, 33-42.
- Mathieson, T. (July 2006). CREE EXTENSION VLF SURVEY logistics and analysis.
- McNeill, J. D., & Labson, V. F. (1991). Geological Mapping Using VLF Radio Fields *Electromagnetic Methods In Applied Geophysics* (pp. 521-587).
- Polarization of Plane Waves. Retrieved May 5, 2014, from <http://www.antenna-theory.com/basics/polarization.php>
- Reynolds, J. (1997). *An introduction to applied and environmental geophysics* (p. 693). John Wiley.
- Sinha, A. K. (1990a). Interpretation of Ground VLF-EM Data in Terms of Inclined Sheet-Like Conductor Models. *PAGEOPH*, 132.
- Sinha, A. K. (1990b). Interpretation of Ground VLF-EM Data in Terms of Vertical Conductor Models. *Geoexploration*, 26, 213-231.
- Skin Depth. Retrieved September 26, 2014, from <http://www.microwaves101.com/microwave-encyclopedia/708-skin-depth>
- Steane, R. A. (2009). Millennium Project Project Description: Cameco Corporation.
- Sundararajan, N., Babu, V. R., & Chaturvedi, A. K. (2011). Detection of basement fractures favourable to uranium mineralization from VLF-EM signals. *J. Geophys. Eng.*, 8, 330–340.
- Sundararajan, N., Babu, V. R., Prasad, N. S., & Srinivas, Y. (2006). VLFPROS—A Matlab code for processing of VLF-EM data. *Computers & Geosciences*, 32, 1806-1813.

Zhdanov, M. S., Varentsov, I. M., Weaver, J. T., Golubev, N. G., & Krylov, V. A. (1997).

Methods for modelling electromagnetic fields Results from COMMEMI - the international project on the comparison of modelling methods for electromagnetic induction. *Journal of Applied Geophysics*, 37, 133-271.